Tristan Seidlhofer, BSc

Material Model for Anisotropic Viscoelasticity at Finite Deformations Applied to Pulp Fibres

Master's Thesis
to achieve the university degree of
Master of Science
Master's degree programme: Mechanical Engineering
Computational Eng. & Mechatronics

submitted to

Graz University of Technology

Supervisor
Assoc.Prof. Dipl.-Ing. Dr.techn. Manfred Ulz

Institute of Strength of Materials
Head: Univ.-Prof. Dipl-Math.techn. Dr.-Ing. Thomas Hochrainer

Graz, November 2017

Affidavit

I declare that I have authored this thesis independently, that I have not used other than the declared sources/resources, and that I have explicitly indicated all material which has been quoted either literally or by content from the sources used. The text document uploaded to TUGRAZonline is identical to the present master's thesis.

Graz, _____ _____

Date Signature

Eidesstattliche Erklärung

Ich erkläre an Eides statt, dass ich die vorliegende Arbeit selbstständig verfasst, andere als die angegebenen Quellen/Hilfsmittel nicht benutzt, und die den benutzten Quellen wörtlich und inhaltlich entnommenen Stellen als solche kenntlich gemacht habe. Das in TUGRAZonline hochgeladene Textdokument ist mit der vorliegenden Masterarbeit identisch.

Graz, am _____ _____

Datum Unterschrift

Zusammenfassung

Das Ziel dieser Arbeit ist es ein Materialmodell zu finden, das die Eigenschaften einer Papierfaser abbilden kann. Die Arbeit unterteilt sich im Wesentlichen in zwei Teile. Im ersten Teil wird eine Einführung in die Finite Elemente Methode gegeben und die Materialgesetze abgeleitet. Im zweiten Teil wird auf die Kalibrierung der Materialparameter mit Nano-Indentierungsversuchen eingegangen.

Das Aufgabenpaket bestand darin ein anisotropes, viskoelastisches Materialmodell in einen bestehenden Finite-Elemente-Code in MATLAB und in einer User-Subroutine in ABAQUS zu implementieren. Mit dieser Implementierung wurden dann die Nano-Indentierungsversuche simuliert. Durch iteratives Anpassen der Materialparameter, mit entsprechenden Verfahren, wurden die Ergebnisse aus Simulation und Experiment angeglichen. Dieses Vorgehen führt zur Lösung der ursprünglichen Aufgabenstellung, die Materialparameter zu kalibrieren. Man spricht daher auch von der Lösung eines inversen Problems.

Abstract

The goal of this thesis is to find a material model that is capable of describing the behaviour of a pulp fibre. In the first major part of this thesis a general introduction to finite element analysis is given and the constitutive equations of the used material model are described. In the second major part the calibration of the material model parameters with nano indentation experiments is outlined.

An anisotropic viscoelastic material model for finite deformations is implemented into a finite element Matlab source code SOOFEA and in a user subroutine of ABAQUS. This implementation is then used to simulate nano indentations experiments. By iteratively adapting the material parameters the simulation results are fitted to the real experimental values. With that proceedure the material parameters can be calibrated.

Contents

List of Figures

List of Tables

1. Introduction

This thesis is a part of the research project that runs under the observation of the Christian Doppler (CD) laboratory in cooperation with the "Institute of Paper, Pulp- and Fibre Technology" and "Institute of Strength of Materials". The aim of this thesis is to find an appropriate material model to describe the behaviour of single pulp fibres and a calibration method of the model parameters with nano indentation experiments.

Paper has a wide range of application from printing to carton or even furniture. In practice, a well-established method to improve paper properties is to vary process parameters and benchmarking the paper quality by measuring for example the maximum tensile stresses or other significant material characteristics. On the other hand, paper needs to be printed in many applications. Therefore, printer companies are very interested to know how paper behaves in a printing process. Empirical optimisations is also performed but as a consequence the optimisation chain from manufacturer to printer is very long and the process time consuming. For that reason there is the wish to understand the internal mechanism of paper. Since paper consists of a fibre network as a first step the fibres have to be investigated.

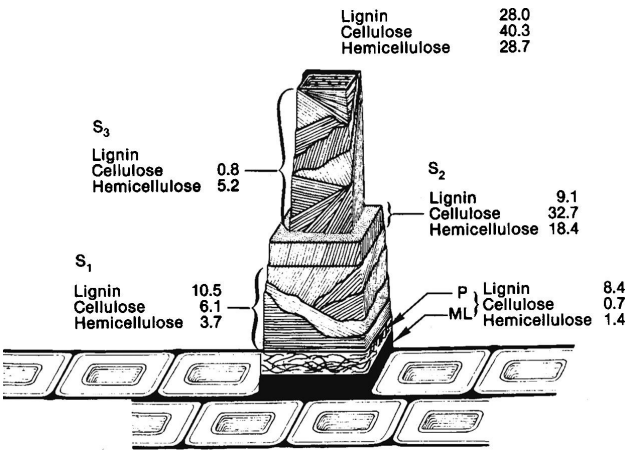

Figure 1.1.: Pulp fibre [27]

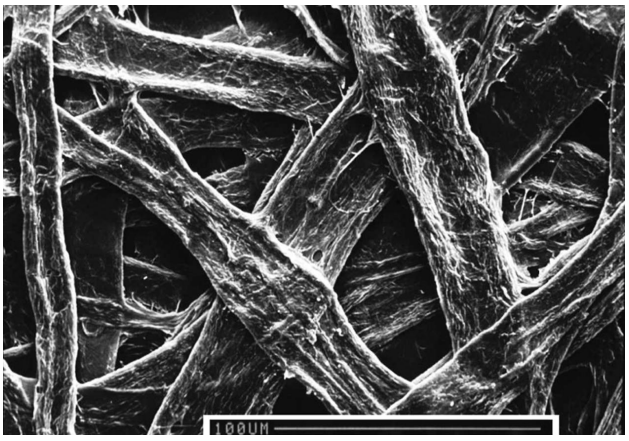

Figure 1.2.: Bonding of pulp fibres in a paper sheet [11]

Pulp fibres consist of various layers that are reinforced with fibrils (see figure 1.1). Thus, this material compound has in the direction of the fibre and perpendicular to the fibre different stiffness which has to be considered in the material model by implementing anisotropy. For finite deformation it is best to formulate the anisotropy in terms of structural tensors.

Furthermore, pulp fibres consist of cellulose, hemicellulose and lignin which have a similar chain structure as polymers. Because of the possible rearranging of these chains,

pulp fibres show a similar relaxation behaviour as polymers. Such behaviour is in a material model implemented in terms of viscoelasticity.

As a consequence, due to this complex material properties a single tensile test is not sufficient to estimate the material parameters. In the research project of the CD laboratory various experimental tests are performed and the missing piece to link all these measurements together is a suitable material model.

Regarding the material model itself, it is convenient to start with a well-established model that is used for polymers or rubber. In the works [9] and [21] in which an anisotropic viscoelastic model at finite deformations for rubber is discussed such a material model was found and used.

Well established methods are available for the estimation of the elastic parameters in fibre direction, however, this is not true for the transverse direction as a pulp fibre is as tiny as a human hair which makes a tensile test in transverse direction impossible. Therefore, nano indentation experiments are carried out on the outer surface of the pulp fibre. This test is also designed to enable extraction of viscoelastic parameters in addition to elastic properties.

This thesis is divided in two main parts. The first part starting with chapter 2 is dealing with the constitutive equations and the second starting with chapter 7 is dealing with the material parameter estimation.

Chapter 2 presents a brief introduction to finite deformation theory and in the following chapter 3 the implementation into a finite element framework is discussed. Chapter 4 outlines the derivation of the material model. The verification of the implementation is described in chapter 5. As it is necessary to have knowledge about how a specific material parameter is influencing the total response of the material for the calibration of the parameters chapter 6 explains the context.

Chapter 7 discusses a general solution method to solve the inverse problem that arises from the material parameter estimation. Chapter 8 gives a short introduction to atomic force microscopy. Chapter 9 presents an analytical approach to model the indentation experiments and a solution strategy. Chapter 10 outlines a testing procedure with a finite element Matlab source code SOOFEA for the constitutive equation. The simulation of the indentation experiments in ABAQUS is presented in 11 before chapter 12 summarises the findings.

2. Continuum Mechanics

In continuum mechanics, different approaches to describe deformation exist. Depending on the amount of local deformation, different theories are applied.

- Finite/large strain theory
- Infinitesimal/small strain theory
- Large displacement or large-rotation theory

In this paper, large rotations and strains have to be examined and therefore only the large strain theory is discussed.

2.1. Kinematics

In the modern continuum mechanics, the kinematics of material particles are described by a reference configuration $\mathfrak{B}_0$ also referred as material configuration and a current configuration known as spatial configuration. The relation between those two configurations is described by the nonlinear mapping equation 2.1. Furthermore, the deformation gradient is defined as in equation 2.2. The deformation gradient is a linear mapping in contrast to the point map $\varphi(\boldsymbol{X})$ and is a fundamental quantity in continuum mechanics.

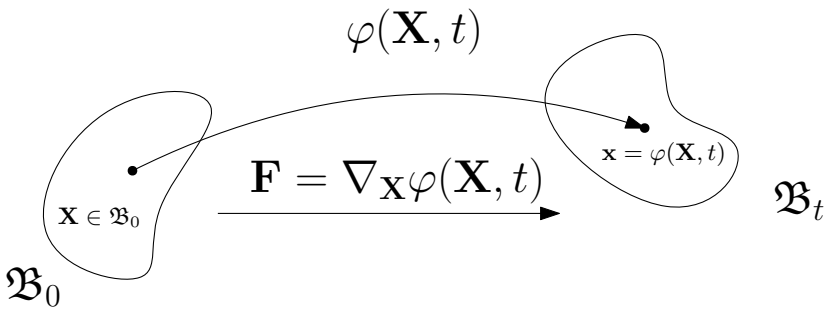

Figure 2.1.: Nonlinear point map and deformation gradient

$$x = \varphi(\boldsymbol{X}, t) \tag{2.1}$$

$$\boldsymbol{F} = \nabla_{\boldsymbol{X}}\varphi(\boldsymbol{X}, t) \tag{2.2}$$

The deformation gradient could, in a geometrical point of view, be considered as a map for tangents[1]. If $\boldsymbol{X} = \mathbf{P}(\xi)$ is a curve in the material configuration and $\boldsymbol{x} = \boldsymbol{p}(\xi)$ is a curve in the spatial configuration only dependent on the parameter $\xi \in \mathbb{R}$, then both are

[1]For a more detailed discussion on this topic, see [23].

related. Equation 2.1 illustrates this as $\boldsymbol{p}(\xi) = \varphi(\mathbf{P}(\xi), t)$. Using this expression on the tangents of the curves results in:

$$\underbrace{\frac{d\boldsymbol{p}(\xi)}{d\xi}}_{\boldsymbol{t}} = \nabla_{\boldsymbol{X}}\varphi(\boldsymbol{X}, t)\underbrace{\frac{d\boldsymbol{P}(\xi)}{d\xi}}_{\boldsymbol{T}} \tag{2.3}$$

$$\boldsymbol{t} = \boldsymbol{F}\boldsymbol{T} \tag{2.4}$$

From equation 2.4 follows that $\boldsymbol{F}$ could be considered as a mapping of tangents $\boldsymbol{T}$ in the material configuration to tangents $\boldsymbol{t}$ in the spatial configuration. Since in continuum mechanics the deformation gradient is more relevant than the mapping $\varphi(\boldsymbol{X}, t)$, it is also obvious to consider the tangent space $T_{\boldsymbol{X}}\mathfrak{B}_0$ in contrast to the particle configuration $\mathfrak{B}_0$

2.2. Strain

In finite strain theory the strains are based on the change of scalar product of two element vectors.

$$\frac{1}{2}(d\boldsymbol{x}_1 \cdot d\boldsymbol{x}_2 - d\boldsymbol{X}_1 \cdot d\boldsymbol{X}_2) = d\boldsymbol{X}_1 \cdot \boldsymbol{E}\, d\boldsymbol{X}_2 \tag{2.5}$$

Where $\boldsymbol{E}$ is the Green Lagrange strain tensor which operates on the material configuration. The Green Lagrange strain tensor itself is derived from the right Cauchy tensor which is on the other hand derived from the deformation gradient.

$$d\boldsymbol{x} = \boldsymbol{F}d\boldsymbol{X} \tag{2.6}$$

$$d\boldsymbol{x}_1 \cdot d\boldsymbol{x}_2 = d\boldsymbol{X}_1 \cdot \boldsymbol{C}d\boldsymbol{X}_2 \tag{2.7}$$

$$\boldsymbol{C} = \boldsymbol{F}^T\boldsymbol{F} \tag{2.8}$$

$$\boldsymbol{E} = \frac{1}{2}(\boldsymbol{C} - \boldsymbol{I}) \tag{2.9}$$

2.3. Stress

The basic concept is to find a relation between the Cartesian components σ_{ji} that are defined in the Cartesian coordinate planes da_i. With this σ_{ji} components the traction vectors in the respective coordinate planes can be described.

$$\mathbf{t}_i = \sigma_{1i}\mathbf{e}_1 + \sigma_{2i}\mathbf{e}_2 + \sigma_{3i}\mathbf{e}_3 \tag{2.10}$$

Evaluating now the equilibrium on a tetrahedron in figure 2.2 with the traction vector $\boldsymbol{t}_n$ corresponding to the surface with the normal vector $\boldsymbol{n}$ and the traction vectors of the coordinate planes as well as the body force $\boldsymbol{f}$ gives:

$$\mathbf{t}_n\, da = \sum_{j=1}^{3} \mathbf{t}_i\, da_i - \mathbf{f}\, dv \tag{2.11}$$

Note that the plane areas $da_i = \boldsymbol{n} \cdot \boldsymbol{e}_i\, da$ can be expressed by the projection of da. This equation can be simplified by dividing the equation with the area da and considering

$dv \to 0, da \to 0$.

$$\mathbf{t}_n = \sum_{i=1}^{3} \mathbf{t}_i \left(\boldsymbol{n} \cdot \boldsymbol{e}_i\right) \tag{2.12}$$

$$\mathbf{t}_n = \sum_{i,j=1}^{3} \sigma_{ji} \boldsymbol{e}_j \left(\boldsymbol{n} \cdot \boldsymbol{e}_i\right) \tag{2.13}$$

$$\mathbf{t}_n = \sum_{i,j=1}^{3} \underbrace{\sigma_{ji} \boldsymbol{e}_j \otimes \boldsymbol{e}_i}_{\boldsymbol{\sigma}} \boldsymbol{n} \tag{2.14}$$

$$\mathbf{t}_n = \boldsymbol{\sigma}\, \boldsymbol{n}. \tag{2.15}$$

With equation 2.15 the Cauchy stress tensor $\boldsymbol{\sigma}$ is found. This tensor relates the traction $\mathbf{t}_n$ with the normal vector $\mathbf{n}$. Since the normal vector and the traction vector do change evenly at a rigid body motion $\tilde{\mathbf{t}}_n = \mathbf{Q}\mathbf{t}_n, \tilde{\mathbf{n}} = \mathbf{Q}\mathbf{n}$, the Cauchy tensor is as a consequence objective. However, this property is lost at derivative respect to time. Furthermore, the Cauchy stresses tensor is defined in the spatial configuration and is because of the duality of shear stresses a symmetric tensor.
In modern formulation of continuum mechanics, the mapping between normal vector

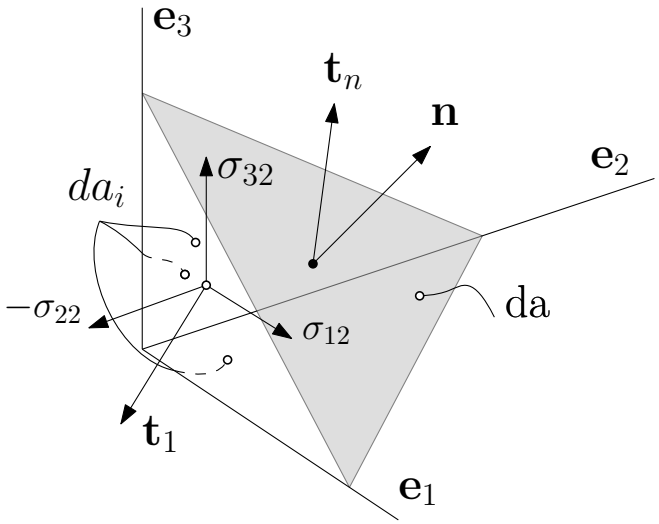

Figure 2.2.: Element tetrahedron

and tangent vector is described in terms of tangent spaces $T_X\mathcal{B}_0$ and co-tangent spaces $T_X^*\mathcal{B}_0$. This applies respectively for the spatial configuration $T_x\mathcal{B}_t$, $T_x^*\mathcal{B}_t$. Considering the Cauchy formula a mapping from co-tangent to tangent space is already found.

$$\boldsymbol{\sigma} = \begin{cases} T_x^*\mathcal{B}_t \to T_x\mathcal{B}_t \\ \boldsymbol{n} \mapsto \boldsymbol{t} = \boldsymbol{\sigma}\boldsymbol{n} \end{cases} \tag{2.16}$$

As a consequence $\boldsymbol{t}$ and $\boldsymbol{n}$ are in each space geometrically different but resemble in the same vector which has only different measures in the spaces.

2.4. Equilibrium and Virtual Work

The equilibrium equations can be formulated in the spatial or in the material configuration. With the push forward or pull back operations, both equilibrium formulations can be transformed into one another and are therefore equal. Nevertheless, depending on the used constitutive relations it is advantageous to use one formulation rather than the other. Even so that afterwards the equilibrium will be formulated in the material configuration the derivation of the equilibrium itself will be done in the spatial configuration and then pulled back to the material configuration.
The equilibrium of a volume v with the body force per volume $\boldsymbol{f}$ and the traction force $\boldsymbol{t}$ per area (see figure 2.3) is given by equation 2.17. With the Cauchy formula 2.15 and the Gauss theorem the equilibrium equation can be reformulated in a more suitable form 2.19.

$$\int_{\partial v} \boldsymbol{t}\, da + \int_v \boldsymbol{f} dv = \int_v \rho \ddot{\boldsymbol{u}}\, dv \tag{2.17}$$

$$\int_{\partial v} \boldsymbol{\sigma}\, \boldsymbol{n} da + \int_v \boldsymbol{f}\, dv + = \int_v \rho \ddot{\boldsymbol{u}}\, dv \tag{2.18}$$

$$\int_v (div \boldsymbol{\sigma} + \mathbf{f})\, dv = \int_v \rho \ddot{\boldsymbol{u}}\, dv \tag{2.19}$$

The virtual work is derived by multiplying the equilibrium equation 2.17 with a virtual displacement $\delta \boldsymbol{u}$. This is also known as the weak form.

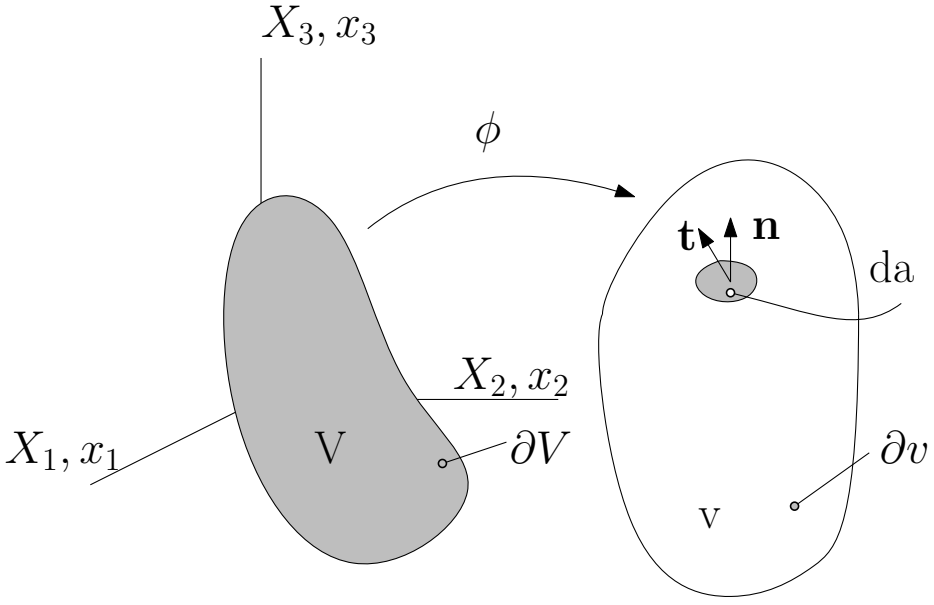

Figure 2.3.: Virtual work

$$\int_v (div \boldsymbol{\sigma} + \boldsymbol{f}) \cdot \delta \boldsymbol{u} dv = \int_v \rho \ddot{\boldsymbol{u}} \cdot \delta \boldsymbol{u} dv \tag{2.20}$$

With the divergence theorem $div(\boldsymbol{\sigma} \cdot \delta\boldsymbol{u}) = (div\boldsymbol{\sigma}) \cdot \delta\boldsymbol{u} + \boldsymbol{\sigma} : grad\,\delta\boldsymbol{u}$ equation 2.20 and the Gauss theorem $\int_v div\,\boldsymbol{\sigma} \cdot \delta\boldsymbol{u}\,dv = \int_{\partial v} \boldsymbol{\sigma}\boldsymbol{n} \cdot \delta\boldsymbol{u} = \int_{\partial v} \boldsymbol{t} \cdot \delta\boldsymbol{u}\,da$ can be rewritten as.

$$-\underbrace{\int_v \boldsymbol{\sigma} : grad\,\delta\boldsymbol{u}\,dv}_{W_{int}} + \underbrace{\int_v \boldsymbol{f} \cdot \delta\boldsymbol{u} dv + \int_{\partial v} \mathbf{t} \cdot \delta\boldsymbol{u}\,da}_{W_{ext}} = \underbrace{\int_v \rho\ddot{\mathbf{u}} \cdot \delta\boldsymbol{u}\,dv}_{W_{inertia}} \tag{2.21}$$

$$-W_{int} + W_{ext} = W_{inertia} \tag{2.22}$$

Depending on the configuration, other stress definitions than the Cauchy stresses $\boldsymbol{\sigma}$ are convenient to use. In this thesis, the focus lies on the Lagrangian configuration and therefore the second Piola Kirchoff stress tensor and the Green Lagrangian strain tensor $\boldsymbol{E}$ or right Cauchy tensor $\boldsymbol{C}$ is of importance. The derivation of the second Piola Kirchoff $\boldsymbol{S}$ is for the sake of completeness done below.
Keeping in mind that the gradient of the virtual displacement $\nabla\delta\boldsymbol{u}$ can be expressed by the Euler Almansi strain by equation 2.26. This relation is derived starting from equation 2.9. A more detailed explanation is discussed in [15].

$$\delta\boldsymbol{E} = \frac{1}{2}(\delta\boldsymbol{F}^T\boldsymbol{F} + \boldsymbol{F}^T\delta\boldsymbol{F}) \tag{2.23}$$

$$\delta\boldsymbol{F} = \delta(Grad\,\boldsymbol{u} + \boldsymbol{I}) = Grad\,\delta\boldsymbol{u} \tag{2.24}$$

$$\delta\boldsymbol{E} = \frac{1}{2}((Grad\delta\boldsymbol{u})^T\boldsymbol{F} + \boldsymbol{F}^T Grad\delta\boldsymbol{u}) \tag{2.25}$$

$$\delta\boldsymbol{e} = \boldsymbol{F}^{-T}\delta\boldsymbol{E}\boldsymbol{F}^{-1} = \frac{1}{2}((grad\delta\boldsymbol{u})^T + grad\delta\boldsymbol{u}) = sym(grad\delta\boldsymbol{u}) \tag{2.26}$$

Considering the symmetry of the Cauchy stress tensor, the internal work W_{int} in equation 2.21 can finally be expressed with equation 2.27. With the help of the pull back operation and the properties of the tensor dot product, the definition of the second Piola Kirchhoff follows as in equation 2.31.

$$\delta W_{int} = \int_v \boldsymbol{\sigma} : \delta\boldsymbol{e}\,dv \tag{2.27}$$

$$\delta W_{int} = \int_V J\boldsymbol{\sigma} : \boldsymbol{F}^{-T}\delta\boldsymbol{E}\boldsymbol{F}^{-1}dV \tag{2.28}$$

$$\delta W_{int} = \int_V \underbrace{J\boldsymbol{F}^{-1}\boldsymbol{\sigma}\boldsymbol{F}^{-T}}_{\boldsymbol{S}} : \delta\boldsymbol{E}dV \tag{2.29}$$

$$\delta W_{int} = \int_V \boldsymbol{S} : \delta\boldsymbol{E}dV \tag{2.30}$$

$$\boldsymbol{S} = J\boldsymbol{F}^{-1}\boldsymbol{\sigma}\boldsymbol{F}^{-T} \tag{2.31}$$

Remark 1. At this point, it should also be mentioned that from the variation of equation 2.9 follows:

$$\delta\boldsymbol{E} = \frac{1}{2}\delta\boldsymbol{C} \tag{2.32}$$

The relation between the stresses in the different tangent spaces are visualised in figure 2.4. The second Piola Kirchhoff tensor can be interpreted as a material force (push back of a spatial element force) per unit of undeformed area. In contrast, the first Piola

Kirchhoff tensor can be interpreted as the current force per unit of undeformed area which means that they are the analogy to the engineering stresses. The Cauchy stresses are also referred to as true stresses since they can be interpreted as the current force per unit of deformed area.

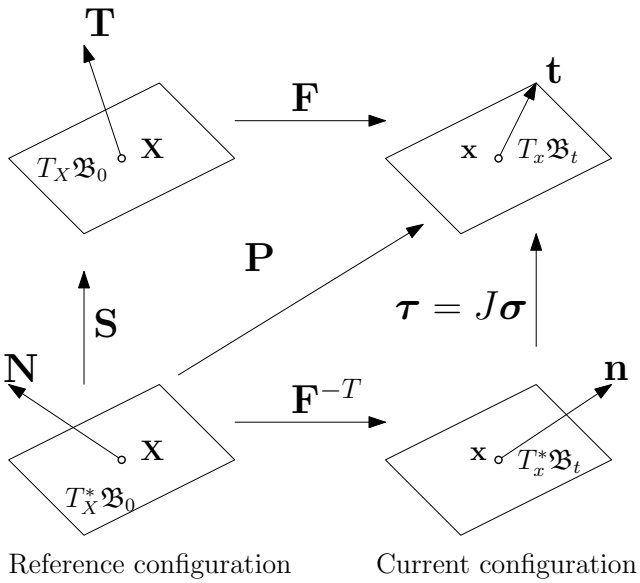

Figure 2.4.: Stress relations

Remark 2. To establish a commutative mapping between reference and current configuration the push/pull operations have to be considered. If in the reference configuration the second Piola Kirchhoff tensor $\boldsymbol{S}$ is used the respective mapping in the current configuration would be $\boldsymbol{FSF}^T = \boldsymbol{\tau}$ which is the Kirchhoff stress tensor.

2.5. Solution of Equilibrium Equation

Equation 2.30 is generally a non-linear equation system which is mainly solved with Newton's method. In practice a variety of Newton implementations exist. However, in this work only the well-established Newton algorithm (Newton-Raphson algorithm) with algorithmic consistent tangent will be outlined.

2.6. Newton Algorithm

To show the principle of the Newton algorithm it is exemplary applied on a one vector function $f(\boldsymbol{x})$. At first, the function $f(\boldsymbol{x})$ is linearised at a starting vector $\boldsymbol{x}_k$ with a Taylor's series which results in equation 2.33. Here, the ∇ operator is a column vector so that the product $\nabla \boldsymbol{x}^T$ gives the Jacobian matrix $\boldsymbol{J}$. The iteration rule follows by finding the

zero points $\boldsymbol{x}_{k+1}$ of equation 2.33.

$$f(\boldsymbol{x}) = f(\boldsymbol{x}_k) + \underbrace{\overbrace{\nabla \boldsymbol{x}_k^T}^{\boldsymbol{J}}(\boldsymbol{x} - \boldsymbol{x}_k)}_{Df(\boldsymbol{x}_k)[\boldsymbol{u}]} \tag{2.33}$$

$$\boldsymbol{x}_{k+1} = \boldsymbol{x}_k - \boldsymbol{J}^{-1} f(\boldsymbol{x}_k) \tag{2.34}$$

For a more general notation the linearisation is noted with the symbol $Df(\boldsymbol{x}_0)[\boldsymbol{u}]$. Where $\boldsymbol{u}$ indicates the step or increment which is in the upper case $(\boldsymbol{x} - \boldsymbol{x}_0)$. The general iteration rule for a complex function $\mathcal{F}(\boldsymbol{x})$ with the Newton's method is then given by equation 2.36 with the assumption that the equation system could be solved respectively to $\boldsymbol{u}$.

$$D\mathcal{F}(\boldsymbol{x}_k)[\boldsymbol{u}] = -\mathcal{F}(\boldsymbol{x}_k) \tag{2.35}$$

$$\boldsymbol{x}_{k+1} = \boldsymbol{x}_k + \boldsymbol{u} \tag{2.36}$$

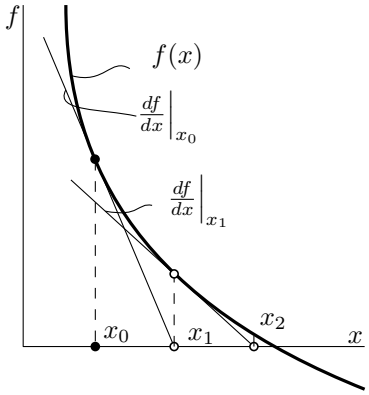

Figure 2.5.: One dimensional Newton's method

2.7. Linearisation of the Constitutive Equations

At first, the equilibrium equation is discretised 2.21 and then linearised. Where $(\dots)^{n+1}$ stands for the current unknown state and $(\dots)^n$ for the known previous step. Since the external work W_{ext}^{n+1} is known no linearisation has to be performed.

$$\delta W_{int}^{n+1} + \delta W_{inertia}^{n+1} = \delta W_{ext}^{n+1} \tag{2.37}$$

$$D\delta W_{int}^{n}[\boldsymbol{u}] + D\delta W_{inertia}^{n}[\boldsymbol{u}] = \delta W_{ext}^{n+1} - \delta W_{int}^{n} - \delta W_{inertia}^{n} \tag{2.38}$$

In this work quasi static problems are solved so that the inertia part could be neglected.

$$D\delta W_{int}^{n}[\boldsymbol{u}] = \delta W_{ext}^{n+1} - \delta W_{int}^{n} \tag{2.39}$$

As seen in section 2.6 and equation 2.39, the Newton method requires a linearisation of the function. It is further necessary to linearise the internal work equation 2.30. In the following the equations are written in index notation.

$$D\delta W_{int}[\boldsymbol{u}] = \int_V \{DS_{ij}[\boldsymbol{u}]\delta E_{ij} + S_{ij} D\delta E_{ij}[\boldsymbol{u}]\}\, dV \tag{2.40}$$

Remark 3. From equation 2.9 the variation $\delta[\dots]$ and linearisation $D\dots[\boldsymbol{u}]$ of the Green Lagrange strain tensor follows. The mathematical operation of both are similar.

$$\delta E_{ij} = \frac{1}{2}\delta C_{ij} = \frac{1}{2}\left\{\delta F_{mi}F_{mj} + F_{ni}\delta F_{nj}\right\} \tag{2.41}$$

$$DE_{kl}[\boldsymbol{u}] = \frac{1}{2}\left\{DF_{rk}[\boldsymbol{u}]F_{rl} + F_{sk}DF_{sl}[\boldsymbol{u}]\right\} \tag{2.42}$$

For the linearised internal work 2.40, the linearisation of the varied Green Lagrange strain tensor $\delta\boldsymbol{E}$ and the second Piola Kirchhoff tensor is necessary.

$$D\delta E_{ij}[\boldsymbol{u}] = \frac{1}{2}\left\{D\delta F_{mi}[\boldsymbol{u}]F_{mj} + \delta F_{mi}DF_{mj}[\boldsymbol{u}] + DF_{ni}[\boldsymbol{u}]\delta F_{nj} + F_{ni}D\delta F_{nj}[\boldsymbol{u}]\right\} \tag{2.43}$$

$$\tag{2.44}$$

The linearisation of the virtual quantities $\delta(\dots)$ are zero since per definition they remain constant in an incremental step $\boldsymbol{u}$. This is in detail discussed in remark 5.

$$D\delta E_{ij}[\boldsymbol{u}] = \frac{1}{2}\left\{\delta F_{mi}DF_{mj}[\boldsymbol{u}] + DF_{li}[\boldsymbol{u}]\delta F_{lj}\right\} \tag{2.45}$$

$$\tag{2.46}$$

Remark 4. Due to the fact that the second Piola Kirchhoff tensor can be expressed as a function of the Green Lagrange strain tensor, the linearisation of the second Piola Kirchhoff tensor can be represented by equation 2.47 by applying the chain rule. The derivation of the second Piola Kirchhoff respective the Green Lagrange strain tensor is also known as the material/Lagrangian tangent moduli or Lagrangian elasticity tensor $\mathbb{C}$. A more detailed explanation is given in chapter 4.

$$DS_{ij}[\boldsymbol{u}] = \frac{\partial S_{ij}}{\partial E_{kl}}DE_{kl}[\boldsymbol{u}] = \mathbb{C}_{ijkl}DE_{kl}[\boldsymbol{u}] \tag{2.47}$$

Remark 5. The virtual work is at an increment defined by a trial solution position given by the mapping ϕ_k and the virtual displacement $\delta\boldsymbol{u}$ as $\delta W(\phi_k, \delta\boldsymbol{u})$. For the solution with Newton's method it is necessary that in an increment $\boldsymbol{u}$ the virtual work δW change is solely caused due to $\boldsymbol{u}$ itself by $\phi_k + \boldsymbol{u}$. As the virtual displacement is an independent variable, the virtual displacement $\delta\boldsymbol{u}$ has to be constant in an increment. This is visualised in figure 2.6.

The term $\delta\boldsymbol{F} = \frac{\partial\delta\boldsymbol{u}}{\partial\boldsymbol{X}} = \boldsymbol{\nabla}_0\delta\boldsymbol{u}$ is representing in this context the virtual displacement. The linearisation of this term in the increment $\boldsymbol{u}$ is in many cases zero. This depends on the form of the nabla operator $\boldsymbol{\nabla}_0$ (coordinate system) and on the element type in a finite element context (see equation 3.9). In this thesis only Cartesian coordinates and brick elements are used so that these linearised terms are equal to zero.

$$D\delta W_{int}[\boldsymbol{u}] = \int_V \mathbb{C}_{ijkl}DE_{kl}[\boldsymbol{u}]\delta E_{ij}\,dV + \int_V S_{ij}D\delta E_{ij}[\boldsymbol{u}]\,dV \tag{2.48}$$

Equating now the first integral of equation 2.48 with remark 4 and 3 gives:

$$\int_V \mathbb{C}_{ijkl}\frac{1}{2}\left\{DF_{rk}[\boldsymbol{u}]F_{rl} + F_{sk}DF_{sl}[\boldsymbol{u}]\right\}\frac{1}{2}\left\{\delta F_{mi}F_{mj} + F_{li}\delta F_{lj}\right\}\,dV \tag{2.49}$$

$$\int_V \mathbb{C}\frac{1}{4}\left\{DF_{rk}[\boldsymbol{u}]F_{rl}\delta F_{mi}F_{mj} + DF_{rk}[\boldsymbol{u}]F_{rl}F_{li}\delta F_{lj} + F_{sk}DF_{sl}[\boldsymbol{u}]\delta F_{mi}F_{mj} + F_{sk}DF_{sl}[\boldsymbol{u}]F_{li}\delta F_{kj}\right\} \tag{2.50}$$

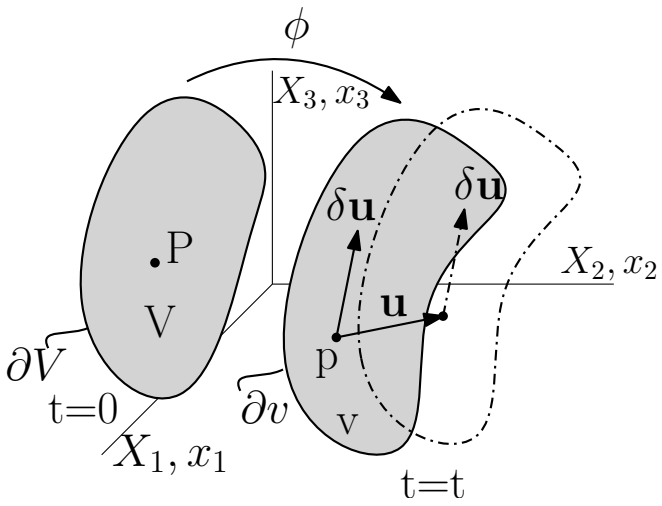

Figure 2.6.: Virtual displacement

By using the minor symmetry of the Lagrange moduli $\mathbb{C}_{ijkl} = \mathbb{C}_{jikl} = \mathbb{C}_{ijlk}$ equation 2.50 can be further simplified.

$$\int_V \mathbb{C}_{ijkl} DF_{rk}[\boldsymbol{u}] F_{rl} \delta F_{mi} F_{mj} \, dV \tag{2.51}$$

For the second integral of equation 2.48 follows:

$$\int_V S_{ij} D\delta E_{ij}[\boldsymbol{u}] \, dV \tag{2.52}$$

$$\int_V S_{ij} \frac{1}{2} \left\{ \delta F_{mi} DF_{mj}[\boldsymbol{u}] + DF_{li}[\boldsymbol{u}] \delta F_{lj} \right\} \, dV \tag{2.53}$$

Again the symmetry of the second Piola Kirchhoff tensor can be used.

$$\int_V S_{ij} \delta F_{mi} DF_{mj}[\boldsymbol{u}] \, dV \tag{2.54}$$

Inserting the found expressions for the linearised internal work into equation 2.39 gives:

$$\underbrace{\int_V \mathbb{C}_{ijkl} DF_{rk}[\boldsymbol{u}] F_{rl} \delta F_{mi} F_{mj} \, dV}_{\text{material tangent}} + \underbrace{\int_V S_{ij} \delta F_{mi} DF_{mj}[\boldsymbol{u}] \, dV}_{\text{geometrical tangent}} = \delta W_{ext}^{n+1} - \delta W_{int}^{n} \tag{2.55}$$

3. Finite Element Method

In general, the iteration rule for the Newton method is defined with equation 2.55. However, as can be seen the displacement $\boldsymbol{u}$ does not directly appear in the equation and therefore the equation system cannot be solved respective to $\boldsymbol{u}$. The finite element method can be used to provide solveable equations. In the finite element method, the displacement $\boldsymbol{u}$ and the coordinates $\boldsymbol{x}$ are defined by shape functions which are in general Lagrange polynomials. Due to the Gauss integration it is also best to transform the local coordinate system of the element X, Y, Z into an iso-parametric r, s, t one. For that reason the Jacobian $\boldsymbol{J}$ of the shape function occurs. This iso-parametric configuration is visualised in the figure 3.1. Here, n indicates the amount of points $n+1$.

$$h_{[i,j,k]}(r,s,t) = l_i^n(r) l_j^o(s) l_k^p(t) \tag{3.1}$$

$$l_i^n(x) = \prod_{\substack{k=0 \\ k \neq i}}^{n} \frac{x - x_k}{x_i - x_k} \tag{3.2}$$

$$x = \sum_{i=1}^{n} h_i(r,s,t)\hat{x}_i \qquad y = \sum_{i=1}^{n} h_i(r,s,t)\hat{y}_i \qquad z = \sum_{i=1}^{n} h_i(r,s,t)\hat{z}_i \tag{3.3}$$

$$u = \sum_{i=1}^{n} h_i(r,s,t)\hat{u}_i \qquad v = \sum_{i=1}^{n} h_i(r,s,t)\hat{v}_i \qquad w = \sum_{i=1}^{n} h_i(r,s,t)\hat{w}_i \tag{3.4}$$

$$\tag{3.5}$$

Remark 6. The displacements $\boldsymbol{u}$ can therefore be expressed by the discrete displacements $\hat{\boldsymbol{u}}$ by:

$$\boldsymbol{u} = \boldsymbol{H}(r,s,t)\hat{\boldsymbol{u}} \tag{3.6}$$

Where $\boldsymbol{H}$ is defined by the Lagrange polynomials at the respective node positions. Therefore, the shape of $\boldsymbol{H}$ depends also on the element type.

Remark 7. With the definition of the shape functions the deformation gradient is defined as:

$$\boldsymbol{F} = \frac{\partial(\boldsymbol{X} + \boldsymbol{u})}{\partial \boldsymbol{X}} = \boldsymbol{1} + \frac{\partial \boldsymbol{u}}{\partial \boldsymbol{X}} = \boldsymbol{1} + \frac{\partial \boldsymbol{r}}{\partial \boldsymbol{X}} \frac{\partial \boldsymbol{u}}{\partial \boldsymbol{r}} = \boldsymbol{1} + \underbrace{\boldsymbol{J}^{-1} \frac{\partial \boldsymbol{H}(r,s,t)}{\partial \boldsymbol{r}}}_{\boldsymbol{B}} \hat{\boldsymbol{u}} \tag{3.7}$$

$$\tag{3.8}$$

For the linearisation of the deformation gradient and the variation follows:

$$\delta \boldsymbol{F} = \boldsymbol{B} \delta \hat{\boldsymbol{u}} \quad \delta F_{ij} = B_{im} \delta \hat{u}_{mj} \tag{3.9}$$

$$D\boldsymbol{F}[\boldsymbol{u}] = \boldsymbol{B}\hat{\boldsymbol{u}} \quad DF_{ij}[\boldsymbol{u}] = B_{im}\hat{u}_{mj} \tag{3.10}$$

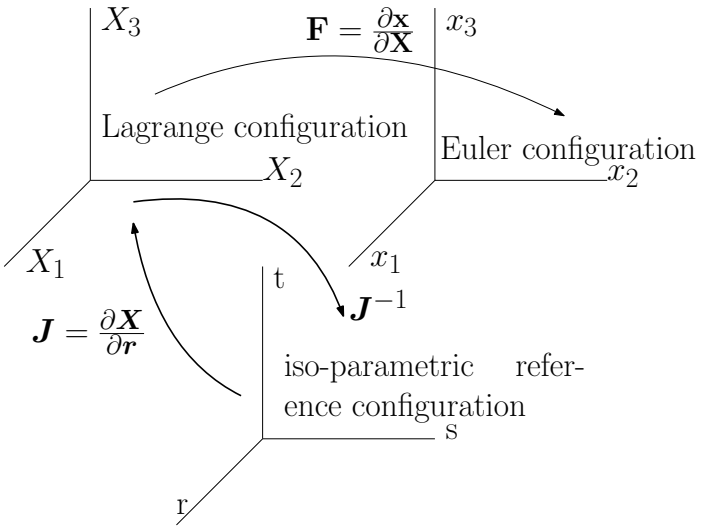

Figure 3.1.: Configurations

Principally, the integrals 2.55 are solved during the numerical integration by evaluating the integral expressions at every Gauss points of an element. As a consequence, the material routine is called at all Gauss point of the element. For the integration in the iso-parametric configuration over the volume also the boundaries have to be transformed.

$$dV = det(\boldsymbol{J}) d\bar{V} = R d\bar{V} \tag{3.11}$$

3.1. Assembling

Since the integration is performed on element level, the resulting element stiffness matrices have to be assembled to a global stiffness matrix by ordering these element stiffness matrices correctly.

3.2. Newton Algorithm

With the linearised internal work of section 2.7, the iteration rule 2.39 for the Newton algorithm can now be specified with the deformation gradient approximation of remark 7. The shape functions are defined in the iso-parametric configuration. Consequently, the volume boundary V of the integrals 2.54 and 2.51 must be transformed to the iso-parametric reference configuration with equation 3.11. The determinant R of the Jacobian is not to be confused with the determinant J of the deformation gradient.

$$\int_{\bar{V}} \delta\hat{u}_{li} B_{ml} S_{ij} B_{mn} \hat{u}_{nj} R \, d\bar{V} \tag{3.12}$$

Introducing the approximation into the integral 2.51 gives

$$\int_{\bar{V}} \delta\hat{u}_{ni} B_{mn} F_{mj} \mathbb{C}_{ijkl} F_{rl} B_{rq} \hat{u}_{qk} R \, d\bar{V}. \tag{3.13}$$

For the known part of the inner virtual energy δW_{int}^n follows.

$$\delta W_{int}^n = \int_{\bar{V}} S_{ij}\delta E_{ij} R\, d\bar{V} = \int_{\bar{V}} S_{ij}\frac{1}{2}(\delta F_{mi}F_{mj} + F_{ni}\delta F_{nj}) R\, d\bar{V} \tag{3.14}$$

$$= \int_{\bar{V}} \delta F_{mi} S_{ij} F_{mj} R\, d\bar{V} \tag{3.15}$$

$$= \int_{\bar{V}} \delta \hat{u}_{ui} B_{mu} F_{mj} S_{ij} R\, d\bar{V}. \tag{3.16}$$

Remark 8. Commonly, the displacements $\hat{\boldsymbol{u}}$ are arranged in a column vector. However, here the displacement is written in a matrix form $\hat{u}_{ij}$ to enable a clear index notation. In the other case, a Voigt representation of the other quantities would have been necessary[1].

Finally, putting the found expressions into equation 2.55.

$$D\delta W_{int}[\hat{\boldsymbol{u}}] = \delta W_{ext} - \delta W_{int} \tag{3.17}$$

$$\int_{\bar{V}} \delta \hat{u}_{ni} B_{mn} F_{mj} \mathbb{C}_{ijkl} F_{rl} B_{rq} \hat{u}_{qk} R\, d\bar{V} + \int_{\bar{V}} \delta \hat{u}_{li} B_{ml} S_{ij} B_{mn} \hat{u}_{nj} R\, d\bar{V} = \ldots$$
$$\ldots \delta \hat{u}_{mu} F_{um}^{ext} - \int_{\bar{V}} \delta \hat{u}_{ui} B_{mu} F_{mj} S_{ij} R\, d\bar{V} \tag{3.18}$$

$$\delta \hat{u}_{ni} \int_{\bar{V}} \left(B_{mn} F_{mj} \mathbb{C}_{ijkl} F_{rl} B_{rq} - B_{mn} S_{ik} B_{mq}\right) R\, d\bar{V}\, \hat{u}_{qk} = \ldots$$
$$\ldots \delta \hat{u}_{mu} F_{um}^{ext} - \delta \hat{u}_{ui} \int_{\bar{V}} B_{mu} F_{mj} S_{ij} R\, d\bar{V} \tag{3.19}$$

$$\delta \hat{\boldsymbol{u}} \underbrace{\int_{\bar{V}} (\boldsymbol{B}\boldsymbol{F}\mathbb{C}\boldsymbol{F}\boldsymbol{B} + \boldsymbol{B}\boldsymbol{S}\boldsymbol{B})\, det(\boldsymbol{J})\, d\bar{V}\, \hat{\boldsymbol{u}}}_{D\boldsymbol{F}_{int}[\hat{\boldsymbol{u}}]} = \delta \hat{\boldsymbol{u}} \boldsymbol{F}_{ext} - \delta \hat{\boldsymbol{u}} \underbrace{\int_{\bar{V}} \boldsymbol{B}\boldsymbol{F}\boldsymbol{S}\, det(\boldsymbol{J})\, d\bar{V}}_{\boldsymbol{F}_{int}} \tag{3.20}$$

$$D\boldsymbol{F}_{int}[\hat{\boldsymbol{u}}] = \boldsymbol{F}_{ext} - \boldsymbol{F}_{int} \tag{3.21}$$

To get the iteration rule of the Newton method equation, 3.21 has to be discretized. For that the notation of remark 9 is used. In a non-linear finite element analysis it is common to prescribe the load in increments to establish a better convergence. These increments are also known as pseudo time steps for static analysis. However, if the material follows a time or kinematic dependent behaviour for example viscoelasticity, plasticity or the material is subjected to a dynamic analysis then the load increment is also coupled to a time step. Here, n indicates the load increments and i the Newton steps.

Remark 9.

$$[\bullet]_n^i \tag{3.22}$$

n . . . n-th load prescription
i . . . i-th iteration of Newton algorithm

With the notation of remark 9 equation 3.21 can be rewritten in a discrete form.

$$D\boldsymbol{F}_{int}[\hat{\boldsymbol{u}}_{n+1}^{i+1}] = (\boldsymbol{F}_{ext})_{n+1} - (\boldsymbol{F}_{int})_{n+1}^{i} \tag{3.23}$$

Remark 10. As the increment in Newton's Method is equivalent to a (pseudo) time step, the linearisation is equivalent to a time derivation. This is also the reason why in literature often the displacement $\boldsymbol{u}$ is replaced by a velocity $\boldsymbol{v}$ to be consistent.

Considering the linearisation of the internal work of remark 4 this expression can also be interpreted as time derivatives.

$$\dot{\boldsymbol{S}} = \mathbb{C} : \dot{\boldsymbol{E}} \tag{3.24}$$

[1] See for example [3].

A push forward operation of this equation leads to the Truesdell rate of the Kirchhoff stresses $\boldsymbol{\tau}^{\circ}$. However, the Euler tangent $\boldsymbol{c}$ is defined for the Truesdell rate of the Cauchy stresses. Hence, the Euler tangent is a push forward of the Lagrange tangent $\mathbb{C}$ plus a division by J as stated in equation 3.27

$$\boldsymbol{\tau}^{\circ} = J\boldsymbol{c} : \boldsymbol{d} \tag{3.25}$$

$$\boldsymbol{\sigma}^{\circ} = \boldsymbol{c} : \boldsymbol{d} \tag{3.26}$$

$$\boldsymbol{c} = J^{-1}\phi_{*}[\mathbb{C}] \tag{3.27}$$

If an update Lagrangian formulation is used and the finite element framework expects a specific rate form, it has to be made sure that the right spacial tangent is evaluated. Regarding ABAQUS this is discussed in the appendix 3.

3.2.1. Residuum

So, as in figure 3.2 could be seen for every load increment $\boldsymbol{F}_{n+1}^{ext}$ starting from point n Newton's method is applied. The equilibrium or solution is found if the unbalanced forces or residuum $\boldsymbol{\psi}_{n+1}^{i+1}$ defined as in equation 3.28 is zero. However, since in a numerical solution zero will never be reached, an appropriate stopping criterion must be defined.

$$\boldsymbol{\psi}_{n+1}^{i+1} = (\boldsymbol{F}_{ext})_{n+1} - (\boldsymbol{F}_{int})_{n+1}^{i+1} \tag{3.28}$$

Remark 11. If the unbalance of the forces $\boldsymbol{F}_{ext}$ and $\boldsymbol{F}_{int}$ which is also known as residuum ψ_{n+1} is multiplied with the respective node displacements $\hat{\boldsymbol{u}}$ we get as a result the unbalanced energy.

$$(W_{unb})_{n+1}^{i+1} = \left(\hat{\boldsymbol{u}}_{n+1}^{i+1} - \hat{\boldsymbol{u}}_{n+1}^{i}\right) \cdot \boldsymbol{\psi}_{n+1}^{i+1} \tag{3.29}$$

$$(W_{unb})_{n+1}^{i+1} < tolerance \tag{3.30}$$

With the unbalanced energy an ideal stopping criterion 3.30 is found. The Newton algorithm with algorithmic consistent tangent has a quadratic convergence. Since here the virtual works were linearised also only the unbalanced energy has a quadratic convergence. The advantage is that if the calculation of the tangent is faulty then the quadratic convergence is instantaneously lost so that the correctness of the implementation could be investigated. New implementations are often firstly tested on simple structures to be able to perform plausibility checks.
For further information on this topic see [7].

3.3. Multi-field Variational Principle

For the usage of nearly incompressible materials, the pure variation of the displacement tends to locking phenomena and has a poor performance in a numerical sense. Therefore, for example the hydrostatic pressure or the volume ratio is treated as an extra independent variable. There are many approaches from two to three field variational principles. Here, only the three field variational Jacobian-pressure principle (Hu-Washizu variational principle) which is implemented in the Abaqus's mixed Hybrid elements is introduced.
The isochoric hyperelastic potential is extended by an additional term (with a Lagrange

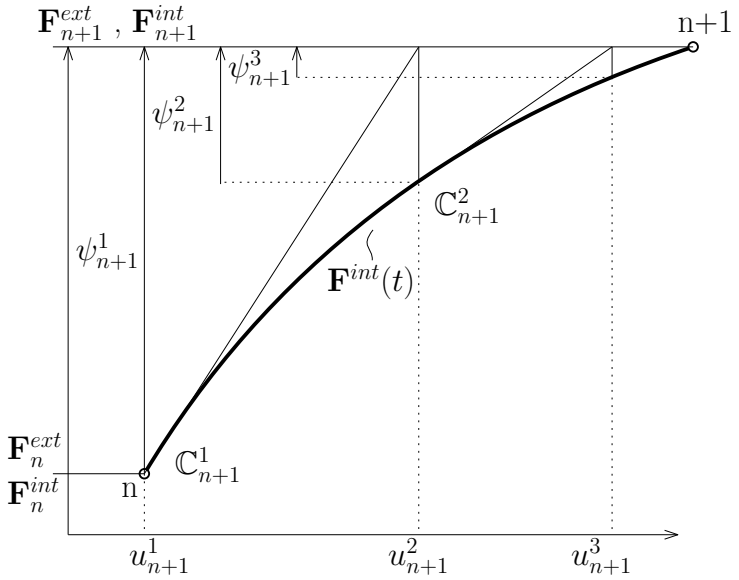

Figure 3.2.: Newton-Raphson algorithm

multiplier $\hat{p}$). So, in addition to the displacement field $\boldsymbol{u}$ the pressure field $\hat{p}$ and Jacobian $\hat{J}$ is varied.

$$W_{int} = \int_V \left[\psi_{iso}(\bar{I}_1(\boldsymbol{u}), \bar{I}_2(\boldsymbol{u})) + \psi_{vol}(\hat{J}) - \hat{p}(J(\boldsymbol{u}) - \hat{J})\right] dV \tag{3.31}$$

$$\tag{3.32}$$

For the variation of the virtual work follows:

$$\delta W_{int} = \int_V \left[2\frac{\partial \psi}{\partial \boldsymbol{C}} : \delta \boldsymbol{E} + (\frac{\partial \psi_{vol}}{\partial \hat{J}} + p)\delta\hat{J} - (J(\boldsymbol{u}) - \hat{J})\delta\hat{p}\right] dV \tag{3.33}$$

$$\psi = \psi_{vol} + \psi_{iso} \tag{3.34}$$

For a more detailed explanation, consult reference [1], [5] and [15].
In the appendix 2, it is briefly shown how this variational principle is implemented in the user subroutine of ABAQUS.

4. Material Model

The well documented work of Dirk Liefeith [9], [21], which is the basis for this chapter, should not go unmentioned at this point.

Before the constitutive equations are derived based on the works of [33], [29] and [30] a short introduction to the necessary theory is given. Especially the incompressibility, the formulation of hyperelasticity and anisotropy is outlined.

4.1. Pulp Fibres

To understand the selection of the material model, it is advisable to look at a pulp fibre from the mechanical point of view. A pulp fibre consists of various layers with different properties. In figure 4.1 it is illustrated how the S_2-layer of the fibre is made up. The S_2-layer is the main part of the fibre wall thickness and therefore only this layer is exemplary discussed.

This layer is reinforced with cellulose micro-fibrils that are in a helical form arranged. Those have a higher stiffness than the matrix material. When in wood, the fibres are hollow but due to the production of paper the fibres collapse so that they can be modelled as in figure 4.2. With that the top side and bottom side mirrored can be described with a material that possesses another stiffness in one direction. Such a material is referred as transverse isotropic which is indicating that the material differs in stiffness in two perpendicular directions. Such a simulation of a collapsed fibre is performed in section 5.1.4.

It is known that biological materials, polymers and rubber have Poisson's ratios close to 0.5 which justifies the usage of incompressible or nearly incompressible material laws. Hemicellulose, lignin, cellulose which the pulp fibre consists of have a similar internal structure as polymers. Polymers show due to its molecule chain structure a relaxation behaviour which can also be observed on pulp fibres. Such a relaxation is modelled in terms of viscoelasticity. Viscoelasticity is in literature mainly applied on incompressible materials.
Considering these relations, it is assuring to implement an anisotropic, viscoelastic and incompressible material model.

4.2. Incompressibility

The volume preserving constraint of incompressible materials has as side effect that little changes in volume can lead to an extremely high hydrostatic pressure p (see also remark 12). Such high stress would lead to a bad conditioned stiffness matrix and a bad convergence. To circumvent this problem the incompressibility constraint is only partly fulfilled and a deviation is penalised.

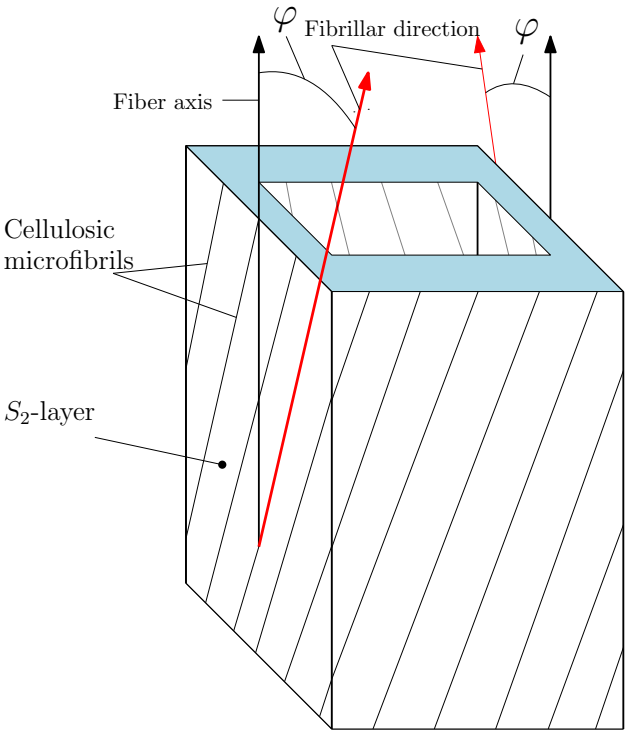

Figure 4.1.: Pulp fibre

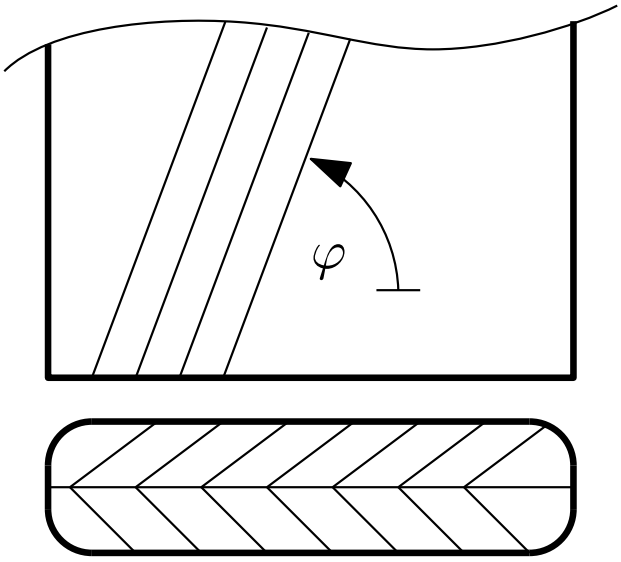

Figure 4.2.: Collapsed pulp fibre

Remark 12. The total stresses $\boldsymbol{\sigma}$ can be decomposed into the hydrostatic pressure p which changes the volume and a deviatoric part $\boldsymbol{\sigma}_{dev}$ that leads to a volume preserving distortion.

$$p = \frac{1}{3} tr(\boldsymbol{\sigma}) \tag{4.1}$$

$$\boldsymbol{\sigma} = \boldsymbol{\sigma}_{dev} + p\boldsymbol{I} \tag{4.2}$$

To establish this in a finite deformation analysis the constitutive laws are split into a volumetric and an isotropic part. Where the volumetric part is purely designated as penalty function. For further information see [5].

$$\boldsymbol{F} = \boldsymbol{F}^{iso}\boldsymbol{F}^{vol} \tag{4.3}$$

$$J = det\,[\boldsymbol{F}] \tag{4.4}$$

$$\boldsymbol{F}^{vol} = J^{\frac{1}{3}}\mathbf{1} \tag{4.5}$$

$$\boldsymbol{F}^{iso} = J^{-\frac{1}{3}}\boldsymbol{F} \tag{4.6}$$

The volumetric deformation gradient is a spherical tensor and includes the total volume change. In the following, the volume preserving isochoric quantities are marked with a bar $\boldsymbol{F}^{iso} = \bar{\boldsymbol{F}}$.

4.3. Hyperelasticity

Elastic constitutive equations are only dependent on the current state. If the work done by the stresses is path independent, which means the work in a time interval can be

expressed by the initial and final configuration, the work can be expressed with a scalar elastic potential function $\psi(\boldsymbol{F}(\boldsymbol{X}), \boldsymbol{X})$. Such a behaviour is termed hyperelastic.
The strain energy function must remain invariant due to a rigid body rotation. As we know, the deformation gradient can be split in a stretch $\boldsymbol{U}$ and a rotation $\boldsymbol{R}$ by $\boldsymbol{F} = \boldsymbol{RU}$ but we also know that $\boldsymbol{C} = \boldsymbol{U}^2$. This implies that it is best to represent the strain energy function in terms of the right Cauchy tensor $\boldsymbol{C}$. Keeping in mind that the strain energy function is the time integration of the time derivation of itself and comparing the work (power) conjugated pair $\boldsymbol{S} : \dot{\boldsymbol{E}}$ and the relation $\dot{\boldsymbol{C}} = 2\dot{\boldsymbol{E}}$, it follows that the derivation $\partial_{\boldsymbol{C}}\psi = \frac{1}{2}\boldsymbol{S}$ is half of the second Piola Kirchhoff.

$$\psi = \int_{t_0}^{t} \dot{\psi}(\boldsymbol{C}, \boldsymbol{X}) = \int_{t_0}^{t} \frac{\partial \psi}{\partial \boldsymbol{C}} : \dot{\boldsymbol{C}} = \int_{t_0}^{t} \frac{1}{2}\boldsymbol{S} : \dot{\boldsymbol{C}} = \int_{t_0}^{t} \boldsymbol{S} : \dot{\boldsymbol{E}} \tag{4.7}$$

$$\boldsymbol{S} = 2\frac{\partial \psi}{\partial \boldsymbol{C}} = \frac{\partial \psi}{\partial \boldsymbol{E}} \tag{4.8}$$

In section 2 it was seen that the linearisation of the second Piola Kirchhoff can be expressed by the Lagrangian elasticity tensor $\mathbb{C}$. As the second Piola Kirchhoff tensor depends on the derivation of the elastic potential respective to the right Cauchy tensor and the equivalence of the derivations 4.8 it follows for the Lagrangian elasticity tensor.

$$\mathbb{C} = \partial_{\boldsymbol{E}}\boldsymbol{S} = 2\partial_{\boldsymbol{C}}\boldsymbol{S} = 4\partial_{\boldsymbol{C}}\partial_{\boldsymbol{C}}\psi(\boldsymbol{C}, \boldsymbol{X}) \tag{4.9}$$

To establish the derivations after a tensor of the scalar tensor function ψ it is convenient to formulate ψ by the invariants of the tensors I_i on which it is dependent (see remark 13). For the isotropic three dimensional case the elastic potential $\psi(\boldsymbol{C}, \boldsymbol{X})$ is defined by the three invariants of the right Cauchy tensor (see remark 13). Then the derivations can be evaluated by the chain rule as:

$$\boldsymbol{S} = 2\sum_{i=1}^{3} \frac{\partial \psi}{\partial I_i}\frac{\partial I_i}{\partial \boldsymbol{C}} \tag{4.10}$$

The derivations of the tensor invariants $\frac{\partial I_i}{\partial \boldsymbol{C}}$ are given in the appendix 1. For the Lagrangian elasticity tensor the derivation are given by:

$$\mathbb{C} = 4\sum_{I_i}\left[\sum_{I_j}\left[\frac{\partial^2 \psi}{\partial I_i \partial I_j}\frac{I_i}{\boldsymbol{C}} \otimes \frac{I_j}{\boldsymbol{C}} + \frac{\partial \psi}{\partial I_i}\frac{\partial^2 I_i}{\partial \boldsymbol{C}\partial \boldsymbol{C}}\right]\right] \tag{4.11}$$

Remark 13. The invariants of a second order tensor $\boldsymbol{C}$ are given in the three dimensional case.

$$I_1 = tr[\boldsymbol{C}] \tag{4.12}$$

$$I_2 = \frac{1}{2}(tr[\boldsymbol{C}]^2 - tr[\boldsymbol{C}^2]) \tag{4.13}$$

$$I_3 = det[\boldsymbol{C}] \tag{4.14}$$

However, in a more general form, the elastic potential is dependent on more individual tensors. Then the question arises with as many invariants the scalar tensor function can be defined. This leads to the *Theory of Invariants*. In the *Theory of Invariants* a minimal integrity basis is searched for which is an irreducible system of invariants. Here, a short

introduction is given and for a more detailed explanation it is referred to [31].
From [31] it is apparent that the invariants of a set of second order tensors can be expressed by traces of the tensor products. [31] gives also seven rules how the combination of tensor products can be reduced to an integrity basis.

Remark 14. Rules for building an integrity base:

1. The tensor products are products of $\boldsymbol{P}_i$, $\boldsymbol{P}_i^2$ and $\boldsymbol{P}_i^3$ ($i = 1 \dots n$). There is no higher order than 3.
2. If the tensor is in a cubic form it possesses no other factors.
3. There is no product with the same two factors.
4. The first and the last factor cannot be of the same power.
5. $\boldsymbol{P}$ precedes $\boldsymbol{P}^2$ ... (*This is a convention*)
6. Two quadratic terms follow each other.
7. There are no tensor products of order higher than six.

With these rules we get as a result for a symmetric second-order tensor $\boldsymbol{A}$ the traces:

$$tr[\boldsymbol{A}], \quad tr[\boldsymbol{A}^2], \quad tr[\boldsymbol{A}^3] \tag{4.15}$$

For two symmetric second-order tensors $\boldsymbol{A}$, $\boldsymbol{B}$:

$$tr[\boldsymbol{A}], \quad tr[\boldsymbol{A}^2], \quad tr[\boldsymbol{A}^3], \quad tr[\boldsymbol{B}], \quad tr[\boldsymbol{B}^2], \quad tr[\boldsymbol{B}^3] \tag{4.16}$$

$$tr[\boldsymbol{AB}], \quad tr[\boldsymbol{AB}^2], \quad tr[\boldsymbol{A}^2\boldsymbol{B}], \quad tr[\boldsymbol{A}^2\boldsymbol{B}^2] \tag{4.17}$$

Finally for $\boldsymbol{A}$, $\boldsymbol{B}$, $\boldsymbol{C}$ additional to the invariants of the two tensors:

$$tr[\boldsymbol{ABC}], \quad tr[\boldsymbol{A}^2\boldsymbol{BC}], \quad tr[\boldsymbol{B}^2\boldsymbol{CA}], \quad tr[\boldsymbol{C}^2\boldsymbol{AB}] \tag{4.18}$$

$$tr[\boldsymbol{A}^2\boldsymbol{B}^2\boldsymbol{C}], \quad tr[\boldsymbol{B}^2\boldsymbol{C}^2\boldsymbol{A}], \quad tr[\boldsymbol{C}^2\boldsymbol{A}^2\boldsymbol{B}] \tag{4.19}$$

$$\tag{4.20}$$

4.4. Anisotropy

The anisotropy can be formulated in a classical representation with a fixed coordinate system which leads to a respective structure of the elastic moduli tensor (see equation 4.21) or a representation with coordinate independent structural tensors. In the following context only the representation with structural tensors is discussed.

$$\begin{pmatrix} \sigma_{11} \\ \sigma_{22} \\ \sigma_{33} \\ \sigma_{12} \\ \sigma_{23} \\ \sigma_{13} \end{pmatrix} = \begin{pmatrix} c_{1111} & c_{1122} & c_{1133} & c_{1123} & c_{1121} & c_{1112} \\ c_{2211} & c_{2222} & c_{2233} & c_{2223} & c_{2231} & c_{2212} \\ c_{3311} & c_{3322} & c_{3333} & c_{3323} & c_{3331} & c_{3312} \\ c_{2311} & c_{2322} & c_{2333} & c_{2323} & c_{2331} & c_{2312} \\ c_{3111} & c_{3122} & c_{3133} & c_{3123} & c_{3131} & c_{3112} \\ c_{1211} & c_{1222} & c_{1233} & c_{1223} & c_{1231} & c_{1212} \end{pmatrix} \begin{pmatrix} \varepsilon_{11} \\ \varepsilon_{22} \\ \varepsilon_{33} \\ 2\varepsilon_{23} \\ 2\varepsilon_{31} \\ 2\varepsilon_{12} \end{pmatrix} \tag{4.21}$$

A structural tensor characterises the directional dependence of the anisotropic behaviour. For large deformations the anisotropic orientation of the material could change relating to the fixed coordinate system. As the structural tensors are defined in the material configuration, the advantage of structural tensors will become clear: Due to the push

forward operation the structural tensor is rotated accordingly and the orientation change is implicitly established.

$$\boldsymbol{M} = \boldsymbol{a} \otimes \boldsymbol{a} \quad ; \quad ||\boldsymbol{a}|| = 1 \tag{4.22}$$

The second order second Piola Kirchhoff stress tensor $\boldsymbol{S}$ is a response of the material due to some deformation defined by right Cauchy tensor $\boldsymbol{C}$. However, the material structure as well influences the stress response so that the energy state of the material ψ is defined by the deformation $\boldsymbol{C}$ and also by the internal structure which in turn is defined by the second order structural tensor $\boldsymbol{M}$. Such a constitutive energy function has to fulfil the *Principle of Material Indifference*. This principle implies that an arbitrary orthogonal transformation $\boldsymbol{Q}$ applied on the internal material structure and the deformation must lead to the identical energetic state. A material symmetry group $\mathcal{G}$ is defined. For that, assume a set of orthogonal transformations $\boldsymbol{Q} in \mathcal{G}$, which leaves the energy state invariant. Since the stresses are derivations from the strain energy respective to the deformation, this principle implies as well on the stress response.

$$\psi(\boldsymbol{Q}\boldsymbol{C}\boldsymbol{Q}^T, \boldsymbol{Q}\boldsymbol{M}\boldsymbol{Q}^T) = \psi(\boldsymbol{C}, \boldsymbol{M}) \quad \forall \boldsymbol{Q} \in \mathcal{G} \tag{4.23}$$

$$\boldsymbol{S} = 2\partial_{\boldsymbol{C}}\psi(\boldsymbol{C}, \boldsymbol{M}) \tag{4.24}$$

Now the definition of an isotropic material is that an arbitrary transformation $\boldsymbol{Q}$ on the internal structure $\boldsymbol{M}$ but not on the deformation $\boldsymbol{C}$ leads to the same stress response.

$$\psi(\boldsymbol{C}, \boldsymbol{Q}\boldsymbol{M}\boldsymbol{Q}^T)) = \psi(\boldsymbol{C}, \boldsymbol{M}) \tag{4.25}$$

This leads to the consequence that the structural tensor $\boldsymbol{M}$ has to be $\boldsymbol{M} = \lambda\boldsymbol{1}$ were $\lambda \in \mathbb{R}$ and arbitrary and therefore the constitutive equations are independent of the internal structure. In contrast, this is not valid for an anisotropic material.
In figure 4.3, it is shown how the principal directions of strain and stress response do not coincide for an anisotropic material.

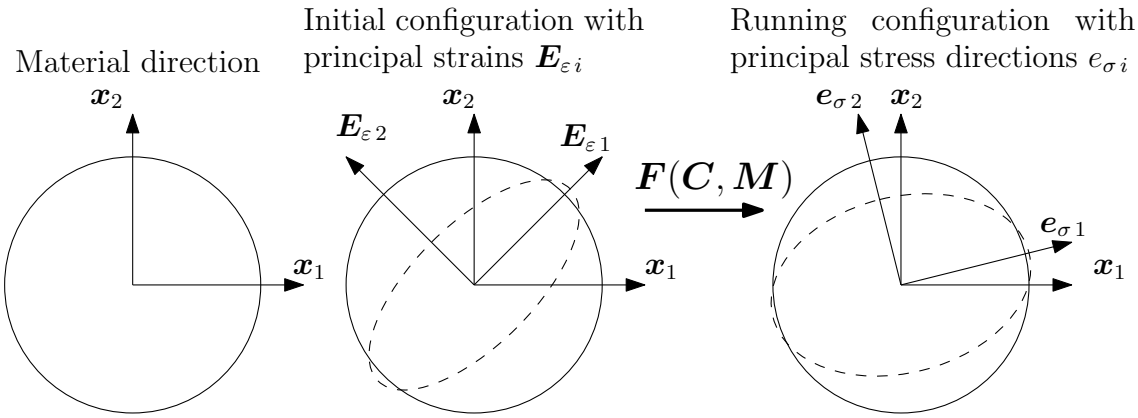

Figure 4.3.: Principal directions

4.4.1. Orthotropic Material

For an orthotropic material all three preferred directions $\boldsymbol{a}_1$, $\boldsymbol{a}_2$, $\boldsymbol{a}_3$ are orthonormal. Therefore, the third direction can be expressed by the other two by $\boldsymbol{a}_3 = \boldsymbol{a}_1 \times \boldsymbol{a}_2$. Which

leads also to the fact that the third structural tensor can be expressed by the other two structural tensors. Since the structural tensors are derived from unit vectors $\boldsymbol{a}$, it follows that the power of the structural tensor is again the structural tensor.

Remark 15. The following simplifications of the structural tensors have to be considered by evaluating the minimum integrity base.

$$\boldsymbol{M}_3 = \boldsymbol{1} - \boldsymbol{M}_1 - \boldsymbol{M}_2 \tag{4.26}$$

$$\boldsymbol{M}^2 = \boldsymbol{M} \tag{4.27}$$

$$\boldsymbol{M}_1 : \boldsymbol{M}_2 = (\boldsymbol{a}_1 \otimes \boldsymbol{a}_2) : (\boldsymbol{a}_2 \otimes \boldsymbol{a}_2) = 0 \tag{4.28}$$

From the previous section 4.3, the integrity base for three second order tensors is given. In fact, an orthotropic material is defined by the three tensors $\boldsymbol{C}$, $\boldsymbol{M}_1$, $\boldsymbol{M}_2$ so that with the simplifications of remark 15 the integrity base follows as in equation 4.30. This basis cannot be reduced any more.

$$\mathcal{I} = \{J_1, J_2, J_3, J_4, J_5, J_6, J_7, I_{\boldsymbol{M}_1}, I_{\boldsymbol{M}_2}\} \tag{4.29}$$

$$\begin{aligned}\mathcal{I} =& \{tr[\boldsymbol{C}], tr[\boldsymbol{C}^2], tr[\boldsymbol{C}^2], tr[\boldsymbol{C}\boldsymbol{M}_1], tr[\boldsymbol{C}^2\boldsymbol{M}_1], \\ & tr[\boldsymbol{C}\boldsymbol{M}_2], tr[\boldsymbol{C}^2\boldsymbol{M}_2], tr[\boldsymbol{M}_1], tr[\boldsymbol{M}_2]\}\end{aligned} \tag{4.30}$$

Since the strain energy function of the Yeoh model is formulated with the principal invariants I_1, I_2, I_3 it is purposeful to replace the first three basic invariants in the integrity base which gives a mixed form of basic and principal invariants.

$$I_1 = tr[\boldsymbol{C}] \tag{4.31}$$

$$I_2 = \frac{1}{2}(tr[\boldsymbol{C}]^2 - tr[\boldsymbol{C}^2]) = tr[cof(\boldsymbol{C})] \tag{4.32}$$

$$I_3 = det[\boldsymbol{C}] \tag{4.33}$$

$$\mathcal{I} = \{I_1, I_2, I_3, J_4, J_5, J_6, J_7, I_{\boldsymbol{M}_1}, I_{\boldsymbol{M}_2}\} \tag{4.34}$$

4.4.2. Transverse Isotropy

For a transverse isotropy only one structural tensor is needed. Therefore, the minimal integrity base follows as:

$$\mathcal{I} = \{tr[\boldsymbol{C}], tr[cof(\boldsymbol{C})], det[\boldsymbol{C}], tr[\boldsymbol{C}\boldsymbol{M}_1], tr[\boldsymbol{C}^2\boldsymbol{M}_1], tr[\boldsymbol{M}_1]\} \tag{4.35}$$

4.5. Isochoric and Volumetric Split

To implement an incompressible material, it is common practice to divide the elastic potential in a volumetric and isochoric part. Where the volumetric part is accountable for the volume dilatation and the isochoric for the deformation. For an incompressible material the volumetric part is zero. Due to numerical reasons the volumetric part is modelled as a penalty function and controlled to be very small by a parameter κ which would normally be the bulk modulus. Such a penalty function is given by [25]. A collection of these potentials can be found in [28].

$$\psi = \psi^{vol}(J) + \psi^{iso}(\bar{\boldsymbol{C}}) \tag{4.36}$$

$$\psi^{vol} = \kappa(J - \ln J - 1) \tag{4.37}$$

Since it is assumed that the volumetric part is small compared to the isochoric part it is also assumed that the contribution of anisotropy and viscoelasticity is only affecting the isochoric part. Therefore, the further contributions to the elastic potentials are only effecting the isochoric part. For that reason also all potentials are dependent on the respective isochoric invariants. As a consequence, the chain rule has to be applied to the derivations of the elastic potential and the derivation $2\frac{\partial \mathbb{Q}}{\partial \boldsymbol{C}} = \mathbb{M}$, $\frac{\partial \boldsymbol{C}}{\partial \boldsymbol{C}} = \mathbb{Q}$ appears. The fourth order tensor $\mathbb{Q}$ could be used to define the deviator operator $DEV[\bullet]$ in the Lagrangian configuration.

$$DEV[\bullet] = [\bullet] : J^{\frac{2}{3}}\mathbb{Q} \tag{4.38}$$

The derivations of those tensors are given in the appendix. This correlation could also be visualised in figure 4.4 as an intermediate configuration.

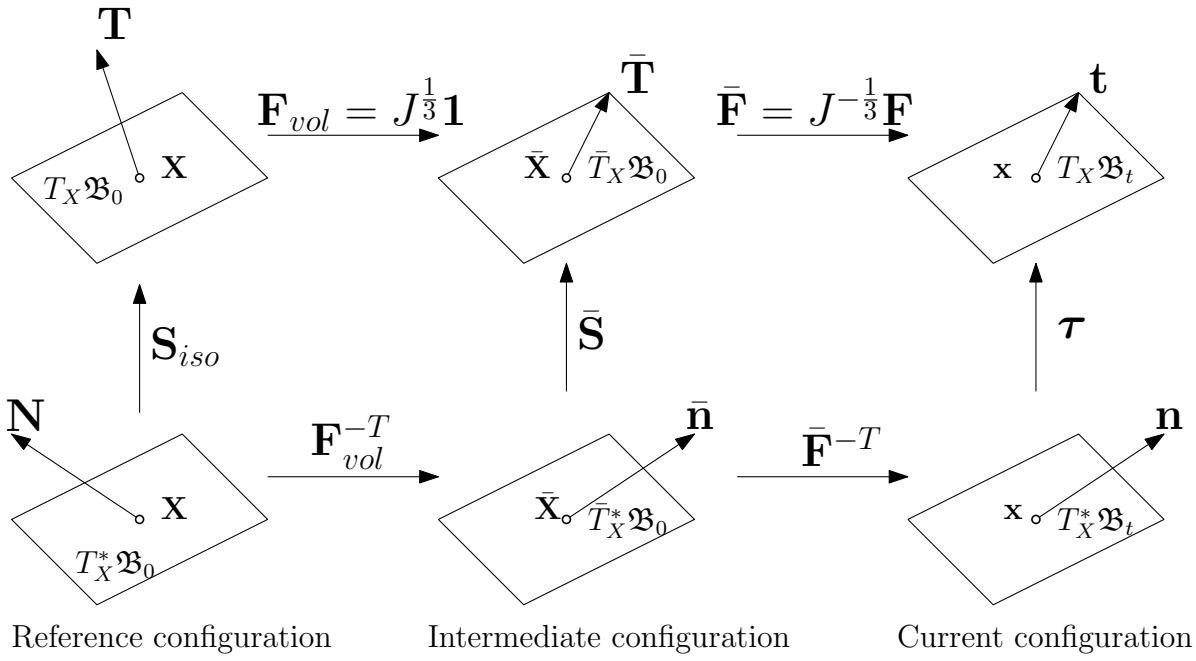

Figure 4.4.: Isochoric intermediate configuration

Remark 16. The deviator operator is in the Lagrangian configuration defined as:

$$DEV[\bullet] = [\bullet] - \frac{1}{3}\left[[\bullet] : \boldsymbol{C}\right]\boldsymbol{C}^{-1} \tag{4.39}$$

$$= [\bullet] : \mathbb{I} - \frac{1}{3}\left[\mathbb{I} : [\bullet] : \boldsymbol{C}\right]\boldsymbol{C}^{-1} \tag{4.40}$$

$$= [\bullet] : \left[\mathbb{I} - \frac{1}{3}\boldsymbol{C} \otimes \boldsymbol{C}^{-1}\right] \tag{4.41}$$

For further information see also [17]. Performing the push forward of the $DEV[\bullet]$ operator on the second Piola Kirchhoff tensor $\boldsymbol{S}$, leads to the well known deviatoric components of

the Cauchy stresses in the spatial configuration.

$$J^{-1}\boldsymbol{F}DEV[\boldsymbol{S}]\boldsymbol{F}^T = J^{-1}\boldsymbol{F}[\boldsymbol{S}]\boldsymbol{F}^T - J^{-1}\frac{1}{3}\left[[\boldsymbol{S}] : \boldsymbol{C}\right]\underbrace{\boldsymbol{F}\boldsymbol{C}^{-1}\boldsymbol{F}^T}_{\mathbf{1}} \tag{4.42}$$

$$= J^{-1}\boldsymbol{F}[\boldsymbol{S}]\boldsymbol{F}^T - J^{-1}\frac{1}{3}tr(\boldsymbol{F}[\boldsymbol{S}]\boldsymbol{F}^T) \tag{4.43}$$

$$= J^{-1}\boldsymbol{F}[\boldsymbol{S}]\boldsymbol{F}^T - \frac{1}{3}tr(J^{-1}\boldsymbol{F}[\boldsymbol{S}]\boldsymbol{F}^T) \tag{4.44}$$

$$= \boldsymbol{\sigma} - \frac{1}{3}tr(\boldsymbol{\sigma})\mathbf{1} = dev(\boldsymbol{\sigma}) \tag{4.45}$$

Where $\mathbb{I}_{ijkl} = \frac{1}{2}(\delta_{ik}\delta_{jl} + \delta_{il}\delta_{jk})$ is the fourth order identity tensor.

4.6. Elastic Potential

The elastic potentials for the anisotropic viscoelastic material are additively divided. In a general way the strain energy function is split into an elastic and a viscoelastic part. Since in this thesis an orthotropic material is used, only two preferred directions or structural tensors $\boldsymbol{M}_1$, $\boldsymbol{M}_2$ are needed. Such an orthotropic material is visualised in figure 4.5 with two perpendicular fibre orientations.

$$\psi^{iso}(\bar{\boldsymbol{C}}, \boldsymbol{M}_1, \boldsymbol{M}_2, \mathfrak{I}_i^I, \mathfrak{A}_j^A, \mathfrak{B}_k^B) = \psi^e(\bar{\boldsymbol{C}}, \boldsymbol{M}_1, \boldsymbol{M}_2) + \psi^v(\bar{\boldsymbol{C}}, \boldsymbol{M}_1, \boldsymbol{M}_2, \mathfrak{I}_i^I, \mathfrak{A}_j^A, \mathfrak{B}_k^B) \tag{4.46}$$

Where $\mathfrak{I}_i^I$, $\mathfrak{A}_j^A$, $\mathfrak{B}_k^B$ are the internal variables in the context of viscoelasticity. The elastic part is further divided into an isotropic and anisotropic elastic potential. Whereas for the viscoelastic part potentials are necessary for each Maxwell (spring) element and for each preferred direction plus isotropic part. The terms of viscoelasticity will be outlined in section 4.10 in more detail.

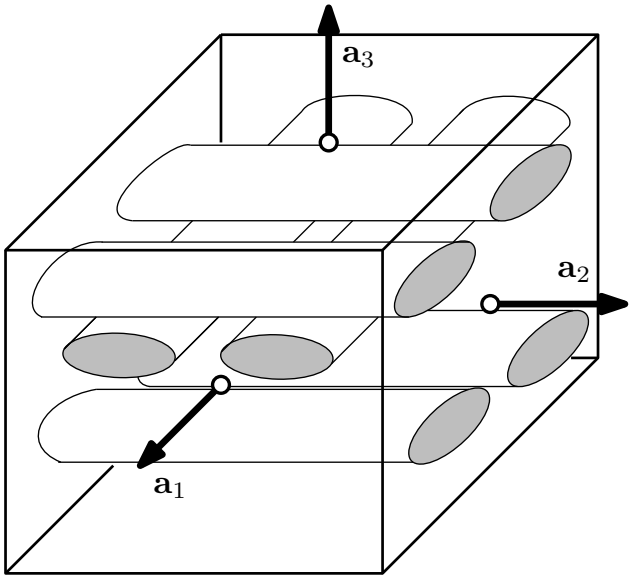

Figure 4.5.: Orthotropic material visualised with two fibre directions

$$\psi^e(\bar{\boldsymbol{C}}, \boldsymbol{M}_1, \boldsymbol{M}_2) = \psi^e_I(\bar{\boldsymbol{C}}) + \psi^e_A(\bar{\boldsymbol{C}}, \boldsymbol{M}_1, \boldsymbol{M}_2) \tag{4.47}$$

$$\psi^v(\bar{\boldsymbol{C}}, \boldsymbol{M}_1, \boldsymbol{M}_2, \mathfrak{I}_i, \mathfrak{A}_j, \mathfrak{B}_k) = \sum_{i=1}^{n^I_{v,i}} \psi^v_i(\bar{\boldsymbol{C}}, \mathfrak{I}_i) + \sum_{j=1}^{n^A_{v,j}} \psi^v_j(\bar{\boldsymbol{C}}, \boldsymbol{M}_1, \mathfrak{A}_j) + \sum_{k=1}^{n^A_{v,k}} \psi^v_k(\bar{\boldsymbol{C}}, \boldsymbol{M}_2, \mathfrak{B}_k) \tag{4.48}$$

4.7. Stresses

The total stress is divided in the respective volumetric, elastic isotropic, elastic anisotropic and the respective viscoelastic parts.

$$\boldsymbol{S} = \boldsymbol{S}_{vol} + \boldsymbol{S}_{iso} = \boldsymbol{S}_{vol} + \boldsymbol{S}^e_I + \boldsymbol{S}^e_A + \boldsymbol{S}^v_I + \boldsymbol{S}^v_A \tag{4.49}$$

Since the isochoric part of the calculation is performed in the isochoric intermediate configuration it is more effective to sum its parts in the aforementioned isochoric intermediate configuration.

$$\bar{\boldsymbol{S}}_{iso} = \underbrace{\bar{\boldsymbol{S}}^e_I + \bar{\boldsymbol{S}}^v_I}_{=\bar{\boldsymbol{S}}_I} + \underbrace{\bar{\boldsymbol{S}}^e_A + \bar{\boldsymbol{S}}^v_A}_{=\bar{\boldsymbol{S}}_A} \tag{4.50}$$

4.8. Lagrangian Elasticity Tensor

Similar to section 4.7 the Lagrangian moduli can be summed.

$$\mathbb{C} = \mathbb{C}_{vol} + \mathbb{C}^e_I + \mathbb{C}^v_I + \mathbb{C}^e_A + \mathbb{C}^v_A \tag{4.51}$$

Again, the sum of the isochoric contribution can be summed up in the isochoric intermediate configuration to reduce the amount of transformations.

$$\bar{\mathbb{C}}_{iso} = \underbrace{\bar{\mathbb{C}}^e_I + \bar{\mathbb{C}}^v_I}_{\bar{\mathbb{C}}_I} + \underbrace{\bar{\mathbb{C}}^e_A + \bar{\mathbb{C}}^v_A}_{\bar{\mathbb{C}}_A} \tag{4.52}$$

4.9. Elastic Properties

4.9.1. Isotropic

The elastic isochoric potential is defined by [33].

$$\psi^e_I = \mu_{10}(\bar{I}_1 - 3) + \mu_{20}(\bar{I}_1 - 3)^2 + \mu_{30}(\bar{I}_1 - 3)^3 \tag{4.53}$$

In figure 4.6, the Yeoh model is compared to the Neo-Hooke model. Here, both models are fitted to experimental data from [32] of an uniaxial stretch test on rubber. Whereas the Neo-Hooke material cannot describe the increase in stiffness at higher stretches, the Yeoh model does. Consequently, the Yeoh model is well suited for large deformations of rubber. If the parameters μ_{20} and μ_{30} are set to zero the model is equivalent to the incompressible Neo-Hooke material model. With that in mind for smaller deformations those parameters can be neglected.

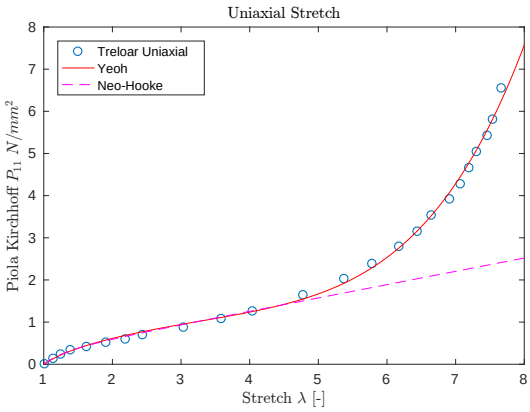

Figure 4.6.: Uniaxial stretch data fit with the Yeoh and Neo-Hooke model

4.9.2. Anisotropic

In general the elastic potential must fulfil physical principles as the balance principles or the stress freeness in the initial state. From a mathematical point of view it is necessary to assure the existence of solutions which implies further restriction on the shape of the elastic potentials. This restriction is enforced by fulfilling the requirements of convexity. Nevertheless, it is advantageous to weaken the requirement of a unique solution stated by convexity. This leads to the definition of poly-convex elastic potential. For a more detailed explanation about poly-convexity and its advantage of a scalar valued tensor function see [28] and [29].
In [29], a poly-convex elastic potential 4.54 for an orthotropic material is outlined. This elastic potential has in addition the advantage that through the set of parameters α_{e1}, α_{e2}, the elastic potential can be made independent of the invariants $\bar{J}_4$, $\bar{J}_5$ by setting them zero or analogous with α_{e3}, α_{e4} and the invariants $\bar{J}_6$, $\bar{J}_7$. Keeping in mind that these invariants are depended on the respective structural tensors, the orthotropic material can easily be made independent of one preferred direction $\boldsymbol{a}_1$ or $\boldsymbol{a}_2$. As mentioned above such a material with one preferred direction is referred to as transverse isotropic.

$$\psi_A = \alpha_{e1}(\bar{J}_4 - 1)^2 + \alpha_{e2}K_{11} + \alpha_{e3}(\bar{J}_6 - 1)^2 + \alpha_{e4}K_{12} + \psi_{\boldsymbol{M}_1} + \psi_{\boldsymbol{M}_2} \tag{4.54}$$

$$K_{11} = (\bar{J}_5 - 1) - (\bar{I}_1 - 3)(\bar{J}_4 - 1) + (\bar{I}_2 - 3) \tag{4.55}$$

$$K_{12} = (\bar{J}_7 - 1) - (\bar{I}_1 - 3)(\bar{J}_6 - 1) + (\bar{I}_2 - 3) \tag{4.56}$$

$$\psi_{\boldsymbol{M}_1} = -2\alpha_{e2}(\bar{J}_4 - 1) \tag{4.57}$$

$$\psi_{\boldsymbol{M}_2} = -2\alpha_{e4}(\bar{J}_6 - 1) \tag{4.58}$$

The potentials $\psi_{\boldsymbol{M}_1}$ and $\psi_{\boldsymbol{M}_2}$ are needed to achieve a stress-free reference configuration.

Remark 17. For convenience the unit vectors of the preferred directions $\boldsymbol{a}_1$ and $\boldsymbol{a}_2$ are described by the angles φ and ϑ as defined in figure 4.7.

$$\begin{pmatrix} \sin\vartheta\cos\varphi \\ \sin\vartheta\sin\varphi \\ \cos\vartheta \end{pmatrix} \tag{4.59}$$

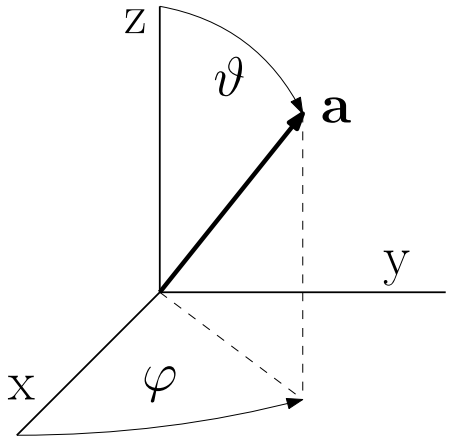

Figure 4.7.: Preferred directions

4.10. Viscoelastic Properties

The viscoelastic behaviour could be modelled with different combinations of springs and dashpots. Some of these combinations are very well-established in practice like the Kelvin Voigt, Maxwell element or standard linear solid model (SLS). A general form is represented by the generalised Maxwell elements as shown in figure 4.8. One Maxwell element is a spring connected serially with a dashpot. In the general form, n Maxwell elements are connected parallel to each other where one branch is purely elastic which represents the elastic properties of section 4.9. Keeping that in mind the viscoelastic

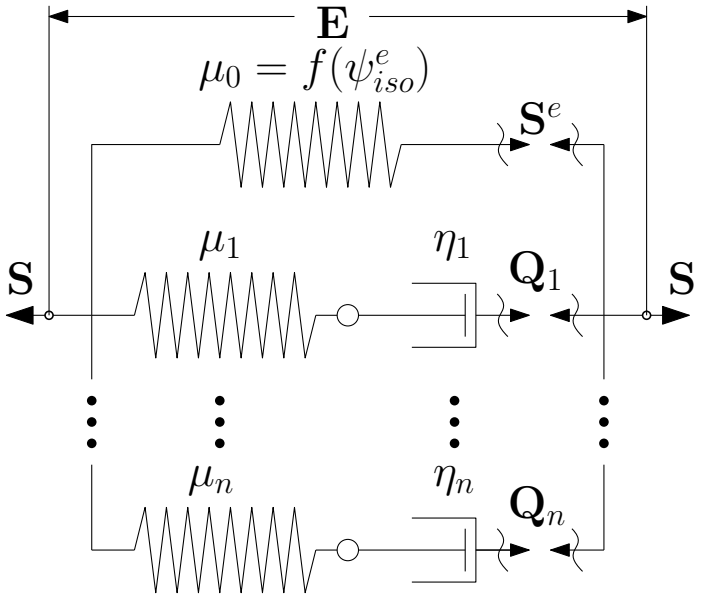

Figure 4.8.: Two Maxwell elements

stresses can be expressed by the sum of the back stresses of the respective Maxwell

elements in the directions $\boldsymbol{a}_1$, $\boldsymbol{a}_2$ and the isotropic ones.

$$\bar{\boldsymbol{S}}_I^v = \sum_{i=1}^{n_v^I} \bar{\boldsymbol{Q}}_i^I \tag{4.60}$$

$$\bar{\boldsymbol{S}}_A^v = \sum_{j=1}^{n_{v,j}^A} \bar{\boldsymbol{Q}}_{a_1,j}^A + \sum_{k=1}^{n_{v,k}^A} \bar{\boldsymbol{Q}}_{a_2,k}^A \tag{4.61}$$

4.10.1. Isotropic

For the isotropic viscoelastic contribution to the elastic potential, the stiffness of the Maxwell elements springs μ_i is just a variation by β_i of the elastic potentials in section 4.9.1 for the sake of simplicity.

$$(\psi_{iso}^v)_i = \beta_i \psi_{iso}^e \tag{4.62}$$

If the differential equation system for the network of the generalised Maxwell elements is solved in the isochoric intermediate configuration as stated in section 4.5 the following evolution equation is found. Since only the deviatoric components of the stress tensors contribute to the viscoelasticity but in the intermediate configuration the stresses are derived by derivations respective to the isochoric quantities, they have generally not only deviatoric components. Therefore, the $DEV[\bullet]$ has to be applied which is derived in section 4.5. At this point this seems unnecessary since the isochoric stresses are in the real material configuration already deviatoric tensors. However, the background of this approach will get clearer in section 4.10.3 where equation 4.63 is discretised.

$$\frac{d}{dt}\left[\bar{\mathbf{Q}}_i^I\right] + \underbrace{\frac{2\mu_i}{\eta_i}}_{\tau_i^{-1}} \bar{\mathbf{Q}}_i^I = \underbrace{\frac{\mu_i}{\mu_0}}_{\beta_i} \frac{d}{dt}\left[DEV[\bar{\mathbf{S}}^e]\right] \tag{4.63}$$

4.10.2. Anisotropic

For the anisotropic viscoelastic contribution respective evolution equations can be formulated in the direction $\boldsymbol{a}_1$, $\boldsymbol{a}_2$.

$$\frac{d}{dt}\left[\bar{\mathbf{Q}}_{a_1,j}^A\right] + \tau_{a_1,j}^{-1} \bar{\mathbf{Q}}_{a_1,j}^A = \frac{d}{dt}\left[DEV[\bar{\mathbf{S}}_{A,a_1,j}^{v,0}]\right] \tag{4.64}$$

$$\frac{d}{dt}\left[\bar{\mathbf{Q}}_{a_2,k}^A\right] + \tau_{a_2,k}^{-1} \bar{\mathbf{Q}}_{a_2,k}^A = \frac{d}{dt}\left[DEV[\bar{\mathbf{S}}_{A,a_2,k}^{v,0}]\right] \tag{4.65}$$

In figure 4.9, the basic structure of the viscoelasticity in the anisotropic model can be seen. At the top, the anisotropic contribution shows both permanent anisotropic elastic stresses $\boldsymbol{S}_{A,1}^e$, $\boldsymbol{S}_{A,2}^e$ and for each Maxwell element the instantaneous stresses $\boldsymbol{S}_{Aa_1,k}^{v,0}$, $\boldsymbol{S}_{Aa_2,j}^{v,0}$. At the bottom, the single isotropic contribution is visualised with three clusters since the isotropy is active in all directions.

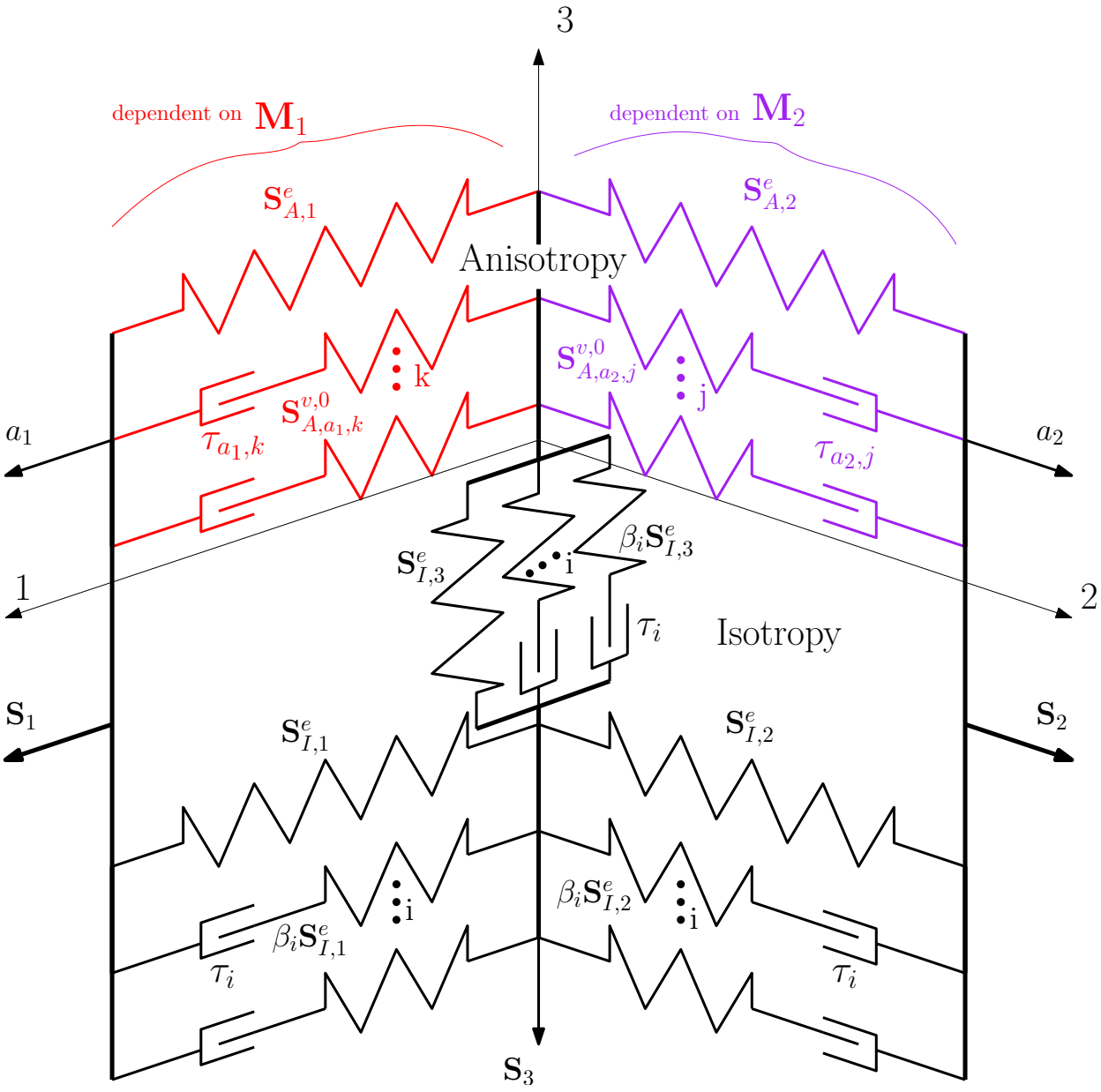

Figure 4.9.: Structure of viscoelastic model

4.10.3. Time Integration

To implement the viscoelastic evolution equation 4.63 into a finite element framework a time discretisation is required. In the non-linear solution algorithm the load is step by step increased so that at this point this incrementation is linked directly to a real time step as well. So that one has to make sure that the step properties for the simulation are set accordingly.
For that reason the evolution equation has to be integrated over this time-step by using the convolution integral. Here, the integration is performed in a general form so that the differentiation between isotropic or anisotropic is omitted.
At first, equation 4.63 is Laplace transformed and simplified with the convolution theorem. See also remark 18 for fundamental dependencies.

$$s\mathscr{L}\left\{\boldsymbol{Q}(t)\right\} - \underbrace{\boldsymbol{Q}(0)}_{=0} + \tau^{-1}\mathscr{L}\left\{\boldsymbol{Q}(t)\right\} = \mathscr{L}\left\{\dot{\boldsymbol{S}}(t)\right\} \tag{4.66}$$

$$\mathscr{L}\left\{\boldsymbol{Q}(t)\right\} = \frac{\mathscr{L}\left\{\dot{\boldsymbol{S}}(t)\right\}}{s+\tau^{-1}} \tag{4.67}$$

$$= \underbrace{\mathscr{L}\left\{\exp\left(-\frac{t}{\tau}\right)\right\}}_{=f(t)} \underbrace{\mathscr{L}\left\{\dot{\boldsymbol{S}}(t)ds\right\}}_{=g(t)} \tag{4.68}$$

$$= \mathscr{L}\left\{\int_0^t \exp\left(-\frac{t-s}{\tau}\right)\dot{\boldsymbol{S}}ds\right\} \tag{4.69}$$

Since it is assumed that at time $t = 0$ all stresses are zero, $\boldsymbol{Q}(0)$ vanishes. Converting back to the time domain by using the inverse Laplace transformation gives an explicit expression for the back-stresses.

$$\boldsymbol{Q}(t) = \int_0^t \exp\left(-\frac{t-s}{\tau}\right)\dot{\boldsymbol{S}}ds \tag{4.70}$$

Remark 18. Using the theorems:

Differentiation:
$$\mathscr{L}\left\{\dot{f}(t)\right\} = s\mathscr{L}\left\{f(t)\right\} - f(0) \tag{4.71}$$

Convolution:
$$\mathscr{L}\left\{f(t)\right\}\mathscr{L}\left\{g(t)\right\} = \mathscr{L}\left\{\int_0^t f(t-s)g(s)ds\right\} \tag{4.72}$$

$$\exp(-at) = \frac{1}{s+a} \tag{4.73}$$

The integral in equation 4.70 is implicitly solved during the analysis. For that the integral has to be approximated by a discrete form which is established by splitting the integral at time t_{n+1} into the known $(\dots)^n$ and unknown $(\dots)^{n+1}$ part. This can be

established by introducing the time step $\Delta t = t_{n+1} - t_n$ in equation 4.70.

$$\boldsymbol{Q}^{n+1} = \int_0^{t_{n+1}} \exp\left(-\frac{t_{n+1}-s}{\tau}\right)\dot{\boldsymbol{S}}ds \tag{4.74}$$

$$= \int_0^{t_n} \exp\left(-\frac{t_n+\Delta t-s}{\tau}\right)\dot{\boldsymbol{S}}ds + \int_{t_n}^{t_{n+1}} \exp\left(-\frac{t_{n+1}-s}{\tau}\right)\dot{\boldsymbol{S}}ds \tag{4.75}$$

$$= \exp\left(-\frac{\Delta t}{\tau}\right)\boldsymbol{Q}^n + \int_{t_n}^{t_{n+1}} \exp\left(-\frac{t_{n+1}-s}{\tau}\right)\dot{\boldsymbol{S}}ds \tag{4.76}$$

Now solving the integral in equation 4.76 with the midpoint rule $\int_{t_n}^{t_{n+1}} f(t) = \Delta t f(\frac{t_{n+1}+t_n}{2})$ and approximating the derivative $\dot{\boldsymbol{S}} = \frac{\boldsymbol{S}^{n+1}-\boldsymbol{S}^n}{\Delta t}$.

$$\boldsymbol{Q}^{n+1} = \exp\left(-\frac{\Delta t}{\tau}\right)\boldsymbol{Q}^n + \Delta t \exp\left(-\frac{t_{n+1}-\frac{t_{n+1}+t_n}{2}}{\tau}\right)\frac{\boldsymbol{S}^{n+1}-\boldsymbol{S}^n}{\Delta t} \tag{4.77}$$

$$= \exp\left(-\frac{\Delta t}{\tau}\right)\boldsymbol{Q}^n + \exp\left(-\frac{\Delta t}{2\tau}\right)\left(\boldsymbol{S}^{n+1}-\boldsymbol{S}^n\right) \tag{4.78}$$

With equation 4.78 an update-equation is found for the back stresses. Where $\boldsymbol{Q}_n$, and $\boldsymbol{S}_n$ have to be stored in every quadrature point at all prescribed increments. For further details see [15].
Considering the result of equation 4.78 for the isotropic and anisotropic viscoelastic part gives the respective update equations:

$$\bar{\boldsymbol{Q}}_i^{I,n+1} = \exp\left(-\frac{\Delta t}{\tau_i}\right)\bar{\boldsymbol{Q}}_i^{I,n} + \exp\left(-\frac{\Delta t}{2\tau_i}\right)\beta_i\left(DEV[\bar{\boldsymbol{S}}_I^{e,n+1}]\Big|^{n+1} - DEV[\bar{\boldsymbol{S}}_I^{e,n}]\Big|^{n}\right) \tag{4.79}$$

$$\bar{\boldsymbol{Q}}_{a_1,j}^{A,n+1} = \exp\left(-\frac{\Delta t}{\tau}\right)\bar{\boldsymbol{Q}}_{a_1,j}^{A,n} + \exp\left(-\frac{\Delta t}{2\tau_{a_1,j}}\right)\left(DEV[\bar{\mathbf{S}}_{A,a_1,j}^{v,0,n+1}]\Big|^{n+1} - DEV[\bar{\mathbf{S}}_{A,a_1,j}^{v,0,n}]\Big|^{n}\right) \tag{4.80}$$

$$\bar{\boldsymbol{Q}}_{a_2,k}^{A,n+1} = \exp\left(-\frac{\Delta t}{\tau}\right)\bar{\boldsymbol{Q}}_{a_2,k}^{A,n} + \exp\left(-\frac{\Delta t}{2\tau_{a_2,k}}\right)\left(DEV[\bar{\mathbf{S}}_{A,a_2,k}^{v,0,n+1}]\Big|^{n+1} - DEV[\bar{\mathbf{S}}_{A,a_2,k}^{v,0,n}]\Big|^{n}\right) \tag{4.81}$$

Since the deviator operator $DEV[\bullet]|^n$ changes in the reference configuration over the iteration it has to be made sure that the right operator is applied.

Remark 19. Keeping in mind that the deviatoric viscoelastic isochoric stresses $DEV[\bar{\boldsymbol{S}}^{n+1}]$ have to be transformed back to the reference configuration with $\mathbb{Q}$ and the properties of a double operation of DEV in remark 20 gives:

$$DEV[\bar{\boldsymbol{S}}^{n+1}] : \mathbb{Q} = J^{-\frac{2}{3}}DEV[DEV[\bar{\boldsymbol{S}}^{n+1}]] = J^{-\frac{2}{3}}DEV[\bar{\boldsymbol{S}}^{n+1}] \tag{4.82}$$

$$= \bar{\boldsymbol{S}}^{n+1} : \mathbb{Q} \tag{4.83}$$

4.10.4. Lagrangian Moduli

The derivatives of the known stresses $(\dots)^n$ equal zero in equation 4.79 to 4.81. Therefore, only the derivation of the $(\dots)^{n+1}$ stresses have to be considered for the Lagrangian

moduli. Considering remark 19 the $DEV[\bullet]$ operator has not to be considered in the derivation of the Lagrangian moduli.

$$\bar{\mathbb{C}}^{v,n+1}_{I,i} = \beta_i \exp\left(-\frac{\Delta t}{2\tau_i}\right) \bar{\mathbb{C}}^{e,n+1}_{I,i} \tag{4.84}$$

$$\bar{\mathbb{C}}^{v,n+1}_{A,a_1,j} = \exp\left(-\frac{\Delta t}{2\tau_{a_1,j}}\right) \bar{\mathbb{C}}^{v,0,n+1}_{A,a_1,j} \tag{4.85}$$

$$\bar{\mathbb{C}}^{v,n+1}_{A,a_2,k} = \exp\left(-\frac{\Delta t}{2\tau_{a_2,k}}\right) \bar{\mathbb{C}}^{v,0,n+1}_{A,a_2,k} \tag{4.86}$$

4.10.5. Simplification

Considering again remark 19, the isotropic viscoelastic stresses are consequently proportional to the isotropic elastic part by $\beta_i \exp\left(-\frac{\Delta t}{2\tau_i}\right)$ and can be added to the elastic part.

$$\bar{\boldsymbol{S}}^{n+1}_I = \bar{\boldsymbol{S}}^{e,n+1}_I + \sum_{i=1}^{n_v^I} \beta_i \exp\left(-\frac{\Delta t}{2\tau_i}\right) \bar{\boldsymbol{S}}^{e,n+1}_I \tag{4.87}$$

$$\bar{\boldsymbol{S}}^{n+1}_I = \underbrace{\left(1 + \sum_{i=1}^{n_v^I} \beta_i \exp\left(-\frac{\Delta t}{2\tau_i}\right)\right)}_{g} \bar{\boldsymbol{S}}^{e,n+1}_I \tag{4.88}$$

$$\bar{\boldsymbol{S}}^{n+1}_I = g\, \bar{\boldsymbol{S}}^{e,n+1}_I \tag{4.89}$$

Where g could be seen as weight or ratio factor of the viscosity. The same applies for the Lagrangian moduli.

$$\bar{\mathbb{C}}^{n+1}_I = \left(1 + \sum_{i=1}^{n_v^I} \beta_i \exp\left(-\frac{\Delta t}{2\tau_i}\right)\right) \bar{\mathbb{C}}^{e,n+1}_I = g\, \bar{\mathbb{C}}^{e,n+1}_I \tag{4.90}$$

$$\tag{4.91}$$

With that the isotropic contribution $\bar{\boldsymbol{S}}_I$ in equation 4.50 can be rewritten as:

$$\bar{\boldsymbol{S}}^{n+1}_I = \bar{\boldsymbol{S}}^{e,n+1}_I + \bar{\boldsymbol{S}}^{n+1}_I \tag{4.92}$$

$$= \left[1 + \sum_{i=1}^{n_v^I} \beta_i \exp\left(-\frac{\Delta t}{2\tau_i}\right)\right] \bar{\boldsymbol{S}}^{e,n+1}_I + \sum_{i=1}^{n_v^I} \underbrace{\left[\exp\left(-\frac{\Delta t}{\tau_i}\right) \bar{\boldsymbol{Q}}^{I,n}_i - \exp\left(-\frac{\Delta t}{2\tau_i}\right) \beta_i\, DEV[\bar{\boldsymbol{S}}^{e,n}_I]\right]}_{\bar{\boldsymbol{H}}^n_{I,i}} \tag{4.93}$$

In [15], the right sum in equation 4.93 is also referred to as the history variables $\bar{\boldsymbol{H}}^n_{I,i}$. Nonetheless, if the time-step changes over the increments it is not possible to save only this history variable for the next increment. Therefore, it was decided to save the back-stresses and deviatoric stresses separately.

The isotropic contribution to the Lagrangian moduli in equation 4.52 is given in equation 4.94.

$$\bar{\mathbb{C}}_I^{n+1} = \left[1 + \sum_{i=1}^{n_v^I} \beta_i \exp\left(-\frac{\Delta t}{2\tau_i}\right)\right] \bar{\mathbb{C}}_I^{e,n+1} \tag{4.94}$$

On the other hand, the double operation of the $DEV[\bullet]$ operator applies also on the anisotropic instantaneous stresses so that the anisotropic contribution $\bar{\boldsymbol{S}}_A$ in equation 4.50 could be rewritten as:

$$\bar{\boldsymbol{S}}_A^{n+1} = \bar{\boldsymbol{S}}_A^{e,n+1} + \sum_{j=1}^{n_{v,j}^A} \bar{\boldsymbol{Q}}_{a_1,j}^{A,n+1} + \sum_{k=1}^{n_{v,k}^A} \bar{\boldsymbol{Q}}_{a_2,k}^{A,n+1} \tag{4.95}$$

$$\begin{aligned}
=&\bar{\boldsymbol{S}}_A^{e,n+1} \\
&+ \sum_{j=1}^{n_{v,j}^A} \bar{\boldsymbol{S}}_{A,a_1,j}^{v,0,n+1} + \sum_{j=1}^{n_{v,j}^A} \left[\exp\left(-\frac{\Delta t}{\tau_{a_1,j}}\right) \bar{\boldsymbol{Q}}_{a_1,j}^{A,n+1} - \exp\left(-\frac{\Delta t}{2\tau_{a_1,j}}\right) DEV[\bar{\boldsymbol{S}}_{A,a_1,j}^{v,0,n}]\Big|^n\right] \\
&+ \sum_{k=1}^{n_{v,k}^A} \bar{\boldsymbol{S}}_{A,a_2,k}^{v,0,n+1} + \sum_{k=1}^{n_{v,k}^A} \left[\exp\left(-\frac{\Delta t}{\tau_{a_2,k}}\right) \bar{\boldsymbol{Q}}_{a_2,k}^{A,n+1} - \exp\left(-\frac{\Delta t}{2\tau_{a_2,k}}\right) DEV[\bar{\boldsymbol{S}}_{A,a_2,k}^{v,0,n}]\Big|^n\right]
\end{aligned} \tag{4.96}$$

For the anisotropic contribution to the total Lagrangian moduli in equation 4.52 equation 4.97 is found.

$$\bar{\mathbb{C}}_{A,n+1} = \bar{\mathbb{C}}_A^{e,n+1} + \exp\left(-\frac{\Delta t}{2\tau_{a_1,j}}\right) \bar{\mathbb{C}}_{A,a_1,j}^{v,0,n+1} + \exp\left(-\frac{\Delta t}{2\tau_{a_2,k}}\right) \bar{\mathbb{C}}_{A,a_2,k}^{v,0,n+1} \tag{4.97}$$

Here, it has to be pointed out that one has to be careful with this simplification of the double operation. Because this simplification is only possible if a double operation of the same $DEV[\bullet]|^{n+1}$ is applied which is not the case for the history variables.
On the other hand, this simplification is necessary to get a consistency at the derivations of the Lagrangian moduli.

4.11. Derivations

As has been mentioned in section 4.5, due to the volumetric split the elastic potentials are dependent on the isochoric invariants so that the chain rule has to be applied.

$$\boldsymbol{S} = 2\partial_{\boldsymbol{C}}\psi^{iso} = 2\partial_{\bar{\boldsymbol{C}}}\psi^{iso} : \partial_{\boldsymbol{C}}\bar{\boldsymbol{C}} = \bar{\boldsymbol{S}}^{iso} : \mathbb{Q} \tag{4.98}$$

$$\mathbb{C}^{iso} = 2\partial_{\boldsymbol{C}}\boldsymbol{S}^{iso} = 2\partial_{\boldsymbol{C}}(\bar{\boldsymbol{S}}^{iso} : \mathbb{Q}) \tag{4.99}$$

$$= (2\partial_{\bar{\boldsymbol{C}}}\bar{\boldsymbol{S}}^{iso} : \partial_{\boldsymbol{C}}\bar{\boldsymbol{C}}) : \mathbb{Q} + 2\bar{\boldsymbol{S}}^{iso} : \partial_{\boldsymbol{C}}\mathbb{Q} \tag{4.100}$$

$$= \mathbb{Q}^T : 4\partial^2_{\bar{\boldsymbol{C}}}\psi^{iso} : \mathbb{Q} + \bar{\boldsymbol{S}}^{iso} : 2\partial^2_{\boldsymbol{C}}\bar{\boldsymbol{C}} \tag{4.101}$$

$$= \mathbb{Q}^T : \bar{\mathbb{C}}^{iso} : \mathbb{Q} + \bar{\boldsymbol{S}}^{iso} : \mathbb{M} \tag{4.102}$$

With that at hand only the isochoric derivations have to be outlined.

Remark 20. An important simplification of the model can be achieved by the identity of the $DEV[DEV[\bullet]] = DEV[\bullet]$ operator.

$$DEV[DEV[\bullet]] = [\bullet]_{ij}\left[\mathbb{I}_{ijkl} - \frac{1}{3}C_{kl}C^{-1}_{mn}\right]\left[\mathbb{I}_{klmn} - \frac{1}{3}C_{ij}C^{-1}_{kl}\right] \tag{4.103}$$

$$= [\bullet]_{ij}\left[\mathbb{I}_{ijkl}\mathbb{I}_{klmn} - \frac{1}{3}C_{ij}C^{-1}_{kl}\mathbb{I}_{klmn} + \frac{1}{9}C_{ij}\underbrace{C^{-1}_{kl}C_{kl}}_{=tr(\boldsymbol{C}\boldsymbol{C}^{-1})=3}C^{-1}_{mn} - \mathbb{I}_{ijkl}\frac{1}{3}C_{kl}C^{-1}_{mn}\right] \tag{4.104}$$

$$= [\bullet]_{ij}\left[\mathbb{I}_{ijmn} - \frac{1}{3}C_{ij}C^{-1}_{mn} + \frac{3}{9}C_{ij}C^{-1}_{mn} - \frac{1}{3}C_{ij}C^{-1}_{mn}\right] \tag{4.105}$$

$$= [\bullet]_{ij}\left[\mathbb{I}_{ijmn} - \frac{1}{3}C_{ij}C^{-1}_{mn}\right] \tag{4.106}$$

By using the symmetry of $\boldsymbol{C}$ it can be shown that the double contraction with the fourth order identity tensor $\mathbb{I}$ gives again $\boldsymbol{C}$.

$$\mathbb{I}_{ijkl}C_{kl} = \frac{1}{2}\left[\delta_{ik}\delta_{jl} + \delta_{il}\delta_{jk}\right]C_{kl} \tag{4.107}$$

$$= \frac{1}{2}\left[\delta_{ik}C_{kl}\delta_{jl} + \delta_{jk}C_{kl}\delta_{il}\right] \tag{4.108}$$

$$= \frac{1}{2}\left[C_{il}\delta_{lj} + C_{jl}\delta_{li}\right] \tag{4.109}$$

$$= \frac{1}{2}\left[C_{ij} + C_{ji}\right] = C_{ij} \tag{4.110}$$

4.11.1. Volumetric

For the derivation of the volumetric part see also [28]. To establish an easy change of the penalty function, the derivation is performed in such a way that the potential ψ_{vol} can be

easily replaced. Where $(\dots)'$ indicates the derivation respective to J.

$$\psi_{vol} = \kappa(J - \ln J - 1) \tag{4.111}$$
$$\psi'_{vol} = \kappa(1 - \frac{1}{J}) \tag{4.112}$$
$$\psi''_{vol} = \kappa\frac{1}{J^2} \tag{4.113}$$
$$\boldsymbol{S}^{vol} = 2\partial_{\boldsymbol{C}}\psi^{vol} = 2\partial_J\psi^{vol}\partial_{\boldsymbol{C}}J \tag{4.114}$$
$$\overset{(A.14)}{=} J\psi'_{vol}\boldsymbol{C}^{-1} \tag{4.115}$$

For the Lagrangian moduli follows:

$$\mathbb{C}^{vol}_{ijkl} = 2\partial_{C_{kl}}(J\psi'_{vol}C^{-1}_{ij}) \tag{4.116}$$
$$= 2\partial_J(J\psi'_{vol})C^{-1}_{ij}\partial_{C_{kl}}J + 2J\psi'_{vol}\partial_{C_{kl}}C^{-1}_{ij} \tag{4.117}$$
$$\overset{(A.34)}{=} J(\psi'_{vol} + J\psi''_{vol})C^{-1}_{ij}C^{-1}_{kl} - 2J\psi'_{vol}\frac{1}{2}\left[C^{-1}_{ik}C^{-1}_{jl} + C^{-1}_{il}C^{-1}_{jk}\right] \tag{4.118}$$
$$= J(\psi'_{vol} + J\psi''_{vol})\boldsymbol{C}^{-1}\otimes\boldsymbol{C}^{-1} - 2J\psi'_{vol}\boldsymbol{C}^{-1}\odot\boldsymbol{C}^{-1} \tag{4.119}$$

Remark 21. Where in analogy to [15] the operator $\odot$ is defined as:

$$(\boldsymbol{A}\odot\boldsymbol{B})_{ijkl} = \frac{1}{2}\left[A_{ik}B_{jl} + A_{il}B_{jk}\right] \tag{4.120}$$

4.11.2. Isotropic

The Yeoh elastic potential is only dependent on the first invariant of $\bar{\boldsymbol{C}}$

$$\psi^e_I = \mu_{10}(\bar{I}_1 - 3) + \mu_{20}(\bar{I}_1 - 3)^2 + \mu_{30}(\bar{I}_1 - 3)^3 \tag{4.121}$$
$$\bar{\boldsymbol{S}}^e_I = 2\partial_{\bar{I}_1}\psi^e_I\partial_{\bar{I}_1}\bar{\boldsymbol{C}} \tag{4.122}$$
$$= 2\left[\mu_{10} + 2\mu_{20}(\bar{I}_1 - 3) + 3\mu_{30}(\bar{I}_1 - 3)^2\right]\mathbf{1} \tag{4.123}$$

For the Lagrangian moduli follows:

$$\bar{\mathbb{C}}^{I,e}_{ijkl} = 4\partial_{\bar{C}_{kl}}(\partial_{\bar{I}_1}\psi^e_I\frac{\partial\bar{I}_1}{\partial\bar{C}_{ij}}) \tag{4.124}$$
$$= 4\left[\partial_{\bar{C}_{kl}}(\partial_{\bar{I}_1}\psi^e_I)\frac{\partial\bar{I}_1}{\partial\bar{C}_{ij}} + \partial_{\bar{I}_1}\psi^e_I\underbrace{\frac{\partial^2\bar{I}_1}{\partial\bar{C}_{ij}\partial\bar{C}_{kl}}}_{\overset{(A.20)}{=}0}\right] \tag{4.125}$$
$$= 4\left[\partial^2_{\bar{I}_1\bar{I}_1}\psi^e_I\frac{\partial\bar{I}_1}{\partial\bar{C}_{ij}}\frac{\partial\bar{I}_1}{\partial\bar{C}_{kl}}\right] \tag{4.126}$$
$$\bar{\mathbb{C}}^e_I \overset{A.20}{=} 4\left[2\mu_{20} + 6\mu_{30}(\bar{I}_1 - 3)\right]\mathbf{1}\otimes\mathbf{1} \tag{4.127}$$
$$\tag{4.128}$$

4.11.3. Anisotropic

The elastic potential is dependent on $\bar{I}_1$, $\bar{I}_2$, $\bar{J}_4$, $\bar{J}_5$, $\bar{J}_6$, $\bar{J}_7$.

$$\begin{aligned}\psi_A^e =&\alpha_{e1}(\bar{J}_4-1)^2\\ &+\alpha_{e2}\left[(\bar{J}_5-1)-(\bar{I}_1-2)(\bar{J}_4-1)+(\bar{I}_2-3)\right]\\ &+\alpha_{e3}(\bar{J}_6-1)^2\\ &+\alpha_{e4}\left[(\bar{J}_5-1)-(\bar{I}_1-2)(\bar{J}_4-1)+(\bar{I}_2-3)\right]\\ &-2\alpha_{e2}(\bar{J}_4-1)\\ &-2\alpha_{e4}(\bar{J}_6-1)\end{aligned} \tag{4.129}$$

The stresses are derived by the chain rule. The derivations after the Invariants are given in the appendix.

$$\bar{\boldsymbol{S}}_A^e = 2\left[\frac{\partial\psi_A^e}{\partial\bar{I}_1}\frac{\partial\bar{I}_1}{\partial\bar{\boldsymbol{C}}}+\frac{\partial\psi_A^e}{\partial\bar{I}_2}\frac{\partial\bar{I}_2}{\partial\bar{\boldsymbol{C}}}+\frac{\partial\psi_A^e}{\partial\bar{J}_4}\frac{\partial\bar{J}_4}{\partial\bar{\boldsymbol{C}}}+\frac{\partial\psi_A^e}{\partial\bar{J}_5}\frac{\partial\bar{J}_5}{\partial\bar{\boldsymbol{C}}}+\frac{\partial\psi_A^e}{\partial\bar{J}_6}\frac{\partial\bar{J}_6}{\partial\bar{\boldsymbol{C}}}+\frac{\partial\psi_A^e}{\partial\bar{J}_7}\frac{\partial\bar{J}_7}{\partial\bar{\boldsymbol{C}}}\right] \tag{4.130}$$

$$\partial_{\bar{I}_1}\psi_A^e = -\alpha_{e2}(\bar{J}_4-1)-\alpha_{e4}(\bar{J}_6-1) \tag{4.131}$$
$$\partial_{\bar{I}_2}\psi_A^e = \alpha_{e2}+\alpha_{e4} \tag{4.132}$$
$$\partial_{\bar{J}_4}\psi_A^e = 2\alpha_{e1}(\bar{J}_4-1)-\alpha_{e2}(\bar{I}_1-3)-2\alpha_{e2} \tag{4.133}$$
$$\partial_{\bar{J}_5}\psi_A^e = \alpha_{e2} \tag{4.134}$$
$$\partial_{\bar{J}_6}\psi_A^e = 2\alpha_{e3}(\bar{J}_6-1)-\alpha_{e4}(\bar{I}_1-3)-2\alpha_{e4} \tag{4.135}$$
$$\partial_{\bar{J}_7}\psi_A^e = \alpha_{e4} \tag{4.136}$$

$$\begin{aligned}\bar{\boldsymbol{S}}_A^e =&2\{\left[-\alpha_{e2}(\bar{J}_4-1)-\alpha_{e4}(\bar{J}_6-1)\right]\mathbf{1}\\ &+\left[\alpha_{e2}+\alpha_{e4}\right](\bar{I}_1\mathbf{1}-\bar{\boldsymbol{C}})\\ &+(2\alpha_{e1}(\bar{J}_4-1)-\alpha_{e2}(\bar{I}_1-3)-2\alpha_{e2})\boldsymbol{M}_1\\ &+\alpha_{e2}(\boldsymbol{M}_1\bar{\boldsymbol{C}}+\bar{\boldsymbol{C}}\boldsymbol{M}_1)\\ &+(2\alpha_{e3}(\bar{J}_6-1)-\alpha_{e4}(\bar{I}_1-3)-2\alpha_{e4})\boldsymbol{M}_2\\ &+\alpha_{e4}(\boldsymbol{M}_2\bar{\boldsymbol{C}}+\bar{\boldsymbol{C}}\boldsymbol{M}_2)\}\\ =&\left[2(\alpha_{e2}+\alpha_{e4})\bar{I}_1-2(\alpha_{e2}(\bar{J}_4-1)-\alpha_{e4}(\bar{J}_6-1))\right]\mathbf{1}\\ &-2(\alpha_{e2}+\alpha_{e4})\bar{\boldsymbol{C}}\\ &+\left[4\alpha_{e1}(\bar{J}_4-1)-2\alpha_{e2}(\bar{I}_1-3)-4\alpha_{e2}\right]\boldsymbol{M}_1\\ &+2\alpha_{e2}(\boldsymbol{M}_1\bar{\boldsymbol{C}}+\bar{\boldsymbol{C}}\boldsymbol{M}_1)\\ &+\left[4\alpha_{e3}(\bar{J}_6-1)-2\alpha_{e4}(\bar{I}_1-3)-4\alpha_{e4}\right]\boldsymbol{M}_2\\ &+2\alpha_{e4}(\boldsymbol{M}_2\bar{\boldsymbol{C}}+\bar{\boldsymbol{C}}\boldsymbol{M}_2)\end{aligned} \tag{4.137}$$

With equation 4.11 and the derivatives of equations 4.131 to 4.136 respective to $\bar{I}_1$, $\bar{I}_2$, $\bar{J}_4$, $\bar{J}_5$, $\bar{J}_6$, $\bar{J}_7$ gives without the zero derivatives:

$$\partial_{\bar{I}_1\bar{J}_4}\psi^e_A = -\alpha_{e2} \tag{4.138}$$
$$\partial_{\bar{I}_1\bar{J}_6}\psi^e_A = -\alpha_{e4} \tag{4.139}$$
$$\partial_{\bar{J}_4\bar{J}_4}\psi^e_A = 2\alpha_{e1} \tag{4.140}$$
$$\partial_{\bar{J}_4\bar{I}_1}\psi^e_A = -\alpha_{e2} \tag{4.141}$$
$$\partial_{\bar{J}_6\bar{J}_6}\psi^e_A = 2\alpha_{e3} \tag{4.142}$$
$$\partial_{\bar{J}_6\bar{I}_1}\psi^e_A = -\alpha_{e4} \tag{4.143}$$

If the first derivatives of the invariants are examined, it will get obvious that only the second derivatives of the invariants $\bar{I}_2$, $\bar{J}_4$ and $\bar{J}_6$ are unequal zero. The second derivatives of these three invariants are provided in the appendix. Introducing these derivatives into equation 4.11 gives:

$$\begin{aligned}\bar{\mathbb{C}}^e_A =& 4\{-\alpha_{e2}(\mathbf{1}\otimes\boldsymbol{M}_1)\\ &-\alpha_{e4}(\mathbf{1}\otimes\boldsymbol{M}_2)\\ &-\alpha_{e2}(\boldsymbol{M}_1\otimes\mathbf{1})\\ &+2\alpha_{e1}(\boldsymbol{M}_1\otimes\boldsymbol{M}_1)\\ &-\alpha_{e4}(\boldsymbol{M}_2\otimes\mathbf{1})\\ &+2\alpha_{e3}(\boldsymbol{M}_2\otimes\boldsymbol{M}_2)\\ &+(\alpha_{e2}+\alpha_{e4})(\mathbf{1}\otimes\mathbf{1}-\mathbb{I})\\ &+\alpha_{e2}(\boldsymbol{M}_1\tilde{\otimes}\mathbf{1}+\mathbf{1}\tilde{\otimes}\boldsymbol{M}_1)\\ &+\alpha_{e4}(\boldsymbol{M}_2\tilde{\otimes}\mathbf{1}+\mathbf{1}\tilde{\otimes}\boldsymbol{M}_2)\}\end{aligned} \tag{4.144}$$

Remark 22. Where the operator $\tilde{\otimes}$ is given as

$$(\boldsymbol{A}\tilde{\otimes}\boldsymbol{B})_{ijkl} = \frac{1}{2}\left(A_{ik}B_{jl}+B_{jk}A_{il}\right) \tag{4.145}$$

4.11.4. Viscoelastic

Since the viscoelastic stiffness is based on the respective potentials of the elastic part (only with other parameters), the derivations are equivalent. So these derivations can be easily obtained by setting $\alpha_{e3}=0$, $\alpha_{e4}=0$ for the preferred direction $\boldsymbol{a}_1$ and $\alpha_{e1}=0$, $\alpha_{e2}=0$ for the preferred direction $\boldsymbol{a}_2$ in equation 4.137 and renaming the parameters α_{ei} accordingly.
Hence, it follows for the preferred direction $\boldsymbol{a}_1$ and Maxwell element number j:

$$\begin{aligned}\bar{S}^v_{A,a_1,j} =& \left[2(\alpha_{v2,j})\bar{I}_1 - 2\alpha_{v2,j}(\bar{J}_4-1)\right]\mathbf{1}\\ &-2\alpha_{v2,j}\bar{\boldsymbol{C}}\\ &+\left[4\alpha_{v1,j}(\bar{J}_4-1)-2\alpha_{v2,j}(\bar{I}_1-3)-4\alpha_{v2,j}\right]\boldsymbol{M}_1\\ &+2\alpha_{v2,j}(\boldsymbol{M}_1\bar{\boldsymbol{C}}+\bar{\boldsymbol{C}}\boldsymbol{M}_1)\end{aligned} \tag{4.146}$$

$$\begin{aligned}\bar{\mathbb{C}}^{v}_{A,a_1,j} =& 4\{-\alpha_{v2,j}(\mathbf{1}\otimes\boldsymbol{M}_1)\\ &-\alpha_{v2,j}(\boldsymbol{M}_1\otimes\mathbf{1})\\ &+2\alpha_{v1,j}(\boldsymbol{M}_1\otimes\boldsymbol{M}_1)\\ &+\alpha_{v2,j}(\mathbf{1}\otimes\mathbf{1}-\mathbb{I})\\ &+\alpha_{v2,j}(\boldsymbol{M}_1\tilde{\otimes}\mathbf{1}+\mathbf{1}\tilde{\otimes}\boldsymbol{M}_1)\}\end{aligned} \tag{4.147}$$

For the preferred direction $\boldsymbol{a}_2$ and Maxwell elements number k the stresses and Lagrangian moduli are given as:

$$\begin{aligned}\bar{S}^{v}_{A,a_2,k} =& \left[2\alpha_{v4,k}\bar{I}_1-\alpha_{v4,k}(\bar{J}_6-1))\right]\mathbf{1}\\ &-2\alpha_{v4,k}\bar{\boldsymbol{C}}\\ &+\left[4\alpha_{v3,k}(\bar{J}_6-1)-2\alpha_{v4,k}(\bar{I}_1-3)-4\alpha_{v4,k}\right]\boldsymbol{M}_2\\ &+2\alpha_{v4,k}(\boldsymbol{M}_2\bar{\boldsymbol{C}}+\bar{\boldsymbol{C}}\boldsymbol{M}_2)\end{aligned} \tag{4.148}$$

$$\begin{aligned}\bar{\mathbb{C}}^{v}_{A,a_2,k} =& 4\{-\alpha_{v4,k}(\mathbf{1}\otimes\boldsymbol{M}_2)\\ &-\alpha_{v4,k}(\boldsymbol{M}_2\otimes\mathbf{1})\\ &+2\alpha_{v3,k}(\boldsymbol{M}_2\otimes\boldsymbol{M}_2)\\ &+\alpha_{v4,k}(\mathbf{1}\otimes\mathbf{1}-\mathbb{I})\\ &+\alpha_{v4,k}(\boldsymbol{M}_2\tilde{\otimes}\mathbf{1}+\mathbf{1}\tilde{\otimes}\boldsymbol{M}_2)\}\end{aligned} \tag{4.149}$$

4.12. Algorithm

With that at hand the algorithm can be denoted as:

1. Load previous state variables $\boldsymbol{Q}_i^{I,n}$, $DEV[\bar{\boldsymbol{S}}_{A,a_2,j}^{e,n}]\Big|^n$, $\boldsymbol{Q}_{a_1,j}^{A,n}$, $DEV[\bar{\boldsymbol{S}}_{A,a_1,j}^{v,0,n}]\Big|^n$, $\boldsymbol{Q}_{a_2,k}^{A,n}$, $DEV[\bar{\boldsymbol{S}}_{A,a_2,k}^{v,0,n}]\Big|^n$.

2. Evaluate the determinant J , the right Cauchy tensor $\boldsymbol{C}$, the isochoric right Cauchy tensor $\bar{\boldsymbol{C}}$ and the invariants $\bar{I}_1$, $\bar{J}_4$, $\bar{J}_6$.

3. Evaluate the volumetric stresses $\boldsymbol{S}_{vol}^{n+1}$ (eq. 4.115) and Lagrange moduli $\mathbb{C}_{vol}^{n+1}$ (eq. 4.119).

4. Evaluate the isochoric elastic stresses $\bar{\boldsymbol{S}}_I^{e,n+1}$ (eq. 4.123) and $\bar{\boldsymbol{S}}_A^{e,n+1}$ (eq. 4.137).

5. Compute the instantaneous stresses $\bar{\boldsymbol{S}}_{A,a_1,j}^{v,0,n+1}$ (eq. 4.146), $\bar{\boldsymbol{S}}_{A,a_2,k}^{v,0,n+1}$ (eq. 4.148).

6. Evaluate the respective deviatoric stresses $DEV[\bar{\boldsymbol{S}}_I^{e,n+1}]\Big|^{n+1}$, $DEV[\bar{\boldsymbol{S}}_{A,a_1,j}^{v,0,n+1}]\Big|^{n+1}$ and $DEV[\bar{\boldsymbol{S}}_{A,a_2,k}^{v,0,n+1}]\Big|^{n+1}$.

7. Compute the respective isochoric Lagrange moduli $\bar{\mathbb{C}}_I^{e,n+1}$ (eq. 4.127), $\bar{\mathbb{C}}_A^{e,n+1}$ (eq. 4.144), $\bar{\mathbb{C}}_{A,a_1,k}^{v,0,n+1}$ (eq. 4.147), $\bar{\mathbb{C}}_{A,a_2,k}^{v,0,n+1}$ (eq. 4.149).

8. Update the back stresses $\bar{\boldsymbol{Q}}_i^{I,n+1}$ (eq. 4.79), $\bar{\boldsymbol{Q}}_{a_1,k}^{A,n+1}$ (eq. 4.80), $\bar{\boldsymbol{Q}}_{a_2,k}^{A,n+1}$ (eq. 4.81).

9. Compute the sum of the isotropic stresses (eq. 4.93) and Lagrange moduli (eq. 4.94).

10. Compute the sum of the anisotropic stresses (eq. 4.96) and Lagrange moduli (eq. 4.97).

11. Compute the isochoric stress (eq. 4.50) and Lagrange moduli (eq. 4.52).

12. Compute the total isochoric stresses and Lagrange moduli
$\boldsymbol{S}_{iso}^{n+1} = \bar{\boldsymbol{S}}_{iso}^{n+1} : \mathbb{Q}, \qquad \mathbb{C}_{iso}^{n+1} = \mathbb{Q}^T : \mathbb{C}_{iso}^{n+1} : \mathbb{Q}.$

13. Compute the total stresses and Lagrange moduli
$\boldsymbol{S}^{n+1} = \boldsymbol{S}_{iso}^{n+1} + \boldsymbol{S}_{vol}, \qquad \mathbb{C}^{n+1} = \mathbb{C}_{iso}^{n+1} + \mathbb{C}_{vol}^{n+1}.$

5. Verification

5.1. Uniaxial Tension Test

To show the orthotropic viscoelasticity behaviour, a simple uniaxial deformation is calculated. For that purpose, the deformation gradient is given in a diagonal form with the principal stretches λ_i.

$$\boldsymbol{F} = \begin{pmatrix} \lambda_1 & 0 & 0 \\ 0 & \lambda_2 & 0 \\ 0 & 0 & \lambda_3 \end{pmatrix} \tag{5.1}$$

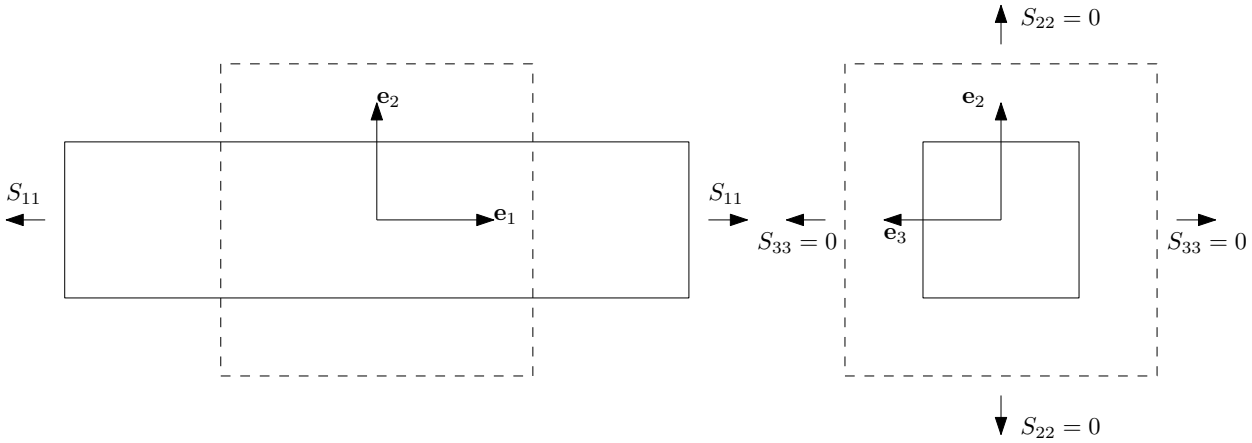

Figure 5.1.: Uniaxial stretch test

Since only the stretch λ_1 is prescribed and the surfaces in $\boldsymbol{e}_1$ and $\boldsymbol{e}_2$ direction have to be stress-free only the stresses S_{11} can evolve. With these boundary conditions, the stress components S_{22}, S_{33} have to be zero, the stretches λ_2, λ_3 can be evaluated. This results in a non-linear equation system that has to be solved with a Newton algorithm. Since for the Newton algorithm the derivatives of $\boldsymbol{S}$ are needed and the derivatives respective to the right Cauchy tensor $\boldsymbol{C}$ are already known it is more convenient to formulate the Newton algorithm with $\boldsymbol{C}$.

$$\hat{\boldsymbol{S}} = \begin{pmatrix} S_{22} \\ S_{33} \end{pmatrix} \qquad \hat{\boldsymbol{C}} = \begin{pmatrix} C_{22} \\ C_{33} \end{pmatrix} \tag{5.2}$$

$$\hat{\mathbb{C}} = \begin{pmatrix} \mathbb{C}_{2222} & \mathbb{C}_{2233} \\ \mathbb{C}_{3322} & \mathbb{C}_{3333} \end{pmatrix} \tag{5.3}$$

$$\frac{1}{2}\underbrace{2\frac{\partial \boldsymbol{S}_i}{\partial \hat{\boldsymbol{C}}_i}}_{\hat{\mathbb{C}}}(\hat{\boldsymbol{C}}_{i+1}-\hat{\boldsymbol{C}}_i)+\hat{\boldsymbol{S}}=\boldsymbol{0} \tag{5.4}$$

$$\hat{\boldsymbol{C}}_{i+1}=\hat{\boldsymbol{C}}_i-2\,\hat{\mathbb{C}}^{-1}\hat{\boldsymbol{S}}_i \tag{5.5}$$

$$||\hat{\boldsymbol{S}}_{i+1}||=\sqrt{\hat{\boldsymbol{S}}_{i+1}\cdot\hat{\boldsymbol{S}}_{i+1}}<tol \tag{5.6}$$

5.1.1. Results Linear Loading

In this simulation, the stretch λ_1 increase with stretch rates $\dot{\lambda}=1\times10^{-2}$, $\dot{\lambda}=5\times10^{-3}$ and $\dot{\lambda}=2\times10^{-3}$ from 1 up to 2. The results are compared to that of the diploma thesis of Dirk Liefeith [21]. Where REF indicates the reference and SIM the simulated or calculated results. The parameters are defined in table 5.1. The material model is implemented in the in-house finite element program SOOFEA for this test. The preferred material directions coincide with the triad of the Cartesian coordinate system: $\boldsymbol{a}_i=\boldsymbol{e}_i$ for $i=1,2,3$.

Isotropic	κ	μ_{10}	μ_{20}	μ_{30}				
	160	0.1489×10^{-4}	-8.551×10^{-3}	6.175×10^{-6}				
		Viscosity(i)	τ_i	β_i				
		1	1.0	0.0				
		2	1.0	0.0				
		3	1.0	0.0				
		4	1.0	0.0				
Anisotropic	α_{e1}	α_{e2}	α_{e3}	α_{e4}				
	0.5	0.6	0.25	0.25				
		Viscosity(j)	$\tau_{a_1,j}$	$\tau_{a_2,j}$	$\alpha_{v1,j}$	$\alpha_{v2,j}$	$\alpha_{v3,j}$	$\alpha_{v4,j}$
		1	10.0	10.0	0.610	0.620	0.410	0.420
		2	10.0	10.0	0.710	0.720	0.450	0.450
		3	10.0	10.0	0.510	0.520	0.350	0.350
		4	10.0	10.0	0.410	0.420	0.310	0.320

Table 5.1.: Input parameters for brick tensile test

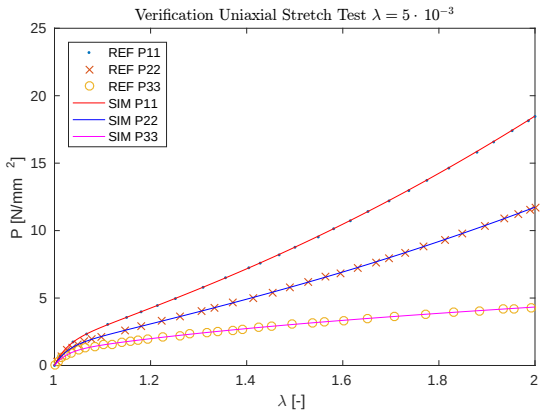

Figure 5.2.: Uniaxial stretch test

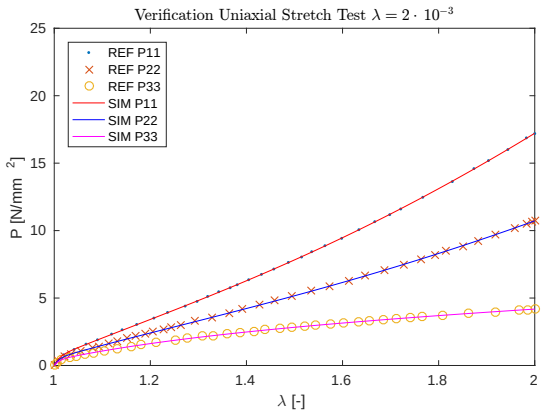

Figure 5.3.: Uniaxial stretch test

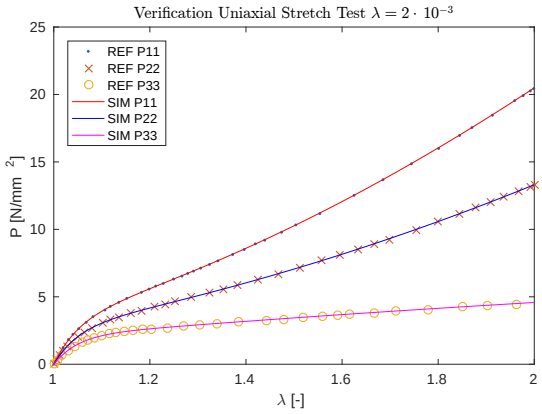

Figure 5.4.: Uniaxial stretch test

5.1.2. Results Cyclic Loading

In this simulation, the stretch λ_1 is varied in one cycle with stretch rates $\dot{\lambda} = 5 \times 10^{-3}$, $\dot{\lambda} = 2.5 \times 10^{-3}$ and $\dot{\lambda} = 1 \times 10^{-3}$ from 1 up to a maximum of 2 and to a minimum of 0.75. This analysis should show the hysteresis that can be described with viscoelasticity.

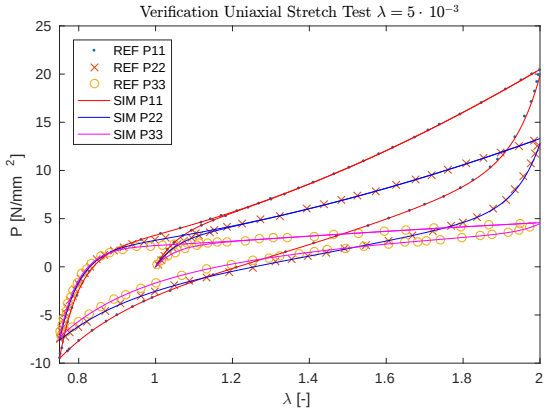

Figure 5.5.: Uniaxial stretch test

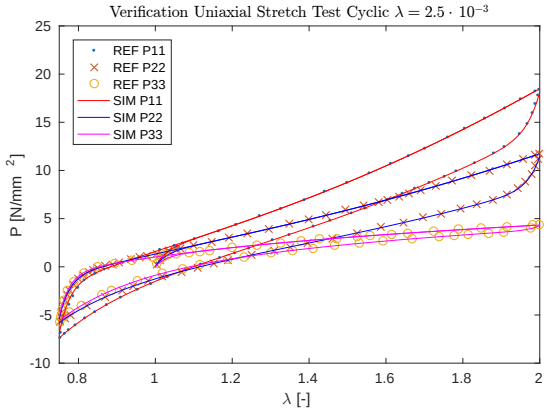

Figure 5.6.: Uniaxial stretch test

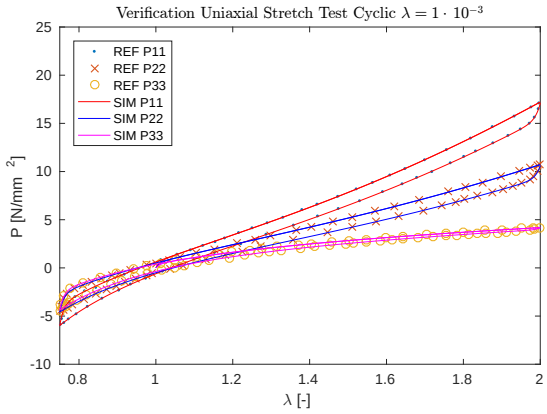

Figure 5.7.: Uniaxial stretch test

5.1.3. Cook's Membrane

A purely elastic test is performed on a three dimensional version of the Cook's membrane problem to show the effects of anisotropy. The material model is implemented into the finite element software package ABAQUS using the user subroutine UMAT for this problem. The cantilever was discretised with an edge subdivision of 20 in length and 10 in height and 2 in depth which sums up to 400 elements. As element type the hybrid element C3D8RH with enhanced hourglass control was used. The parameters for the

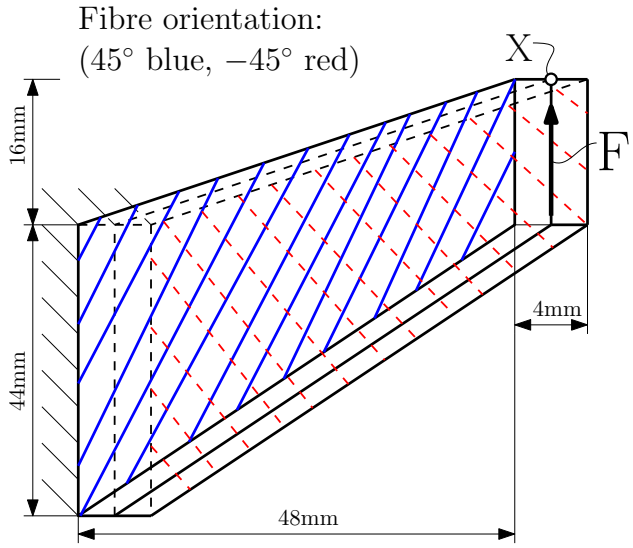

Figure 5.8.: Cook's Membrane problem

simulation are specified in table 5.2. Figure 5.10 shows the displacements of node X.

Isotropic	κ	μ_{10}	μ_{20}	μ_{30}
	100.0	0.2565	3.325×10^{-3}	3.518×10^{-7}
Anisotropic	α_{e1}	α_{e2}		
	0.5	0.2		
Force	$\boldsymbol{F}$			
	20 N			

Table 5.2.: Input parameter for Cook's Membrane simulation

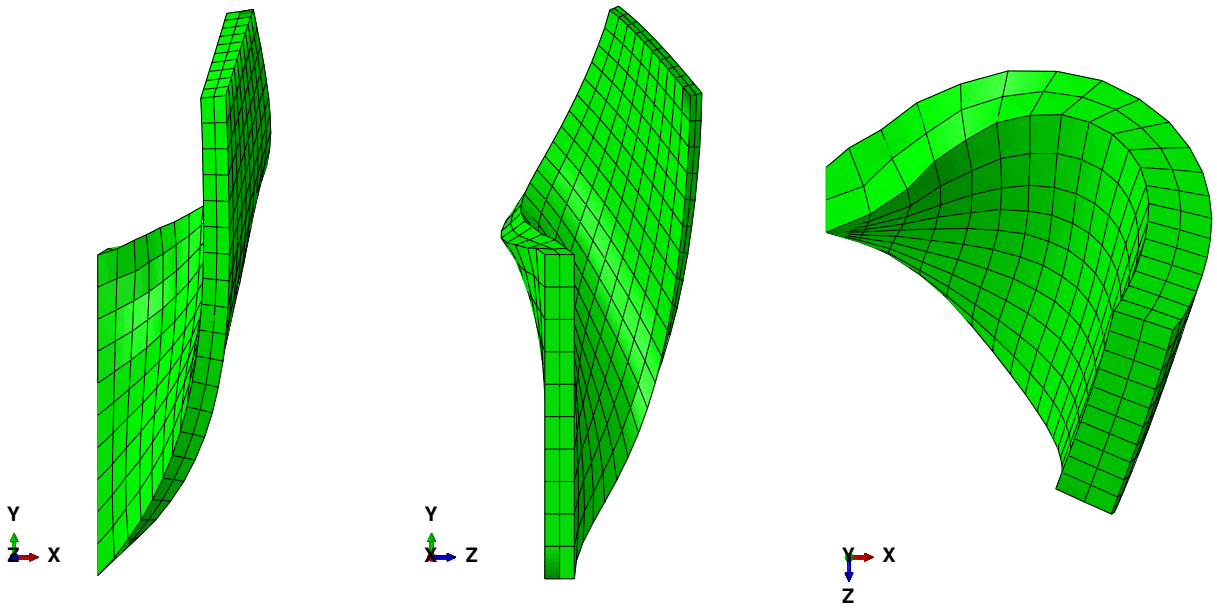

Figure 5.9.: ABAQUS simulation of Cook's Membrane

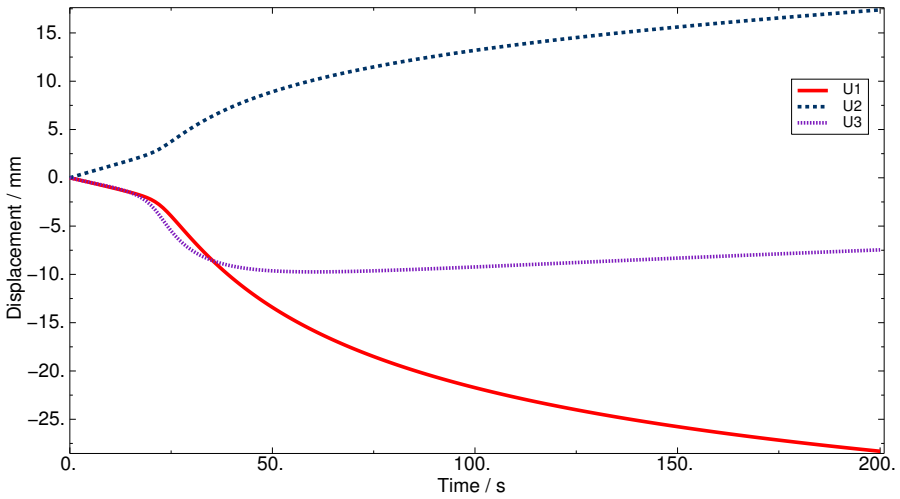

Figure 5.10.: Displacements U1 in x-direction, U2 in y-direction and U3 in z-direction for point X.

width	$32\,\mu m$
thickness	$7.45\,\mu m$
length	$1000\,\mu m$

Table 5.3.: Geometry of pulp fibre

5.1.4. Tensile Test of a Pulp Fibre

To show how the anisotropy can affect the behaviour of pulp fibres a simulation is performed on a simplified model of the pulp fibre. A pulp fibre consists of various layers with fibre reinforcement. These fibres are helically aligned around the fibre tube. However, in a dried state the fibres are often flattened so that the fibre could be approximated by a bi-material bar with two mirrored fibre orientations. The geometrical dimensions of the pulp fibre are based on article [10]. The material parameters where chosen to show clearly the anisotropic behaviour and the relaxation.

The structured mesh was generated with an edge subdivision of 200 in length, 10 in

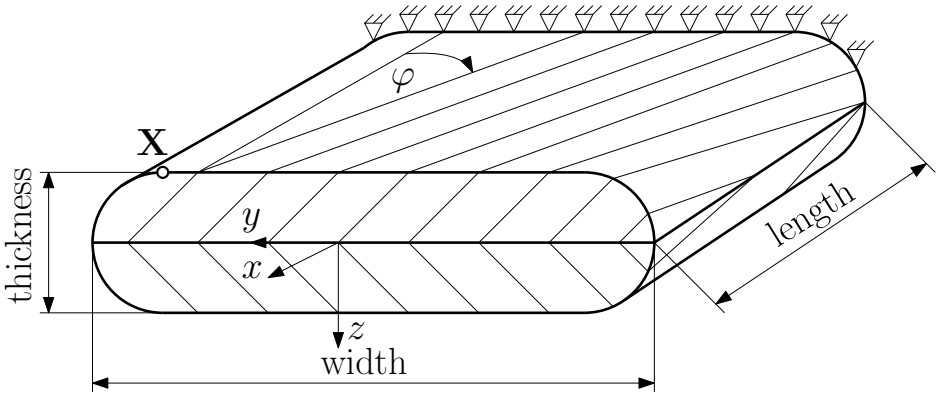

Figure 5.11.: Specification of pulp fibre

Isotropic	κ	μ_{10}	μ_{20}	μ_{30}	
	10	2.947×10^{-4}	-3.01×10^{-5}	5.605×10^{-6}	
		Viscosity(i)	τ_i	β_i	
		1	100.0	0.2	
		2	10.0	0.3	
Anisotropic	α_{e1}	α_{e2}			
	0.001	0.002			
		Viscosity(j)	$\tau_{a_1,j}$	$\alpha_{v1,j}$	$\alpha_{v2,j}$
		1	10.0	0.011	0.012
		2	10.0	0.021	0.022

Table 5.4.: Input parameters for brick tensile test

width, 4 in thickness and the radius with 3. As element type an eight node hybrid element with enhanced reduced integration C3D8RH was used. The pulp fibre was fixed on one side and pulled in x-direction (U1 displacement) as shown in figure 5.14. The simulation is again performed using ABAQUS and UMAT.

In figure 5.14, the relaxation is clearly visible of the node point X after the prescription.

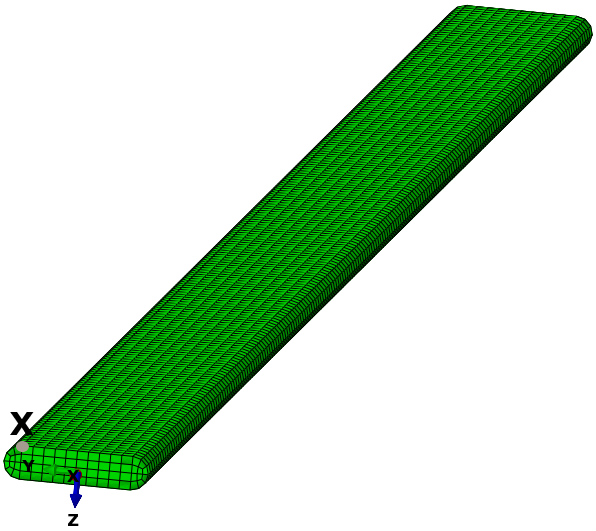

Figure 5.12.: Undeformed pulp fibre $t = 0$

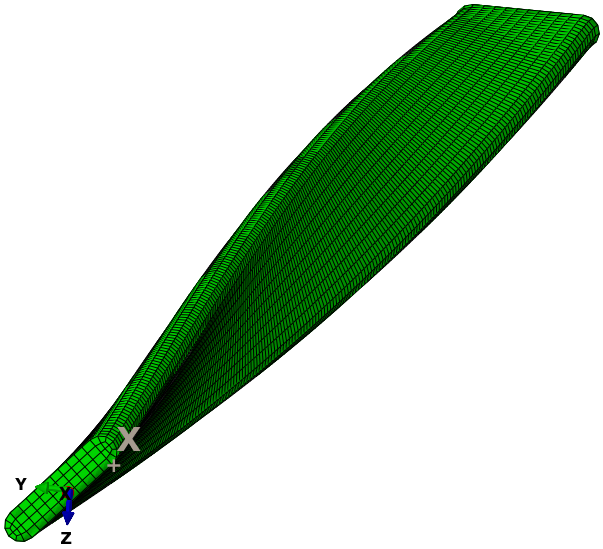

Figure 5.13.: Torsion of the pulp fibre at $t = 75s$

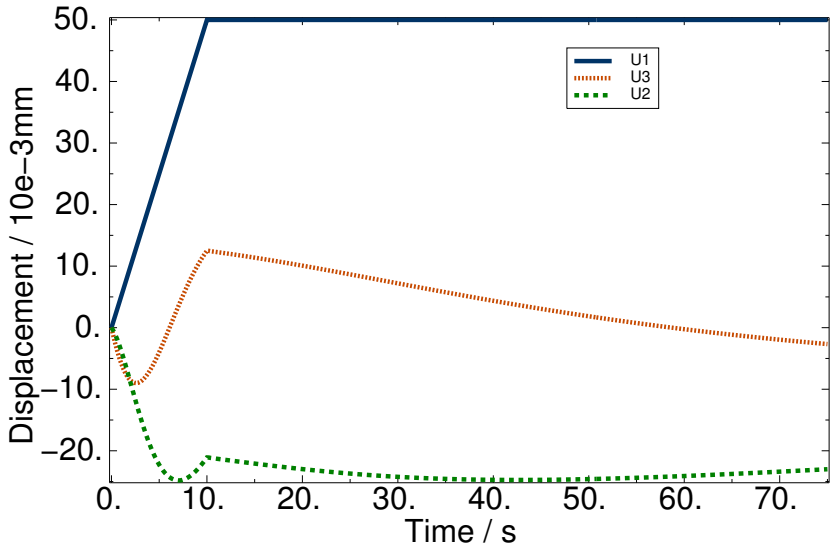

Figure 5.14.: Displacement of point X

6. Parameter Influence

6.1. Elastic Parameter Influence

From the theory manual of Abaqus [1] it has become apparent that for the Yeoh model 4.53 the parameters are commonly chosen to be that $\mu_{10} = 1.0$ is of order one, $\mu_{20} = -0.1 \div 0.01$ negative and one to two orders smaller and $\mu_{30} = 0.01 \div 0.0001$ up to four order smaller. These parameters generate an S-shape of the stress strain behaviour. If μ_{20} and μ_{30} are set to zero the model is equivalent to the incompressible neo-Hookean model.

To get hold of the anisotropic parameter influence, it is advisable to look at the instantaneous anisotropic viscous second Piola Kirchhoff stresses of equation 4.146.

$$\begin{aligned}\bar{S}^{v}_{A,a_1} = &\left[2(\alpha_{v2})\bar{I}_1 - 2\alpha_{v2}(\bar{J}_4 - 1)\right]\mathbf{1} \\ &- 2\alpha_{v2}\bar{\boldsymbol{C}} \\ &+ \left[4\alpha_{v1}(\bar{J}_4 - 1) - 2\alpha_{v2}(\bar{I}_1 - 3) - 4\alpha_{v2}\right]\boldsymbol{M}_1 \\ &+ 2\alpha_{v2}(\boldsymbol{M}_1\bar{\boldsymbol{C}} + \bar{\boldsymbol{C}}\boldsymbol{M}_1)\end{aligned} \tag{6.1}$$

The invariants $\bar{J}_4$ and $\bar{J}_6$ in equation 4.148 can be interpreted in a physical way. Since they are the double contraction of the right Cauchy tensor and the structural tensor $\boldsymbol{C} : \boldsymbol{M}$, they can be interpreted as the squares of the stretches projected in the preferred direction[1]. Hence, in equation 6.1 the parameters of the preferred direction $\boldsymbol{a}_1$ can be discussed. The same applies to the other preferred direction $\boldsymbol{a}_2$.

The parameter α_{v1} is only related to the structural tensor $\boldsymbol{M}_1$ and the invariant $\bar{J}_4$ and therefore this parameter has its influence purely on the preferred direction. The parameter α_{v2} is also a factor of the right Cauchy tensor $\bar{\boldsymbol{C}}$ and the first invariant $\bar{I}_1$, therefore, also some isotropic contribution is expected.

6.2. Viscoelastic Parameter Influence

To get a better understanding of how the material parameters influence the anisotropic viscoelastic material response, the evolution of the stresses in tensile tests are analysed. Since these test are displacement-controlled with a constant stretch rate, the back stresses Q can only evolve if the parameters are chosen accordingly. This becomes clear if the following is considered: The dashpot directly influences how much the spring is tensioned. So, if the viscosity of the dashpot is high or $\tau \gg$ then the spring is completely active and the back stresses are high. On the contrary if $\tau \ll$ then the spring is hardly active since the dashpot is preventing a 'wind up' of the spring. Which means that the back stresses are low. So, on one point the parameter τ influences the maximum stress response but on the other point also the relaxation process over time, how fast the back stresses decay.

[1] For more details see [16]

To show the influence of the relaxation time it is important to look at the update algorithm 6.3 taken in a simplified form and a linear increase of the instantaneous stresses is assumed in figure 6.2.

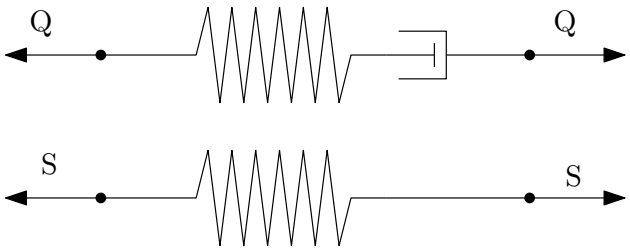

Figure 6.1.: Dashpot & Spring

$$H_i = \exp(-\frac{dt}{\tau})Q_i - \exp(-\frac{dt}{2\tau})S_i \tag{6.2}$$

$$Q_{i+1} = H_i + \exp(-\frac{dt}{2\tau})S_{i+1} \tag{6.3}$$

The anisotropic viscous instantaneous stresses are hypothetical stresses that evolve if due to fast loading the dashpot is completely rigid or inactive. If it is assumed that these stresses evolve linearly over time, as it can be seen in 6.2 that at a certain point the actual back stresses Q do not increase anymore which means that the increase of the instantaneous stress (spring) is in equilibrium with the loss of stresses caused by the history variables (dashpot).

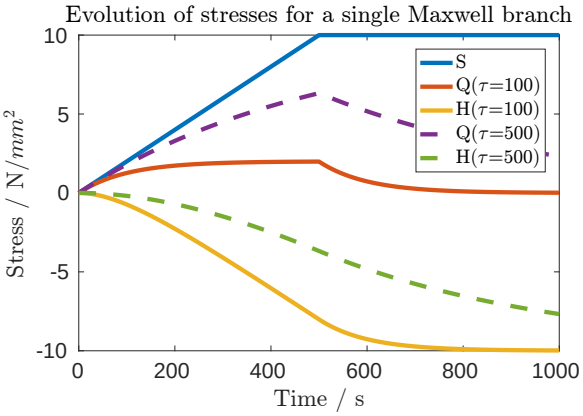

Figure 6.2.: Evolution of stresses

6.3. Uniaxial Tension Test

Once more, a uniaxial stretch test of section 5.1 is done for one anisotropic Maxwell branch where the preferred direction is aligned into the stretch direction. With the parameters of table 6.1.

In figure 6.4 it can be seen that both perpendicular stretches λ_2, λ_3 are equivalent. If now the preferred direction is rotated by $45°$ (this requires $\boldsymbol{a}_1 = [\frac{\sqrt{2}}{2}, \frac{\sqrt{2}}{2}, 0]$) then a difference in both stretches is expected. In figure 6.6 this can be observed.

κ	1000
α_{v1}	1.11
α_{v2}	1.11
τ	100

Table 6.1.: Input parameters

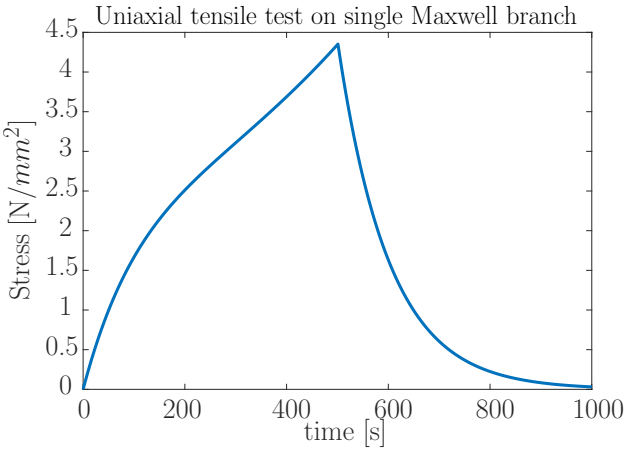

Figure 6.3.: Back stresses at uniaxial drive test

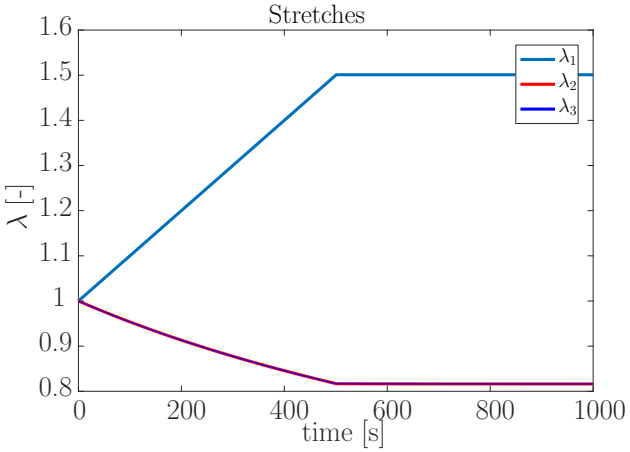

Figure 6.4.: Stretches at uniaxial drive test

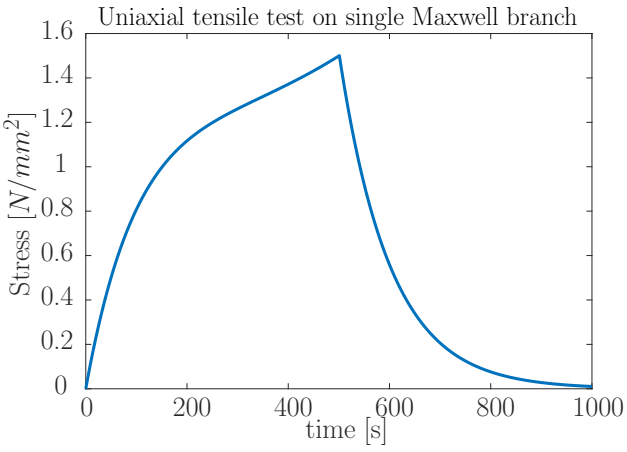

Figure 6.5.: Back stresses evolution at 45° preferred direction

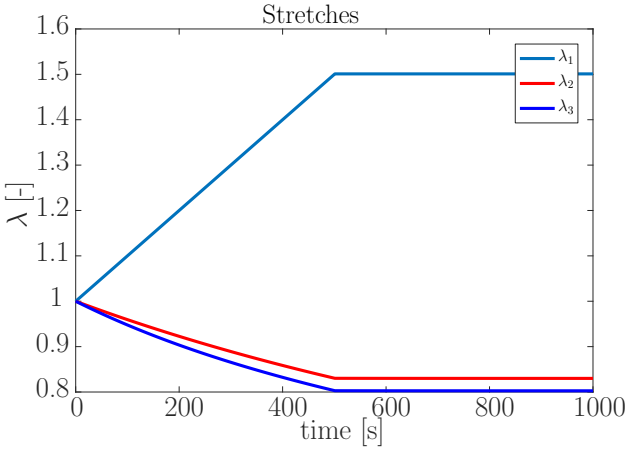

Figure 6.6.: Stretches at 45° preferred direction

6.4. Single Element Tensile Test

To get hold of the anisotropic viscoelastic behaviour in a finite element framework, a single element tensile test is performed in Abaqus. As element type a linear eight node hybrid element C3D8H was used. The material direction was set again to $\boldsymbol{a}_1 = [\frac{\sqrt{2}}{2}, \frac{\sqrt{2}}{2}, 0]$
Due to the unaligned preferred direction with the drive axis the element tends to deform

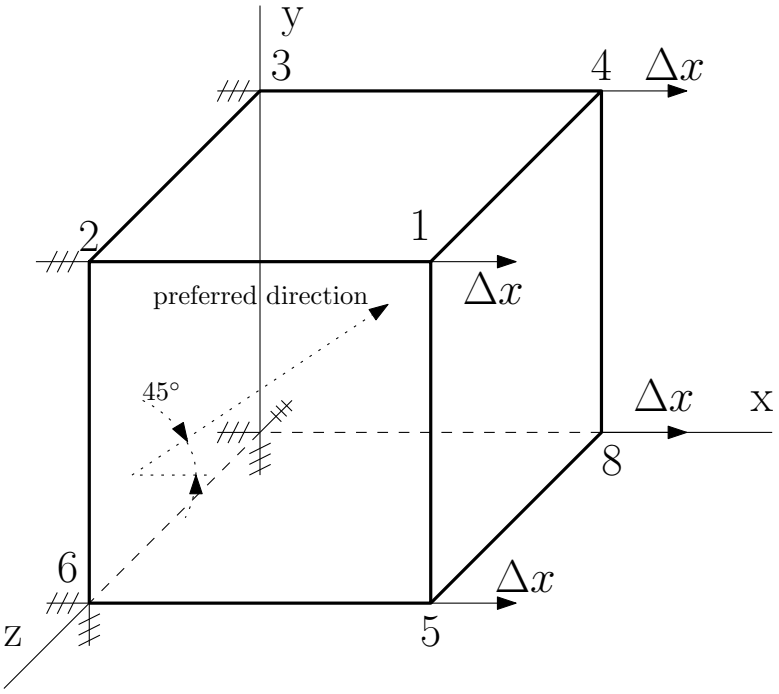

Figure 6.7.: Single element tensile test

$\dot{x}$	$0.01\,\frac{\text{mm}}{\text{s}}$
Edge length	$10\,\text{mm}$
Elongation Δx	$5\,\text{mm}$
total time	$1000\,\text{s}$

Table 6.2.: Single element specification

downwards which aligns the preferred direction with the drive axis. The reason for this is that due to the anisotropic stress part shear stresses are introduced. However, since in this set-up no shear stresses could exist the element has to deform accordingly. The simulation was performed with the parameters in table 6.3.

In figure 6.10, only the Cauchy stress σ_{xx} is plotted since only this stress evolves in the uniaxial stretch test.
In figure 6.9 it is clearly visible that the displacements in y and in z direction are unequal as expected. There is also hardly any relaxation visible in z direction since the anisotropic viscoelastic part is dominating. In contrast to the z direction the displacement in y direction is after the prescription at t=$500\,\text{s}$ slowly decreasing. This behaviour can be explained by taking into account that the back stresses are only at a deformation present.

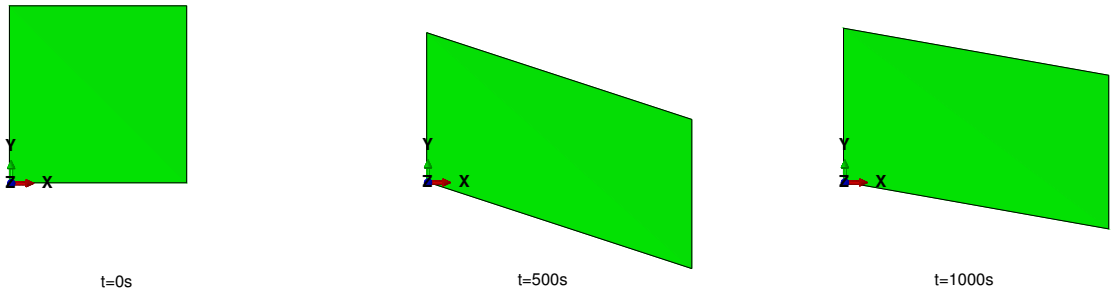

Figure 6.8.: Deformation of the brick element

Isotropic	κ	μ_{10}	μ_{20}	μ_{30}	
	10	2.947×10^{-4}	-3.01×10^{-5}	5.605×10^{-6}	
		Viscosity (i)	τ_i	β_i	
		1	100.0	0.5	
		2	10.0	0.7	
Anisotropic	α_{e1}	α_{e2}			
	0.01	0.02			
		Viscosity (j)	$\tau_{a_1,j}$	$\alpha_{v1,j}$	$\alpha_{v2,j}$
		1	10	1.11	0.0
		2	10	1.11	0.0

Table 6.3.: Input parameters for brick tensile test

Therefore, the whole model is in an over-stress state if the maximum displacement is reached. Because of the permanent elastic part now the relaxation is triggered. Hence, not only the relaxation times are influencing the relaxation behaviour but also the elastic part.
Quantitatively the best displacement to relaxation behaviour of the test discussed in this section can be achieved if elastic stress and over-stresses are of the same order. Since the magnitude of the over-stresses is also dependent on the relaxation time it is not sufficient to compare only the α and β values to get a hold of the over-stress magnitude. Furthermore, also the strain rate has to be considered.
The relaxation behaviour of two Maxwell elements could influence each other, so that it is even possible that the y-displacement could increase due to non-linear effects after the loading (uneven relaxation of the shear stresses). This effect could be observed especially if the parameter $\alpha_{v2,j}$ is unequal to zero. However, the magnitude of this effect is in general small.

6.5. Conclusion

As it was seen in the previous sections, if a desired relaxation displacement is wanted, all the viscous parameters have to be considered since they are affecting each other, so that a clear quantitative effect of one parameter cannot be proposed. Nevertheless, the following influences can be kept in mind.

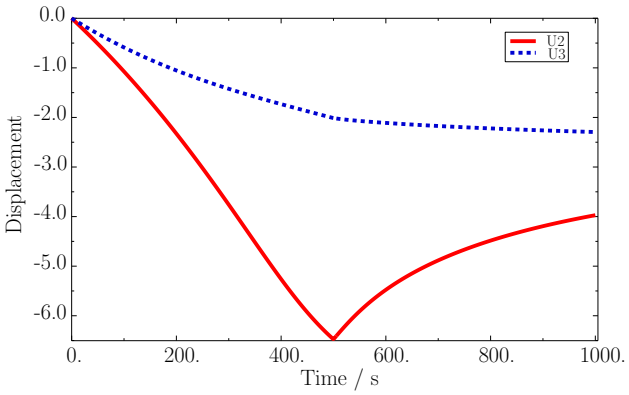

Figure 6.9.: Displacement of $u_y = u_1$ and $u_z = u_3$ of node 1

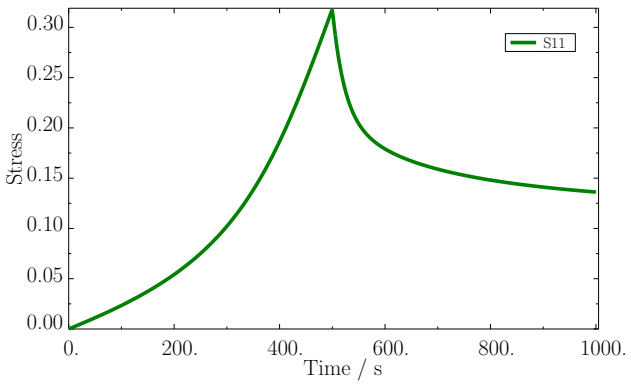

Figure 6.10.: Cauchy stress σ_{xx}

- μ_{10} is dominating at small deformation, hence μ_{20} and μ_{30} can be neglected.
- τ is influencing how big and how fast the back stresses decrease/increase.
- The shear moduli ratios β_i are quantifying the isotropic viscoelastic stress contribution. It is important to consider that if $\beta_i > 1$ the material will slowly relax since the back driving elastic stress (or spring) is small compared to the high counteracting viscous back-stresses.
- The ratio of α_{ei} and α_{vi} have a similar effect as β_i.
- $\alpha_{v1}, \alpha_{v3}, \alpha_{e1}, \alpha_{e3}$ have only a contribution in the preferred direction.
- $\alpha_{v2}, \alpha_{v4}, \alpha_{e2}, \alpha_{e4}$ are hard to classify in their effect. They could be seen as parameters that describe the interaction between preferred direction and isotropic base material. For fibre reinforced material they are expected to be small in value.
- For the sake of completeness κ should be larger or equal to $1 \times 10^4 \mu$ to enforce an accurate incompressibility.

7. Inverse Problem

In the previous chapters the material model and the necessary parameters were described. To estimate the viscosity relaxation experiments are used. For more details see [20]. However, one simple experiment of these is an experiment where a load is prescribed and then held at a constant value while the displacement is measured. As the material model is very complex, it is not possible to directly evaluate material parameters out of a displacement measurement. For that reason the experiment has to be simulated and both experimental and simulation displacements have to by matched varying the material parameters. Such a problem is also known as an inverse problem since with such a procedure the input of the system is found by a given output. This procedure is visualised in figure 7.1.

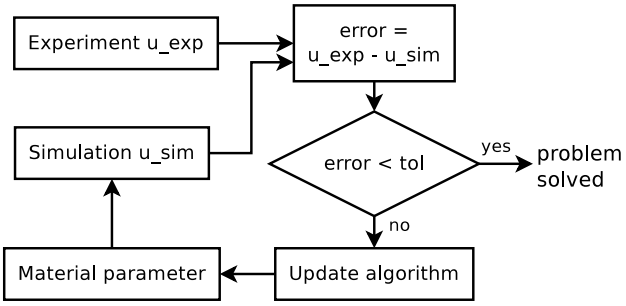

Figure 7.1.: Inverse problem

7.1. Non-linear Least Squares Algorithm

In this section, a short introduction to least squares problems is given since data fitting is solved with such algorithms. A fundamental discussion on this topic can be found in [22] and [26]. In general a least squares problem could be denoted as:

$$F(\boldsymbol{x}) = \frac{1}{2}\boldsymbol{f}(\boldsymbol{x})^T\boldsymbol{f}(\boldsymbol{x}) \tag{7.1}$$

Remark 23. In data fitting problems $f_i(\boldsymbol{x})$ is the error between simulation and experiment at specific time points t_i with the parameters $\boldsymbol{x}$.

$$f_i(\boldsymbol{x}) = \delta_{exp}(\boldsymbol{x})|_i - \delta_{sim}(\boldsymbol{x})|_i \tag{7.2}$$

As $F(\boldsymbol{x})$ represents an error norm, the problem turns into a minimisation problem. For linear problems a wide range of fast algorithms (e.g. SIMPLEX) exist that are often designed for large equation systems. In this thesis, however, a small equation system and a non-linear problem must be solved which means the algorithm performance is of low importance.

7.2. Powell's Dog Leg Algorithm

Every evaluation of the current error with a finite element simulation is very expensive so reducing the evaluation to a minimum is recommended. Especially the evaluation of the Jacobian matrix proves exceedingly costly since the Jacobian has to be approximated iteratively. In the reference [22], independently from the computational cost, it is suggested to use a secant-version approach at problems where the Jacobian has to be approximated. Since the Dog Leg method gives good control over the step size, this algorithm was preferred over the Levenberg Marquardt method.
The Dog Leg algorithm combines the steepest descent direction and the Gauss-Newton step and controls the step width with the trusted region radius Δ.
The error function 7.2 is a non-linear function. To estimate a step size the error function has to be linearised with a Taylor expansion.

$$\boldsymbol{f}(\boldsymbol{x}+\boldsymbol{h}) = \boldsymbol{f}(\boldsymbol{x}) + \boldsymbol{J}(\boldsymbol{x})\boldsymbol{h} \tag{7.3}$$

Where $\boldsymbol{J}(\boldsymbol{x})$ denotes the Jacobian matrix. That has to be approximated iteratively. Introducing this in the function 7.1 leads to the linearised model $L(\boldsymbol{h})$.

$$F(\boldsymbol{x}+\boldsymbol{h}) \approx L(\boldsymbol{h}) = F(\boldsymbol{x}) + \boldsymbol{h}^T\boldsymbol{J}^T\boldsymbol{f} + \frac{1}{2}\boldsymbol{h}^T\boldsymbol{J}^T\boldsymbol{J}\boldsymbol{h} \tag{7.4}$$

To find the minimum of L the first derivation of L' has to be zero. As a result, we get the well-known Newton method.

$$L' = \boldsymbol{J}^T\boldsymbol{f} + \boldsymbol{J}^T\boldsymbol{J}\boldsymbol{h} = 0 \tag{7.5}$$

$$\boldsymbol{J}^T\boldsymbol{J}\boldsymbol{h} = -\boldsymbol{J}^T\boldsymbol{f} \tag{7.6}$$

If equation 7.5 is compared to the general Newton method 7.8., the term $\boldsymbol{J}^T\boldsymbol{J}$ could be identified as the Hessian matrix $\boldsymbol{H}$ and the term $\boldsymbol{J}^T\boldsymbol{f}$ as the gradient $\boldsymbol{g}$.

Remark 24. To find the minimum of the cost function $F(\boldsymbol{x})$ the condition $F'(\boldsymbol{x}^*) = 0$ has to be fulfilled. Since this is a non-linear expression this has to be solved iteratively with the Newton method.

$$F'(\boldsymbol{x}+h) \approx F'(\boldsymbol{x}) + F''(\boldsymbol{x})\boldsymbol{h} = 0 \tag{7.7}$$

$$\boldsymbol{H}\boldsymbol{h} = -F'(\boldsymbol{x}) \tag{7.8}$$

Out of equation 7.6 the Newton step $\boldsymbol{h}_{gn}$ can be evaluated. The steepest descent direction $\boldsymbol{h}_{sd}$ is the gradient.

$$\boldsymbol{h}_{sd} = -F'(\boldsymbol{x}) = -\boldsymbol{g} \tag{7.9}$$

$$\tag{7.10}$$

With that at hand the Dog Leg step $\boldsymbol{h}_{dl}$ could be evaluated (see figure 7.2). So in contrast to damped methods the step norm is clearly limited by the trusted radius Δ. To enable a fast convergence this trusted radius has to be controlled which is achieved by checking if the linearised model L is a good prediction or not. Hence, if the gain ratio ρ (eq. 7.11) has a big value the prediction was good and the radius could be increased.

$$\rho = \frac{F(\boldsymbol{x}) - F(\boldsymbol{x}+\boldsymbol{h})}{L(\boldsymbol{0}) - L(\boldsymbol{h})} \tag{7.11}$$

Which leads to the updating strategy:

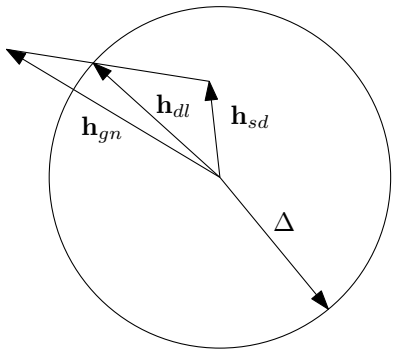

Figure 7.2.: Trusted region: Step definition of Dog Leg algorithm

```
        if rho < 0.25
                Delta = Delta/2
        elseif rho > 0.75
                Delta = max(Delta, 3*norm(h,2))
```

7.3. Secant Version

As stated before, the evaluation of the Jacobian matrix is quite expensive. Due to this, the secant method 7.12 was used. A secant can be used to approximate a finite difference scheme. This is visualised in figure 7.3.
The Jacobian can be updated with the Broyden's rank one update 7.13. Additionally, if one step entry h_i is smaller than 0.8 of its norm $||\boldsymbol{h}||$ an extra differential step is calculated to update one column in the Jacobian with the finite difference scheme to ensure that the approximation of the Jacobian does not get too poor. In conclusion every iteration the vector function $\boldsymbol{f}$ has to be evaluated at maximum twice.

$$\boldsymbol{f}(\boldsymbol{x}) = \boldsymbol{f}(\boldsymbol{x}_{new}) + \boldsymbol{J}_{new}(\boldsymbol{x} - \boldsymbol{x}_{new}) \tag{7.12}$$

$$\boldsymbol{J}_{new} = \boldsymbol{J} + \frac{1}{\|\boldsymbol{h}\|^2}\left[\boldsymbol{f}(\boldsymbol{x}_{new}) - \boldsymbol{f}(\boldsymbol{x}) - \boldsymbol{B}(\boldsymbol{x}_{new} - \boldsymbol{x})\right](\boldsymbol{x}_{new} - \boldsymbol{x})^T \tag{7.13}$$

7.4. Initial Conditions

Even though the step norm $\|h_{dl}\|$ is limited especially at full parameter optimisation it is possible that parameters get negative. Even though some of the parameters could be negative (for example μ_{20}) some other clearly must be positive. For instance the finite element mesh could then collapse because of low or negative stiffness parameters or a negative time constant could lead to extremely high values which would make a convergence impossible. It was found that implementing a constraint with a penalty or barrier function is not effective and is hindering a fast convergence. For that reason, the initial conditions and the specification of the trusted radius have to be chosen carefully. For values that are expected to be close to zero it is advisable to start with an initial value of zero.

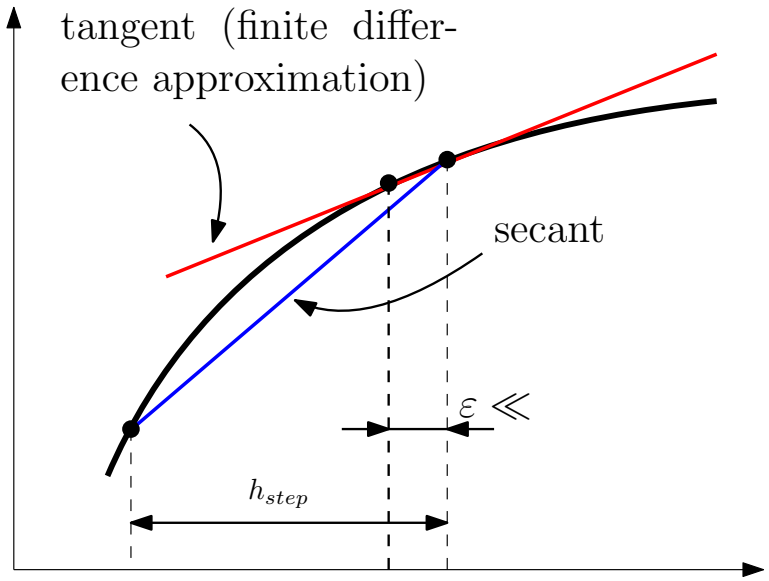

Figure 7.3.: Secant approximation

By combining the Levenberg Marquardt method with the Dog Leg method it is possible to ensure that the parameters are always greater than zero. In this hybrid method the calculated Dog Leg step is checked if it leads to negative parameters. If this applies a step with the Levenberg Marquardt method is calculated while the damping is adjusted so that the step is small enough. Since a large Dog Leg step is an indication for the Jacobian to be inaccurate also the Jacobian is recalculated with a forward Euler discretisation and the trusted radius is reduced. With that at hand it can be ensured that the parameters are definitely positive. However, as mentioned before computational efficiency is lost.

Remark 25. The Levenberg Marquardt method is a damped method. In these methods large steps are penalized by a damping parameter μ. If μ is zero the step is equivalent to the Newton step.

$$min_{\boldsymbol{h}} \left\{ L(\boldsymbol{h}) + \frac{1}{2}\mu ||\boldsymbol{h}||^2 \right\} \tag{7.14}$$

8. Atomic Force Microscopy

This chapter is intended to give a short introduction about atomic force microscopy (AFM). It should help the reader to get a better understanding of the simulation set-up. Therefore, only a little part of the AFM capabilities is discussed. Interested readers about AFM are referred to [13].

In figure 8.1 an exaggerated visualisation of the indentation with the AFM method is displayed. Basically the movement u is prescribed and the deflection d is measured by a laser. Due to the known stiffness k of the cantilever, also a force can be prescribed and the movement u has to be controlled respectively. The indentation δ is the difference of movement u and deflection d. Due to the small dimension adhesion forces and magnetic interaction are as well influencing the measurements. However, the measurement on the pulp fibres are in such a way designed that the adhesion force can be neglected. In the experiment the force is prescribed very fast and hold constant over a specific time (see also figure 9.5).

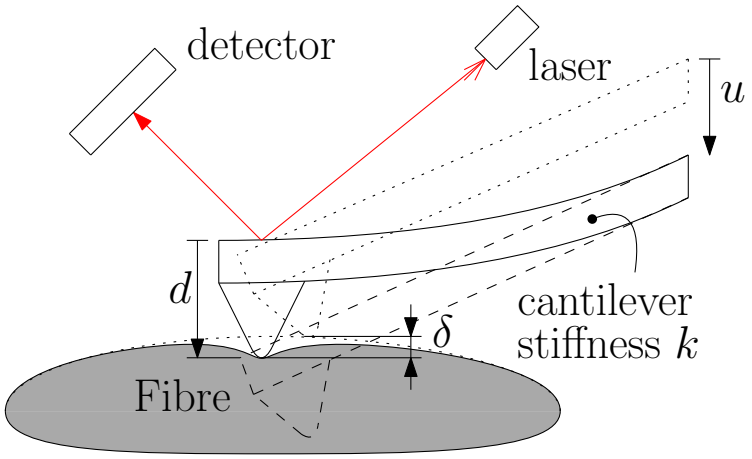

Figure 8.1.: Atomic force microscopy

Currently the measurement set-up on pulp fibres is in development. For a first test of the experiment set-up indentation experiments on poly-methyl-methacrylate (PMMA) are performed. This data was during the master thesis available and used for the development of the material parameter estimation algorithm. The indentation data of pulp fibres is qualitatively similar.

9. Inverse Problem with Hertz Theory

In this master thesis the focus lies on the analysis of nano indentation experiments. There is no analytical description of an indentation with a complex material model as it is used in this thesis. However, it is for investigation purposes interesting to estimate the material parameters with the analytical Hertz theory and compare results.
In chapter 6 and 4.9.1, it was investigated that some simplification regarding the parameters can be made.
Firstly, in the isotropic elastic contribution, only the parameter μ_{10} has to be considered for moderate stretches $\lambda < 2$. Therefore, the isotropic contribution is equivalent to the Neo-Hookean model. For the parameters of the Neo-Hookean model a relation to the Lamé constants is present, so that these parameters can be directly compared to the parameters of the small strain theory.
Secondly, a further simplification occurs out of the fact that the indentation experiments give no indication to distinguish between an anisotropic effect and isotropic effect, thus only the isotropic parameters can be estimated.
With these simplifications, the difference of small strain theory and finite strain theory is only given if large deformations are present. As in the indentation experiment about 10% strains are expected, it justifies the usage of finite strain theory. But it is also expected that the difference to the small strain theory is not that large. Consequently, this also justifies the usage of the small strain theory, on which the Hertz theory is based on.

9.1. Viscoelastic Hertz Contact Model

From [19] a simple method is known to implement viscoelasticity into the Hertz theory. For an incompressible material with the Poisson's ratio $\nu = 0.5$ the stress simplifies to equation 9.1. See also section 10.1 for more details about the reduced Young's modulus and plane stress.

$$\boldsymbol{\sigma} = 4\mu\boldsymbol{\varepsilon} \tag{9.1}$$

For the generalised Maxwell model, the stress strain relation can be expressed in the frequency domain as:

$$\sigma(s) = G(s)\varepsilon(s) \tag{9.2}$$

If equation 9.2 is compared to equation 9.1 then it becomes clear that 4μ must be substituted by the transfer function to integrate the viscosity in the model. This step makes perfect sense in a demonstrative way since the viscosity changes the stiffness

over time.

$$a^3 = (R\delta)^{\frac{3}{2}} = \frac{3}{4}\left(\frac{1}{4\mu}\right) RP \tag{9.3}$$

$$\rightarrow a(s)^3 = \frac{3R}{4}\left(\frac{1}{G(s)}\right) P(s) \tag{9.4}$$

$$\delta(s) = \left[\frac{3}{4\sqrt{R}}\left(\frac{1}{G(s)}\right) P(s)\right]^{\frac{2}{3}} \tag{9.5}$$

Where P is the indentation force, R the indenter radius, a the radius of the contact area and δ the indentation. For more details see section 10.2. A detailed discussion on this topic can be found in [19]. Evaluating now the transfer function $G(s)$ of a generalised Maxwell element with a similar method as it is known from resistor networks (node rule and loop rule; see also [8]):

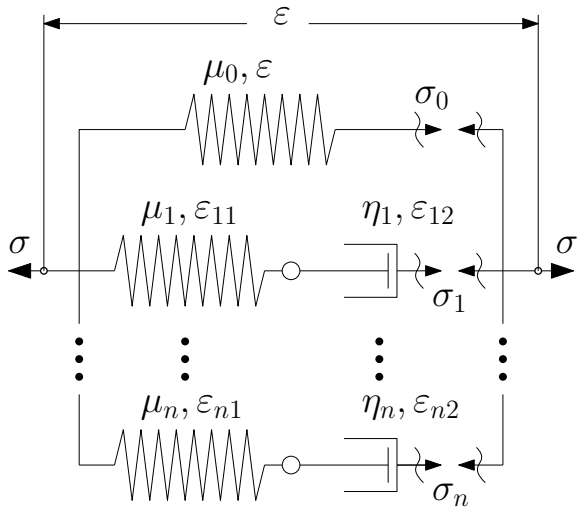

Figure 9.1.: Generalized Maxwell element

$$\sigma_0 + \sigma_1 + \sigma_2 = \sigma \quad \text{node rule} \tag{9.6}$$

$$\varepsilon_{11} + \varepsilon_{12} - \varepsilon_{22} - \varepsilon_{21} = 0 \quad \text{loop rule} \tag{9.7}$$

$$\varepsilon_{21} + \varepsilon_{22} - \varepsilon = 0 \quad \text{loop rule} \tag{9.8}$$

Introducing the stress strain relation $\sigma = \mu\varepsilon$ and taking the equilibrium in the branches into account $\sigma_i = \sigma_{i1} = \sigma_{i2}, \varepsilon = \varepsilon_{i1} + \varepsilon_{i2}$.

$$\sigma = \mu_0\varepsilon + \eta_1\dot{\varepsilon}_{12} + \eta_2\dot{\varepsilon}_{22} \tag{9.9}$$

$$\mu_1\varepsilon_{11} = \eta_1\dot{\varepsilon}_{12} \rightarrow \mu_1(\varepsilon - \varepsilon_{12}) = \eta_1\dot{\varepsilon}_{12} \tag{9.10}$$

$$\mu_2\varepsilon_{21} = \eta_2\dot{\varepsilon}_{22} \rightarrow \mu_1(\varepsilon - \varepsilon_{22}) = \eta_2\dot{\varepsilon}_{22} \tag{9.11}$$

Performing a Laplace transformation leads to

$$\sigma = \mu_0\varepsilon + \eta_1 s\varepsilon_{12} + \eta_2 s\varepsilon_{22} \tag{9.12}$$

$$\varepsilon_{12} = \frac{\mu_1\varepsilon}{\mu_1 + \eta_1 s} \tag{9.13}$$

$$\varepsilon_{22} = \frac{\mu_2\varepsilon}{\mu_1 + \eta_2 s} \tag{9.14}$$

$$\sigma = \mu_0\varepsilon + \eta_1 s\frac{\mu_1\varepsilon}{\mu_1 + \eta_1 s} + \eta_2 s\frac{\mu_2\varepsilon}{\mu_1 + \eta_2 s} \tag{9.15}$$

By introducing the relaxation time $\tau_i = \frac{\eta_i}{\mu_i}$ and the shear moduli ratio $\beta_i = \mu_i\mu_0$ the transfer function is found.

$$\sigma = \underbrace{\mu_0\left[1 + \beta_1\frac{s}{\frac{1}{\tau_1} + s} + \beta_2\frac{s}{\frac{1}{\tau_2} + s}\right]}_{G(s)}\varepsilon \tag{9.16}$$

From the general form of equation 9.6 follows that for n Maxwell elements the stress σ is defined as:

$$\sigma = \mu_0\left[1 + \sum_{i=1}^{n}\beta_i\frac{s}{\frac{1}{\tau_i} + s}\right] \tag{9.17}$$

For the configuration with only one Maxwell element equation 9.16 can be reorganised to ε. For more than one Maxwell element the result is a long expression which is too complex. This becomes clear if it is imagined that for the strain response the branches influences each other where at the stress response they just add up. Equation 9.18 shows the strain step response in the frequency domain.

$$\varepsilon = \frac{1}{\mu_0}\left[\frac{1}{s} - \frac{1}{s + \frac{1}{\tau_1(1+\beta_1)}} + \frac{\frac{1}{1+\beta_1}}{s + \frac{1}{\tau_1(1+\beta_1)}}\right] \tag{9.18}$$

Finally, transforming back to the time domain by evaluating the step response gives:

$$\varepsilon(t) = \frac{1}{\mu_0}\left[1 - \exp\left(-\frac{t}{\tau_1(1+\beta_1)}\right) + \frac{1}{1+\beta_1}\exp\left(-\frac{t}{\tau_1(1+\beta_1)}\right)\right] \tag{9.19}$$

Remark 26. To compare the shear moduli of the analytical model and that of the hyperelastic model of chapter 4 it has to be considered that for the Neo-Hookean material $\mu_{10} = \frac{\mu}{2}$ and in the analytical description $4\mu = \mu_0$ is replaced. In the hyperelastic formulation, to compare μ_{10} and μ_0, the latter has to be divided by 8.

$$\mu_{10} = \frac{\mu_0}{8} \tag{9.20}$$

9.1.1. Dissipation Energy

From [16] it is known that each Maxwell element is through its relaxation time τ in a specific frequency domain active. Therefore, if due to the experiment it is known that there is a short term and a long term response these Maxwell elements are hardly influencing each other. As a consequence these Maxwell elements can be fitted separately.

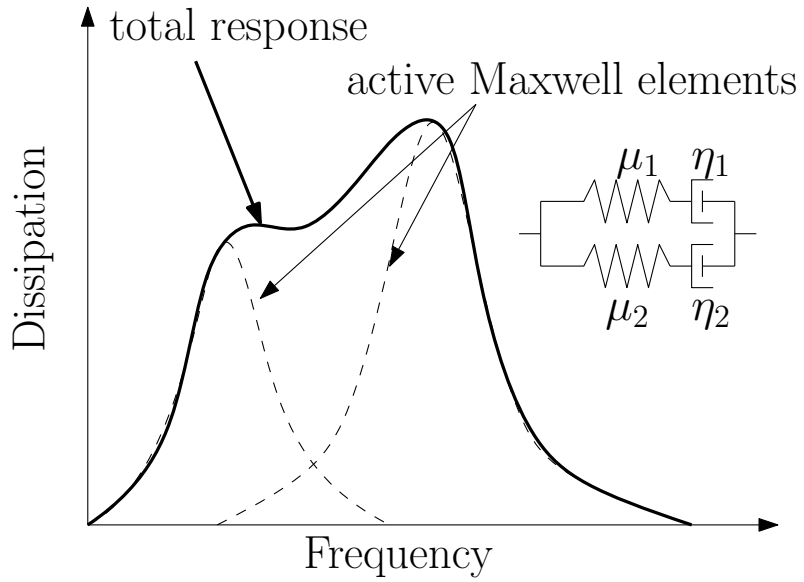

Figure 9.2.: Dissipation energy influence by Maxwell elements

The dissipation energy of one damper W_{Di} can be calculated by integrating the damping force over one period.

$$W_{Di} = \oint F_D \, d\varepsilon_{i2} \tag{9.21}$$

$$W_{Di} = \oint \eta_i \, \dot{\varepsilon}_{i2} \, d\varepsilon_{i2} \tag{9.22}$$

$$W_{Di} = \int_0^{\frac{2\pi}{\omega}} \mu_0 \beta_i \tau_i \, \dot{\varepsilon}_{i2}^2 \, dt \tag{9.23}$$

Considering equation 9.13 and 9.16 the strain rate $\dot{\varepsilon}_{i2}$ can be evaluated. The strain rate can be expressed by the transfer function $T(s)$ with stress input as in equation 9.25.

$$\dot{\varepsilon}_{i2}(s) = \frac{s\mu_i\varepsilon_0}{\mu_i + \eta_i s} = \underbrace{\frac{s}{1+\tau_i s}\frac{1}{G}}_{T(s)} \sigma(s) \tag{9.24}$$

$$\dot{\varepsilon}_{i2}(s) = T(s)\sigma(s) \tag{9.25}$$

Assuming there is only a cosine input signal the steady state output is given by equation 9.27. For more details, see [14] [18]. By introducing this into the dissipation energy 9.23 the integral can be solved.

$$\varphi_i = arc(T_i(j\omega)) \tag{9.26}$$

$$\dot{\varepsilon}_{i2} = |T_i(j\omega)| cos(\omega t + \varphi_i) \tag{9.27}$$

$$W_{Di} = \int_0^{\frac{2\pi}{\omega}} \mu_0 \beta_i \tau_i (|T_i(j\omega)|^2 \cos(\omega t + \varphi_i))^2 dt \tag{9.28}$$

$$W_{Di} = \mu_0 \beta_i \tau_i |T_i(j\omega)|^2 \int_0^{\frac{2\pi}{\omega}} (\cos(\omega t + \varphi_i))^2 dt \tag{9.29}$$

$$W_{Di} = \mu_0 \beta_i \tau_i |T_i(j\omega)|^2 \frac{\pi}{\omega} \tag{9.30}$$

To get the total dissipation those parts have to be summed up for the n Maxwell elements.

$$W_D = \sum_{i=1}^{n} W_{Di} \tag{9.31}$$

9.1.2. Influence of the Relaxation Time on Dissipation Energy

The dissipation energy would be a better quantity for the calibration of the relaxation times τ_i and shear moduli ratios β_i. Since no experimental values for the dissipation energy is available it is investigated how much a poor estimation of the relaxation times could affect the dissipation energy. In this investigation it is assumed that a perfect fit $var1$ resembles the true dissipation energy. Then the relaxation times are varied and it is observed how much it influences the dissipation energy distribution.

As it can be imagined that a curve fit with only one Maxwell element dedicated for the short time response would result in bad and meaningless curve fit this applies also if a certain Maxwell element in between a frequency domain is skipped for the short time response. This is visualised in variation $var3$ where unreasonable high dissipation magnitudes are calculated. Out of the variations $var5$ and $var6$ follows that for the short term part the relaxation time has to be higher than $3s$ to prevent this 'gap'. The result of $var4$ is that the long term part should be below $40s$ to get a good and reasonable fit otherwise the peak in figure 9.3 would further decrease. The lower boundary of the long term relaxation time is implicitly defined through the duration of the experiment. Considering that the long term part should be active until the end. A similar limitation holds for the upper boundary of the short term part to establish a decoupling of long and short term part. More details on estimating these parameters is discussed in section 9.3.

In conclusion, the more Maxwell elements over a frequency range are used the less important it gets which values the relaxation times have.

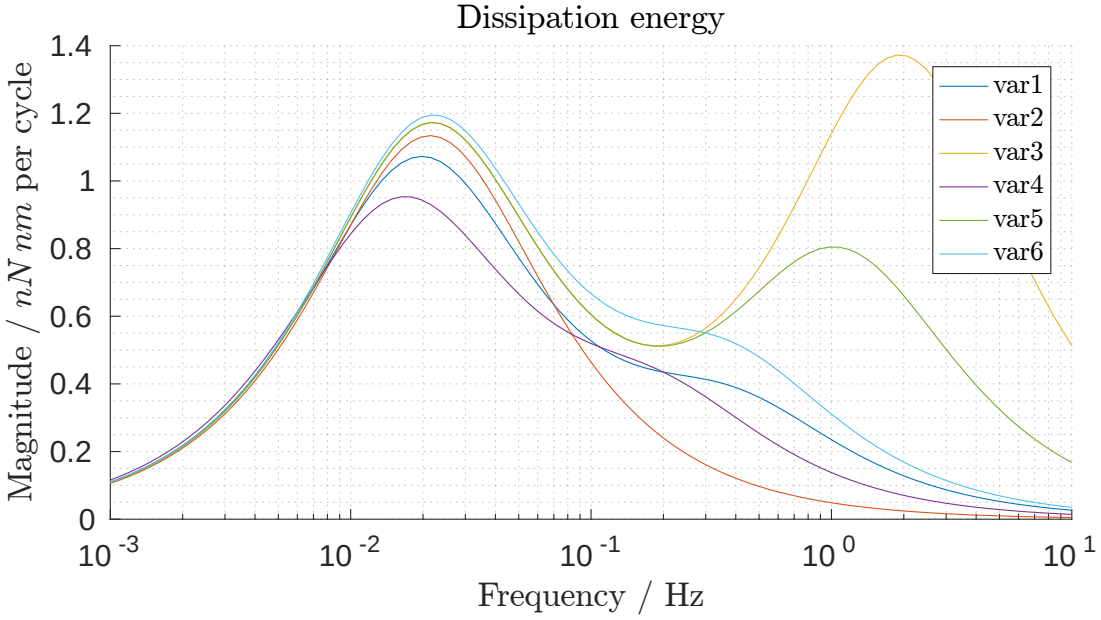

Figure 9.3.: Influence of relaxation times on dissipation energy

	$var1$	$var2$	$var3$	$var4$	$var5$	$var6$
τ_1	40	35	35	50	35	35
τ_2	3	-	0.1	3	0.5	2
τ_3	1	-	-	-	-	-

Table 9.1.: Variation parameter

9.1.3. Step Response

As discussed in section 9.1.1 the Maxwell elements are active in different frequency domains depending on the relaxation time τ_i. Consequently, they are also decoupled in their contribution to the system response.
In the indentation experiments, the load is prescribed in a short time so that it is as a first step convenient to look at step responses of the model. In figure 9.4, the decoupling of the long and the short term behaviour is clearly visible. However, at this point it should be noted that even though these parts are decoupled for the fit of the short time response it is required that the long term response was already fitted. Otherwise, no useful results can be expected. An interesting observation is that the factor $\frac{1}{1+\beta}$ can be

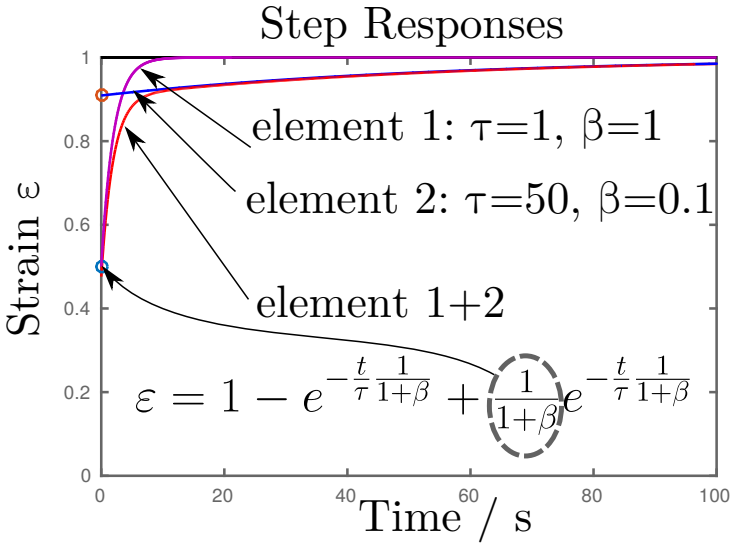

Figure 9.4.: Step response

directly extracted from the signal at $t = 0$ (see figure 9.4).

9.1.4. Experiment Load Response

If the indentation experiment is looked at, the force is loaded with a ramp as shown in figure 9.5 Since this is a linear model, the solution of a ramp response $P(s) = \frac{k_{load}}{s^2}$ can be superimposed to give a respective total response. Where k_{load} is the load rate and u

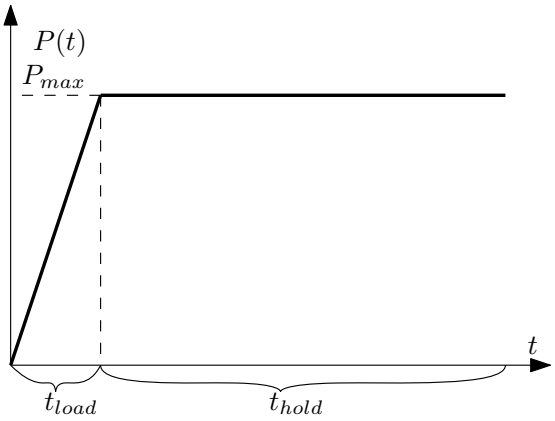

Figure 9.5.: Load

the unit step function (Heaviside function).

$$P(t) = k_{load}t - k_{load}(t - t_{load})u(t - t_{load}) \tag{9.32}$$

$$u(t) = \begin{cases} 0 & t < 0 \\ 1 & t \geq 0 \end{cases} \tag{9.33}$$

By doing so, the indentation response can be found with ramp response δ_{ramp} of equation 9.5.

$$\delta(t) = \delta_{ramp}(t) - u(t - t_{load})\delta_{ramp}(t - t_{load}) \tag{9.34}$$

9.2. Indenter Radius Correction

In the experiment the indentation is performed in a pan in the surface. This curvature is considered by correcting the radius R with equation 9.36. Equation 9.36 represents the relative curvature. For more details, see [19]. The background of the contact hole curvature and its estimation can be looked at in [6].

$$R_{hole} = \frac{\delta_{pl}^2 + r_{hole}^2}{2\delta_{pl}} \tag{9.35}$$

$$R = \left(R_{indenter}^{-1} - R_{hole}^{-1}\right)^{-1} \tag{9.36}$$

9.3. Fitting Strategy

During the solution of the inverse problem, a poor fitting performance was observed if all parameters were attempted to fit at the same time. This can be explained by the following factors.

- The elastic parameters μ_i influence the viscoelastic response.

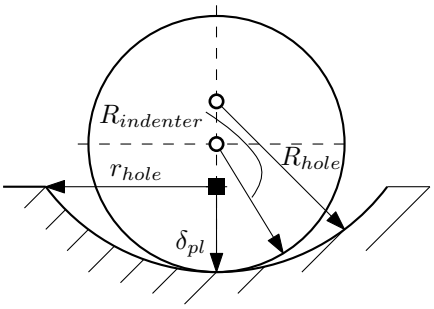

Figure 9.6.: Relative curvature

- Through the initial conditions it has to be defined which Maxwell element branch should represent which effect, otherwise a jumping phenomenon could appear.
- If the Maxwell elements are in a close frequency domain active they influence each other.
- The parameters have different magnitudes which could lead to ill-conditioned Jacobian.
- There are more combinations of τ_i and β_i to establish equivalent good curve fit.

To circumvent these problems it is on one hand good to separate the fitting process in sub processes and on the other hand to fixate on specific relaxation times. For a first estimation of useful relaxation times, the general behaviour of similar exponential functions as they appear in the constitutive laws is considered.
As it is known for exponential expressions like equation 9.37 after $t = 3\tau$ the function value drops approximately to 5%.

$$u = \exp(-\frac{t}{\tau}) \tag{9.37}$$

In section 9.1, it was already mentioned that there is a short-term and a long-term response. To estimate the relaxation times of short term and long term the experimental indentation curve 9.7 can be divided into two time-domains.

$$\tau_{short\,term} = \frac{t_{short\,term}}{3} \approx 3s \tag{9.38}$$

$$\tau_{long\,term} = \frac{t_{long\,term}}{3} \approx 40s \tag{9.39}$$

As has become clear from section 9.1.2, that if fewer Maxwell elements are used the values of the relaxation times have to be estimated precisely. Hence, it is necessary to also fit the relaxation times. While for the analytical model the computational time is not significantly increased, for the simulation with the finite element model it has a tremendous effect. Therefore, it is convenient to estimate the relaxation times with the analytical model and fit only the shear moduli ratios β_i. Another advantage regarding the computational time arises from the fact that for the short-term effect only the first part of the simulation has to be evaluated which is further reducing the computational time. As mentioned before, the fitting process is performed by fitting the elastic and the viscoelastic parameters separately. Such a procedure is also known from [16]. To receive an even more accurate fitting as well the short-term and the long-term Maxwell elements are fitted in different sub processes.

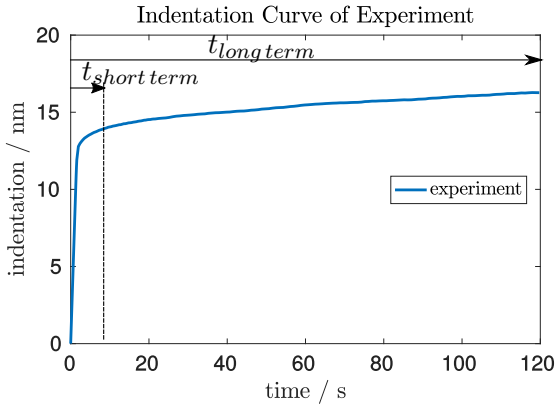

Figure 9.7.: Indentation measurement

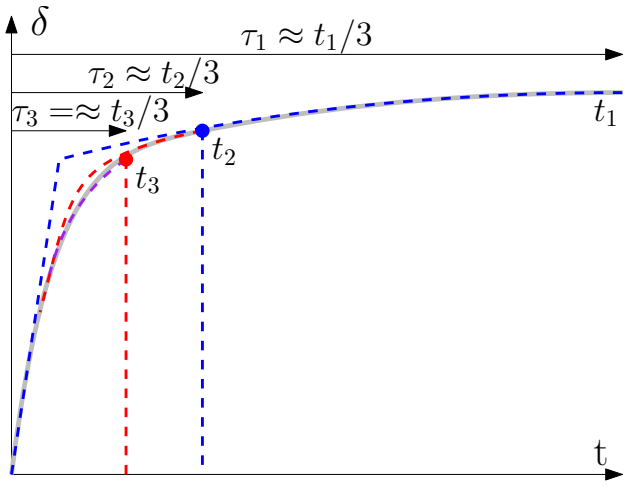

Figure 9.8.: Successive estimation of relaxation times

1. Fit the curve to the last part of the target curve. By assuming that all relaxation processes have finished this part resembles the elastic part.
2. Fit the curve to the intermediate part of the target curve which resembles the long-term part.
3. Fit the curve to the first part of the target curve which resembles the short-term part.

9.4. Curve Fit with Hertz Model

This fitting strategy was tested with the analytical model of section 9.1. Here, a second Maxwell element was used for the short-term response. From figure 9.9 to figure 9.12, the four stages of the fitting process are shown (In the fourth stage a second short term Maxwell element was fitted). To be able to compare the parameter to the hyperelastic model of chapter 4, μ_0 is recomputed to μ_{10} (see remark 26).

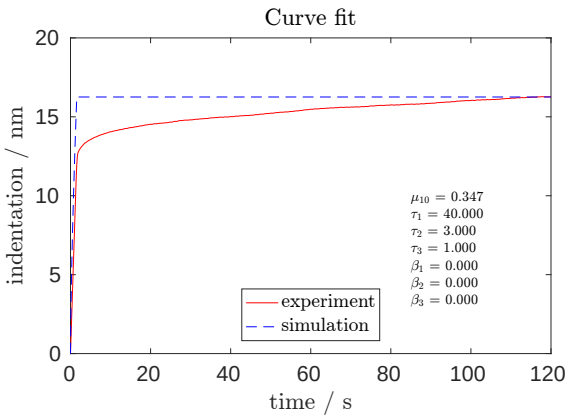

Figure 9.9.: Elastic parameter fit

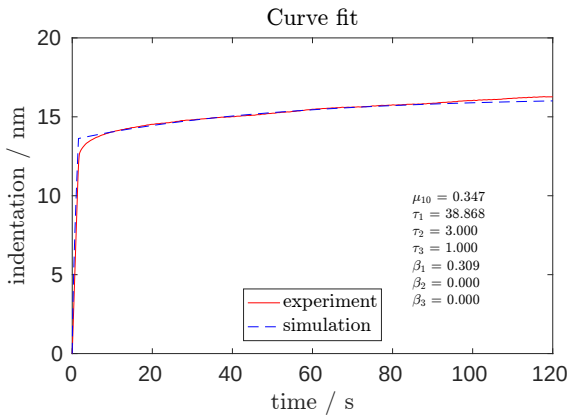

Figure 9.10.: Long term fit

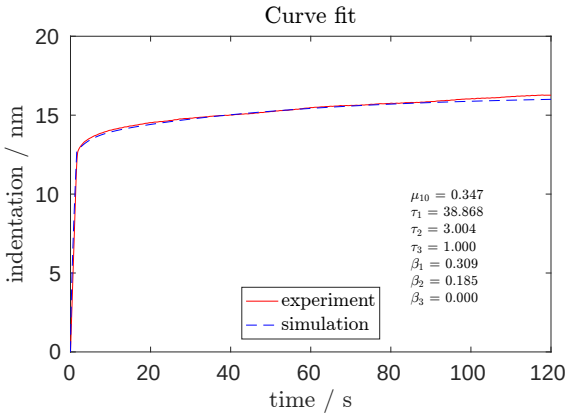

Figure 9.11.: Short term fit 1

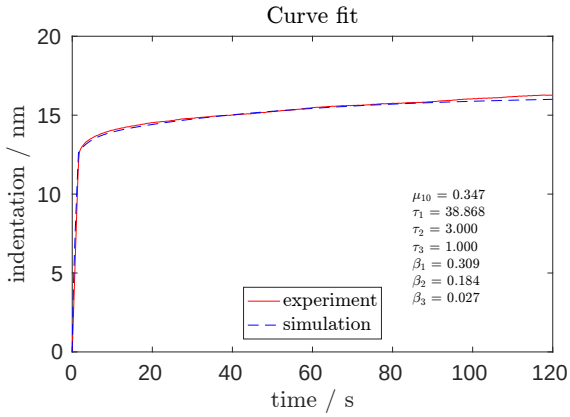

Figure 9.12.: Short term fit 2

In the dissipation energy distribution 9.13 clearly one peak can be seen representing the long-term response or the first Maxwell element. Right to the peak at higher frequency a slight bump is visible that is showing the contribution of the short-term part. The duration of the experiment is limiting the frequency band which can be pictured. For this sample curve there is an indication that a Maxwell-element even for a lower frequency is needed. This indication can be seen if it is looked closely to the end of the curve fit which shows a deviation. This problem cannot be solved by just adding another low frequency Maxwell-element because actually the reason for this discrepancy can be tracked back to the assumption that the last part is representing the converged elastic part. It is also most likely that the single loading is not sufficient to capture high frequencies. So, in conclusion the experiment is not suitable to represent all frequencies.

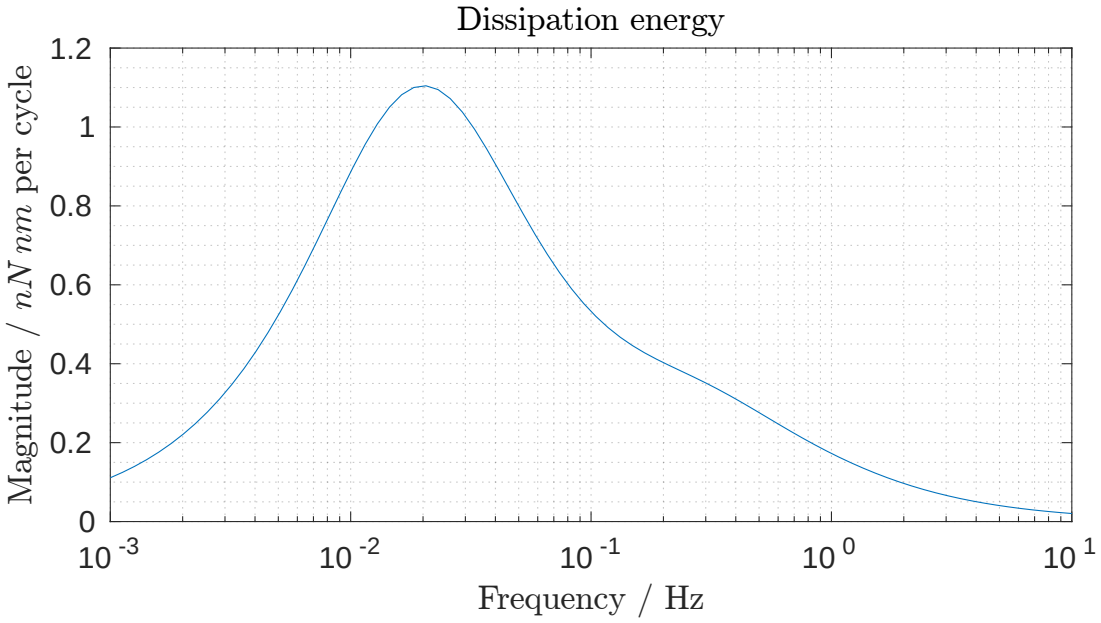

Figure 9.13.: Dissipation energy of Hertz theory curve fit

10. Inverse Problem with SOOFEA

In chapter 6 it was found that only μ_{10} is relevant for the elastic contribution and since PMMA is isotropic only the isotropic viscoelastic parameter τ_i and β_i were taken into account.

10.1. Testing on a Brick Element

For a fundamental study if the material model is capable of showing a similar behaviour as it is observed in the experiments it is the best approach to test the material on a simplified geometry. Since the quadratic convergence of the implementation was already tested on a brick element, it was decided to find a way to simulate the indentation experiment on this brick element. After this testing phase, the material model can be implemented into Abaqus to get full access to element libraries, contact algorithms, post processing and many other tools.

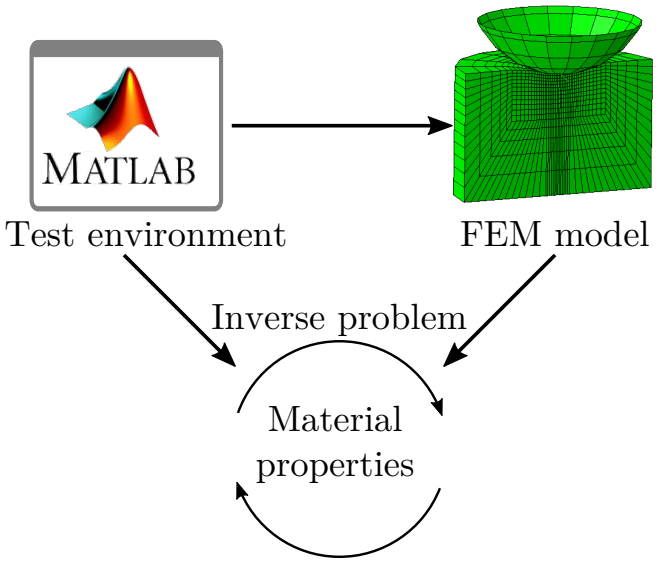

Figure 10.1.: Testing phase of material parameter estimation

The basic idea is to convert the indentation experiment into a compression of a brick element. The Hertz theory is used in order to find a representative geometry for the brick.

The Hertz theory proposes a solution for a two dimensional stress distribution as visualised in figure 10.2. By converting this solution into a one-dimensional rod tensile (compression) test a respective cross-sectional area and length (height) can be evaluated which can be used for the brick geometry as shown in figure 10.3.

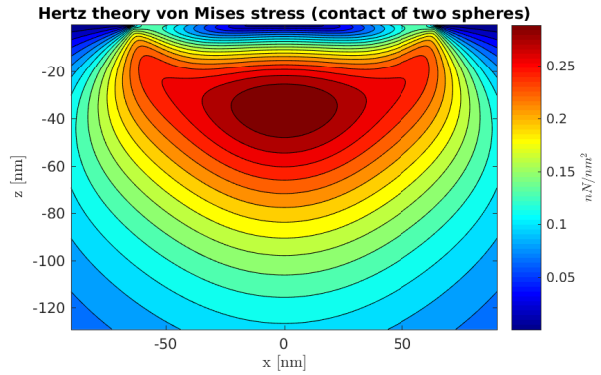

Figure 10.2.: Two dimensional stresses

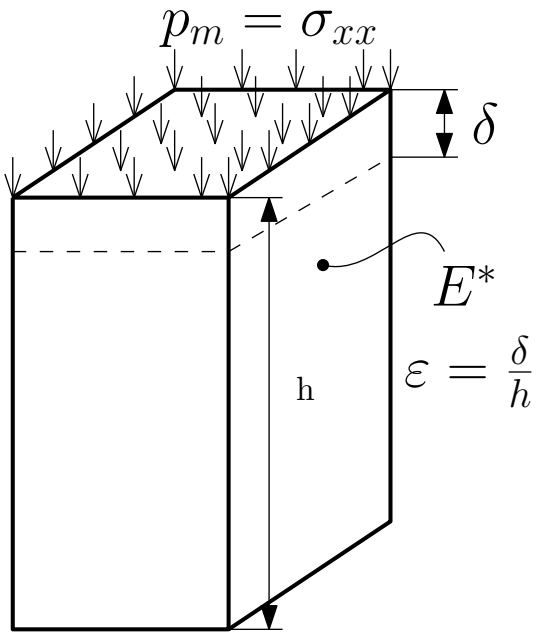

Figure 10.3.: One dimensional rod

10.2. Defining the Geometry of the Brick Element

From the experiments the maximum indentation δ and the contact radius R of the indenter are known. The radius R was evaluated as mentioned in section 9.2. The Hertz theory proposes an elliptical pressure distribution in the contact area between indenter and specimen. The following equations were taken from [19] and for more information on that topic it is also referred to this reference.

$$p(r,t) = p_0 \left(1 - \left(\frac{r}{a}^2\right)\right)^{1/2} \tag{10.1}$$

The middle pressure of this distribution is

$$p_m = \frac{2}{3} p_0 \tag{10.2}$$

The maximum pressure p_0 can be expressed by the Force P

$$P = p_m \pi a^2 \tag{10.3}$$

For a circular point contact with the load P Hertz proposes a contact radius a and indentation δ.

$$a = \left(\frac{3PR}{4E^*}\right)^{1/3} \tag{10.4}$$

$$a^2 = R\delta \tag{10.5}$$

Where E^* is the representative elastic modulus for plane stress.

$$\boldsymbol{\sigma} = \boldsymbol{C}\boldsymbol{\varepsilon} \tag{10.6}$$

$$\boldsymbol{C} = \underbrace{\frac{E}{1-\nu^2}}_{E^*} \begin{pmatrix} 1 & \nu & 0 \\ \nu & 1 & 0 \\ 0 & 0 & \frac{1-\nu}{2} \end{pmatrix} \tag{10.7}$$

$$\begin{pmatrix} \sigma_{xx} \\ \sigma_{yy} \\ \tau_{xy} \end{pmatrix} = \frac{E}{1-\nu^2} \begin{pmatrix} 1 & \nu & 0 \\ \nu & 1 & 0 \\ 0 & 0 & \frac{1-\nu}{2} \end{pmatrix} \begin{pmatrix} \varepsilon_{xx} \\ \varepsilon_{yy} \\ \varepsilon_{xy} \end{pmatrix} \tag{10.8}$$

Which gives for a uni-axial stretch $\varepsilon_{yy} = 0$, $\varepsilon_{xy} = 0$

$$\sigma_{xx} = E^* \varepsilon_{xx} \tag{10.9}$$

For an incompressible material $\nu = 0.5$ the equation could be further simplified. It is also convenient to substitute the elastic modulus E by the shear modulus μ.

$$\mu = \frac{E}{2(1+\nu)} = \frac{E}{3} \tag{10.10}$$

$$E^* = 4\mu \tag{10.11}$$

$$a^3 = \frac{3}{8}\left(\frac{1}{2\mu}\right) RP \tag{10.12}$$

With the definition of the strain 10.13 and evaluating the shear modulus out of equation 10.4 the height h is defined by equation 10.17. The width or edge length b of the quadratic bottom can be evaluated out of the contact radius given by 10.5.

$$\varepsilon_{xx} = \frac{\delta}{h} \tag{10.13}$$

$$\sigma_{xx} = E^* \varepsilon_{xx} = p_m = \frac{P}{\pi R \delta} \tag{10.14}$$

$$\sigma_{xx} = 4\mu \frac{\delta}{h} \tag{10.15}$$

$$\mu = \frac{3}{16} \frac{P}{\sqrt{R}\delta^{\frac{3}{2}}} \tag{10.16}$$

$$h = \frac{4\mu\delta}{\sigma_{xx}} \tag{10.17}$$

$$b = \sqrt{a^2\pi} \tag{10.18}$$

δ	...	indentation
a	...	contact area radius
R	...	radius of tip
E	...	elastic modulus
μ	...	shear modulus
P	...	indenting force

10.3. Simulation in SOOFEA

The simulation was performed in an adapted version of an object oriented finite element program SOOFEA [12] performed. The Matlab source code was provided by the Institute of Strength of Materials. Due to the nearly incompressibility of the material it was necessary to use a 27 node brick element to prevent locking effects. The basic set-up is shown in figure 10.5. The geometry of the brick was evaluated with the estimates of section 10.2.

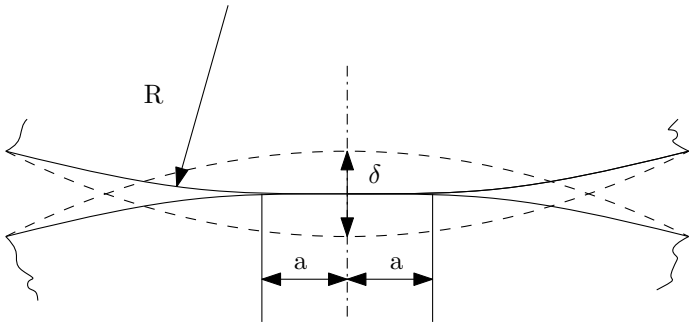

Figure 10.4.: Contact of two spheres

R	$350\,\mathrm{nm}$
δ	$16.28\,\mathrm{nm}$
δ_{pl}	$10\,\mathrm{nm}$
r_{hole}	$200\,\mathrm{nm}$
P	$5000\,\mathrm{nN}$
h	$195.8\,\mathrm{nm}$
b	$147.3\,\mathrm{nm}$

Table 10.1.: Brick geometry

The magnitudes of the nine nodal forces were calculated to represent an energy consistent evenly distributed pressure load. For that, the pressure has to be integrated over the surface. The results of this integration in the initial configuration is given in table 10.2. An update of the distribution during the analysis was not considered since the change could be neglected.

corner nodes	$\frac{1}{36}$
edge middle nodes	$\frac{1}{9}$
center node	$\frac{4}{9}$

Table 10.2.: Nodal forces

Figure 10.6 shows the solution of the brick simulation. In this simulation the relaxation times where chosen accordingly to the results of section 9.4 $\tau_1 = 40s$, $\tau_2 = 3s$, $\tau_3 = 1s$. The bulk modulus κ was set to 100.

10.4. Conclusion

In this analysis a lower stiffness was evaluated as in the Hertz theory. To analyse this result the same brick element was simulated in Abaqus with a Yeoh material. It was found out that on one hand the usage of a hybrid element and on the other hand, the usage of a finer discretisation than one element have a significant influence on the indentation result. Which means that the result is dependent on the "mesh" and the 27 node element is behaving too stiff due to the incompressibility.
However, it was not the aim of this analysis to evaluate quantitatively exact results but to investigate if the material model is capable to fit the experimental indentation curve and

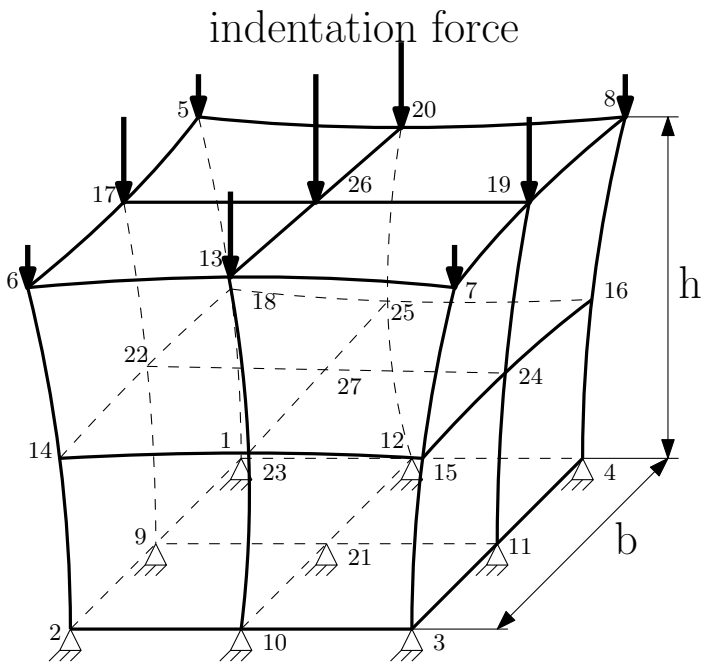

Figure 10.5.: 27 node hexahedron

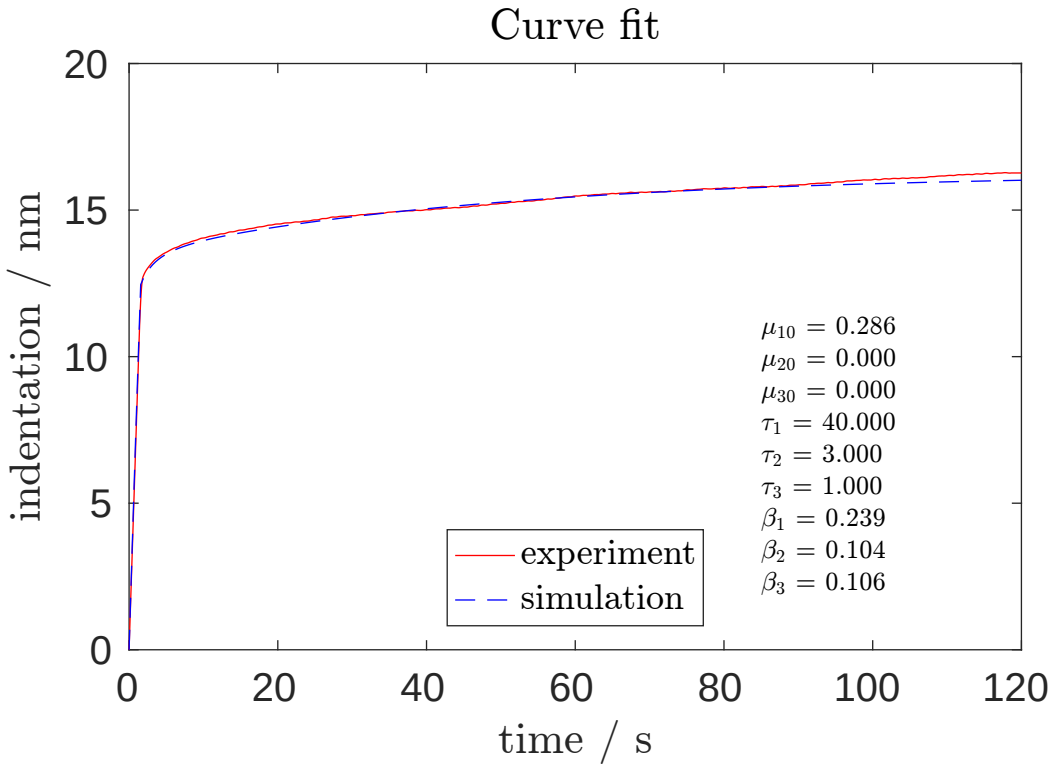

Figure 10.6.: Indentation solution of brick simulation

if the magnitudes of the parameters are plausible. With that in mind as it can be seen in figure 10.6 that the curve could be fitted well it is a promising outcome of this analysis.

11. Inverse Problem with Abaqus Solver

For the simulation with Abaqus the experiment has to be modelled. Afterwards, a communication between the inverse problem solver in Matlab and Abaqus has to be established. During the thesis the tool InvPro was designed to establish this communication. In figure 11.1, the flow diagram of the simulation is visualised. At first, the experimental data has to be averaged appropriately. Then, with the non-linear least squares algorithm implemented in the tool InvPro a new parameter combination is estimated and an input file for Abaqus is generated. In Abaqus, the indentation experiment is then simulated with the specified material parameters. The result of this simulation is compared to the experimental curve and if the difference is small enough, the curve fitting was successful and the right material parameters were found.

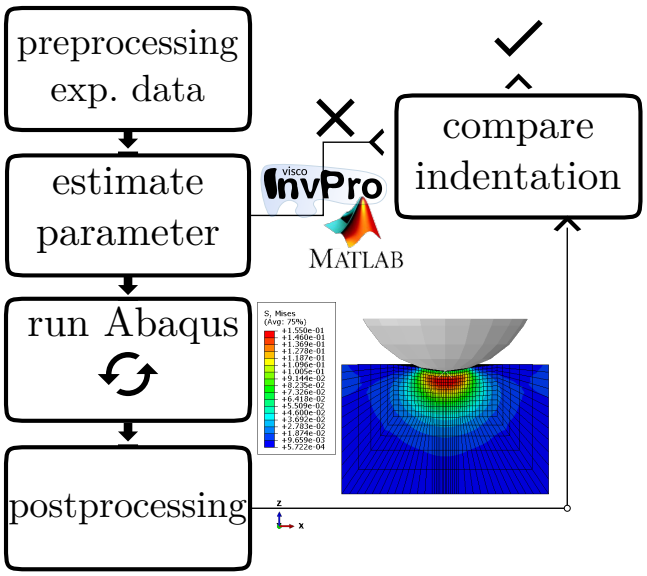

Figure 11.1.: Communication between the different programs

11.1. Mesh

The mesh generation is based on the source code of the software tool STABiX [24]. The mesh is generated with a python script, consists only of brick elements and is structured. In the indentation experiment a contact hole is formed before the measurement starts. For that reason, the existing script had to be adapted at some parts. For a more detailed discussion why this contact hole is necessary, refer to [6].
Due to the incompressible material and the fact that the indentation experiment is performed on a small fibre, it was decided to only fixate the bottom nodes of the mesh. Otherwise, if the outer diameter nodes would also be locked, the material would behave

much stiffer than appropriate due to its incompressibility. There are several mesh refinement control variables which are defined in table 11.1.

Input parameter:		
r_{hole}	= 200	Depends on experiment
δ_{pl}	= 10	Depends on experiment
r_{sample}	= 400.0	
h_{sample}	= 500.0	
$R_{indenter}$	= 350.0	
Proportions:		
box_zfrac	= 0.4	partition vertically = $\frac{z_{top}}{h_{sample}}$
r_center_frac	= 0.25	radial partition of center and core = $\frac{r_{core}}{r_{center}}$
Number of entities		
box_bias_x		Bias in x direction
box_bias_conv_x		Bias in x direction for the outer cylinder
box_bias_z		Bias in z direction
box_elm_nx		Number of horizontal elements in box
box_elm_nz		Number of vertical elements in box
radial_divi		Number of horizontal elements between the big sample and the box
c_divi		$r_{core} = r_{center}/c\_divi$
c_outer_divi		Number of elements for outer core sample in the radial direction
sample_rep		Number of sample sectors (have to be divisible by 8)

Table 11.1.: Mesh properties

11.2. Indenter and Contact Specification

For the indenter an analytical rigid sphere surface was used. This approach is justified by the fact that the indentation depth is small and the indenter has a big radius on its tip, so that a full consideration of the indenter geometry is not necessary (see figure 11.3). Even so, the topology of the indenter surface would have an effect on the results, it cannot be considered since this data is not available. The indenter was set as rigid as PMMA is much softer then the indenter.
The contact was assumed frictionless since no reliable data for the friction coefficient was available and a finite slide surface to surface contact algorithm was used.
The pressure-overclosure method was set to "Hard"-contact and the constraint enforcement method was set to the default penalty method to establish fast convergence.
The contact initialisation leads often to convergence problems so that in the contact initialisation phase $t_{contact}$ the no-overclosure constraint was eased. For that reason, the initialisation was modelled as a separate step so that there would also be the option (if unexpected convergence problems appear) to initialise the contact with a displacement controlled approach or adapt the solver controls accordingly.

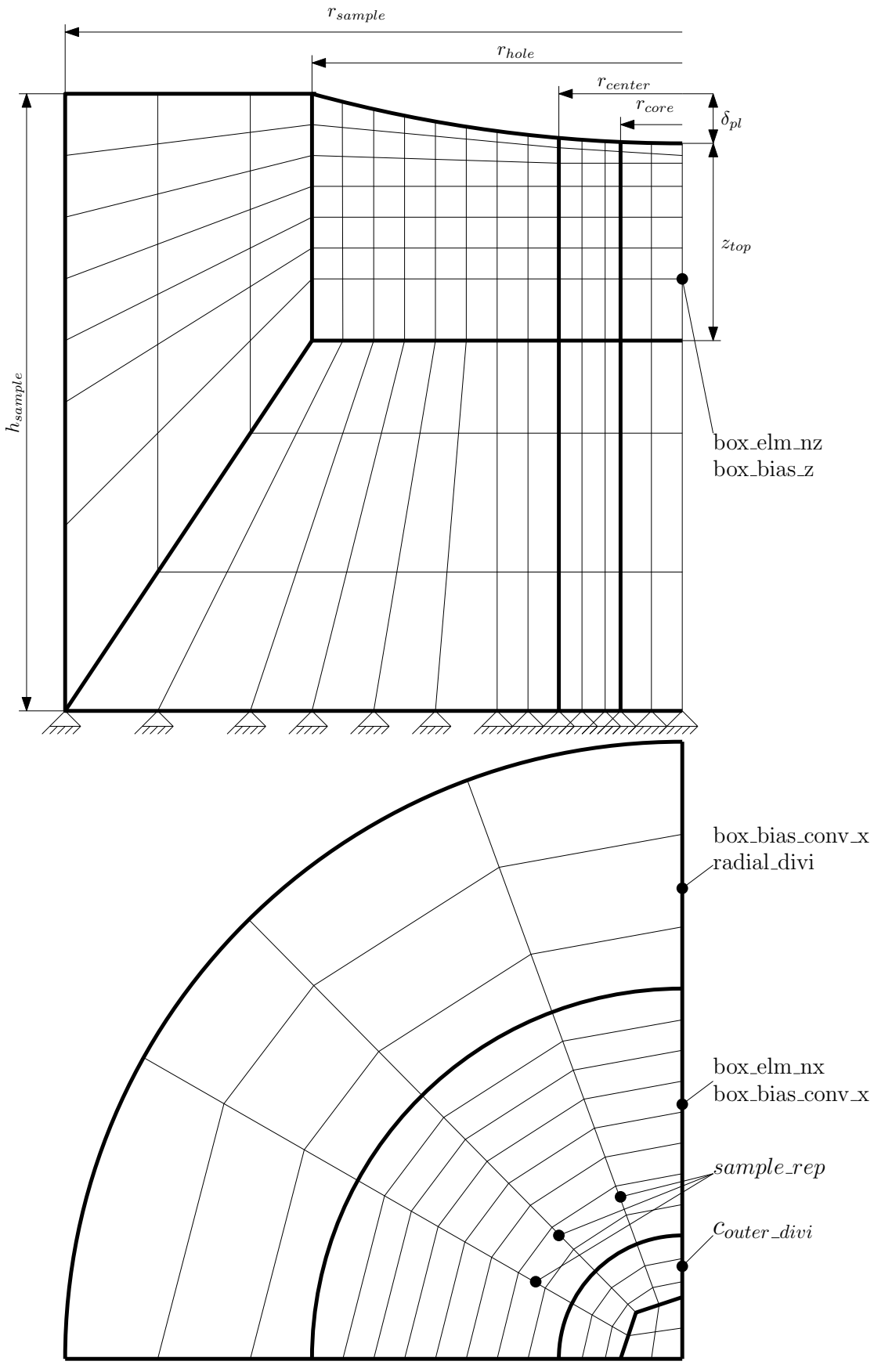

Figure 11.2.: Mesh properties

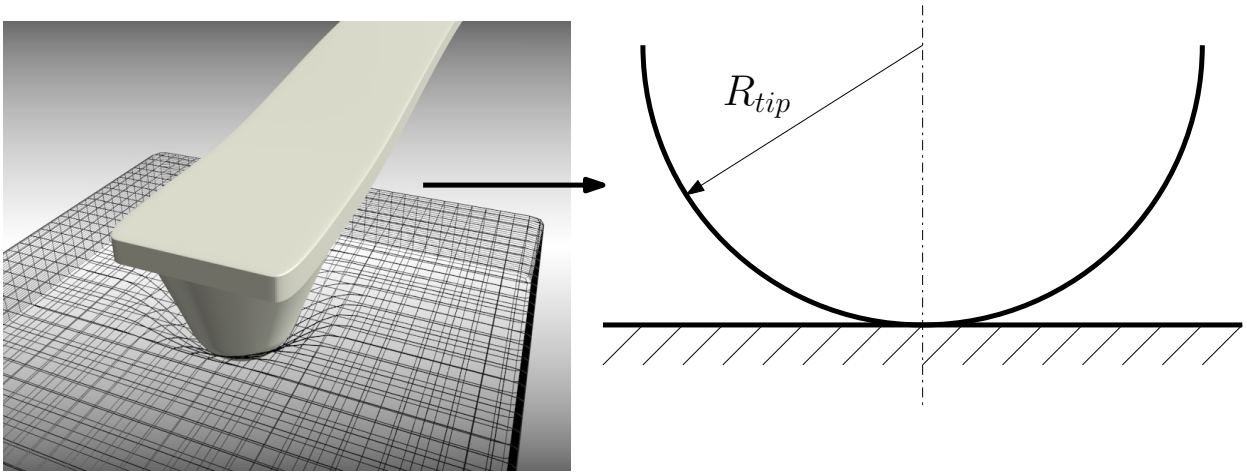

Figure 11.3.: Indenter

11.3. Mesh Study

In a mesh study the mesh is successively refined. If the stresses and the indentation do not change with the element number or mesh refinement anymore, the consequence is that the results are not dependent on the mesh size, which is wanted. The mesh study was performed with a fully incompressible hyperlastic Yeoh material to establish fast convergence.

#	box _bias_x	box_bias _conv_x	box _bias_z	box_elm _nx	box_elm _nz	radial _divi	c_divi	c_outer _divi	sample _rep
1	3	3	3	7	4	3	2	2	16
2	3	3	3	9	5	4	2	3	16
3	3	3	3	12	6	6	3	4	16
4	3	3	3	16	7	7	4	6	24
5	3	3	3	18	10	8	4	8	24
6	3	3	3	18	14	8	4	8	24
7	3	3	3	20	16	5	5	10	24
8	3	3	3	20	20	7	5	10	24
9	3	3	3	16	12	6	4	6	24
10	3	3	3	16	14	6	4	6	24
11	3	3	3	16	14	6	4	7	24
12	3	3	3	15	15	6	4	7	24
13	3	3	2	15	15	6	4	7	24
14	3	3	2	20	24	7	5	10	24

Table 11.2.: Mesh study properties

As a result of the mesh study the configuration 12 showed the same indentation and stress results compared to a fine mesh. Therefore, this configuration was chosen.

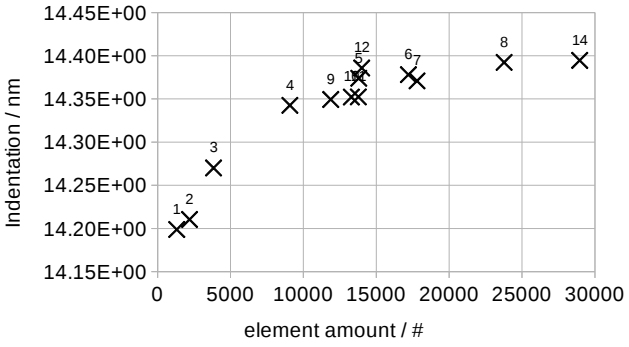

Figure 11.4.: Indentation result of mesh study

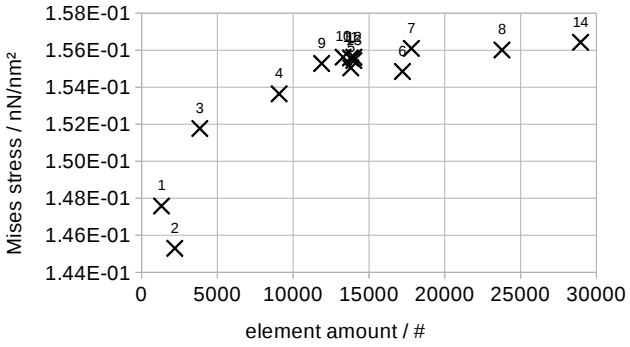

Figure 11.5.: Stress result of mesh study

11.4. Simulation

Similar to chapter 10.3 again three Maxwell elements were used and the fitting process was divided into four sub-processes. The bulk modulus and the loading was specified as in table 11.3. For the load specification see also figure 9.5. The element type was set to a hybrid element C3D8RH with reduced integration and enhanced hourglass control.

P_{max}	$5000\,\mathrm{nN}$
t_{load}	$1.56\,\mathrm{s}$
t_{hold}	$120\,\mathrm{s}$

Table 11.3.: Input specification

In contrast to the SOOFEA simulation in chapter 10.3 here the volumetric locking phenomena was eliminated due to the mixed elements. As expected the shear moduli are higher in value.
By comparing the β values to the Hertz theory results a little difference is visible. This has more than one reason: Firstly the relaxation times were set to other values. Secondly the algorithm could fit the curve with a different parameter combination, especially the short-term response. Thirdly there are non-linear effects. Those non-linear effects can be shown if the indentation curve is normalized and fitted with a linear generalised Maxwell element model. Comparing the fitting parameters again in figure 11.7 and 11.6 a significant difference is visible. By thinking one step ahead also the dissipation energies could be compared. The dissipation energy can be evaluated by setting both shear moduli to one which gives the distribution 11.8. In conclusion the non-linear effects lead to a vertical distortion of the dissipation energy distribution. However, this once again justifies that the relaxation times can be estimated with such a linear model or the Hertz model of chapter 9.1. On the contrary the β-values have to be calculated.

11.4.1. Stresses

Clearly from figure 11.9 to 11.12 it can be seen how the stresses relax after the loading due to the viscosity.

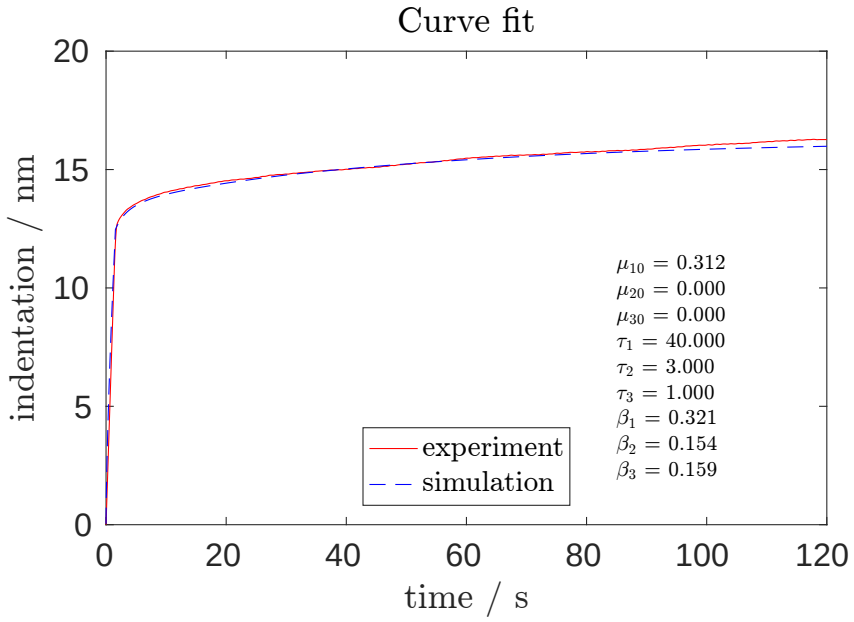

Figure 11.6.: Solution of the curve fit with Abaqus

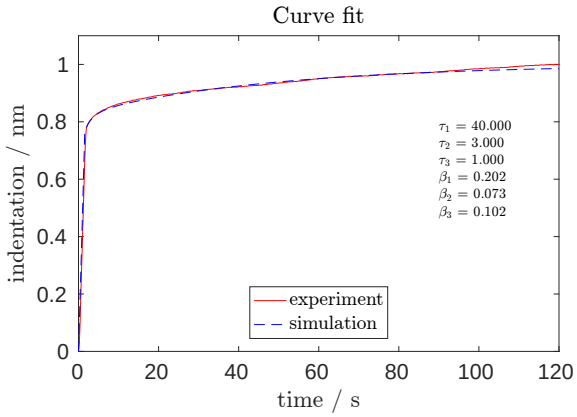

Figure 11.7.: Normalized curve fit

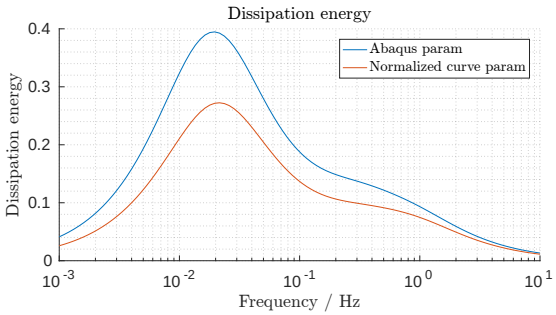

Figure 11.8.: Dissipation energy comparision

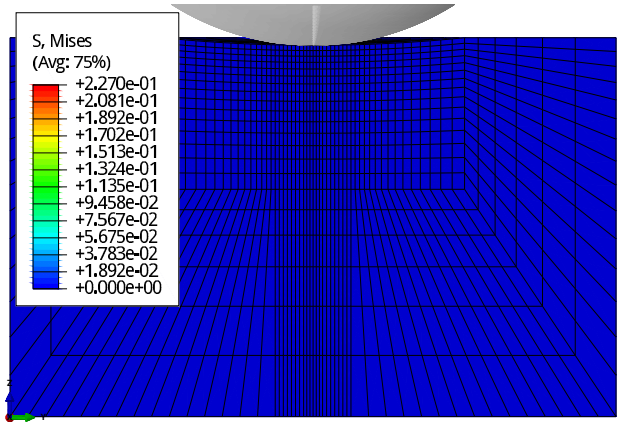

Figure 11.9.: Indentation at 0 s

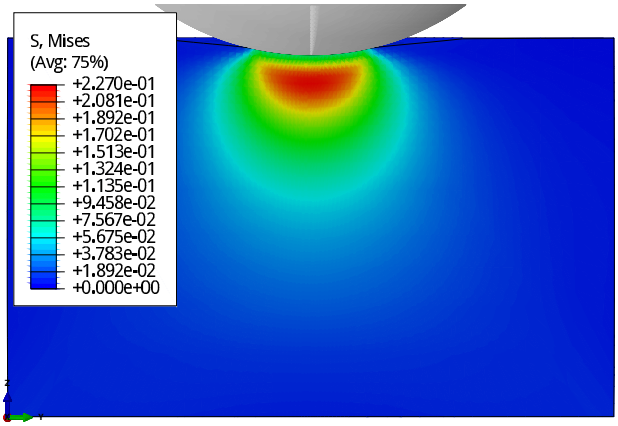

Figure 11.10.: Indentation at 1.56 s

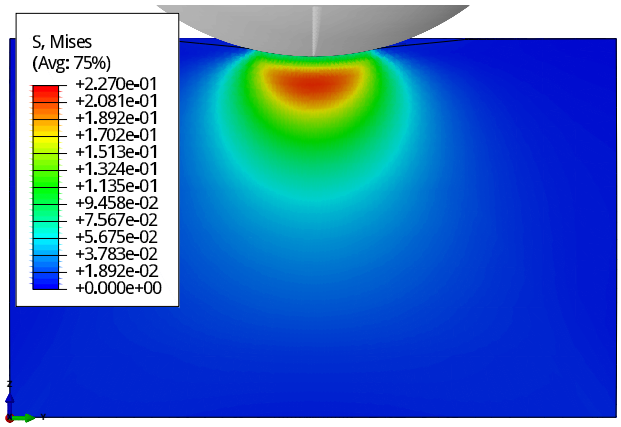

Figure 11.11.: Indentation at 3.16 s

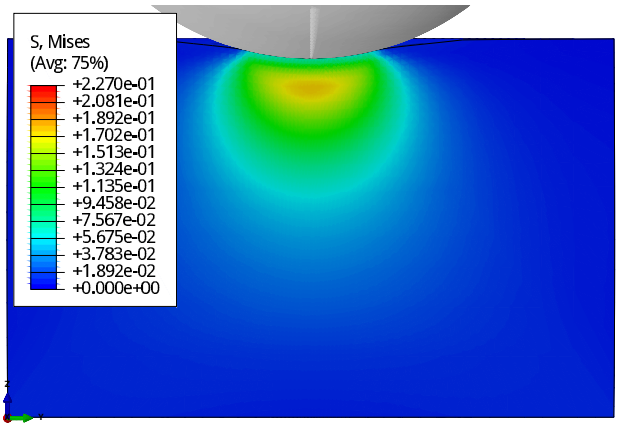

Figure 11.12.: Indentation at 121.56s

11.4.2. Contact Pressure

A further influence of the viscosity is that the contact pressure changes over time due to the viscosity (see figure 11.13). A consequence of the changing contact pressure is that the contact radius a is as well changing over time.
By evaluating the equivalent concentrated force P of the pressure distribution the plausibility of the results can be checked. Assuming an elliptical pressure distribution gives for the time $t = 121.56s$:

$$P = \frac{2}{3} p_{max}\, \pi\, a^2 = \frac{2}{3}\, 0.25\, \pi\, 100^2 \approx 5200 \approx 5000 \checkmark \tag{11.1}$$

During the analysis it was found out that the mesh parameter c_divi has to be chosen accordingly to other mesh parameters. Further details are given in the appendix 4.

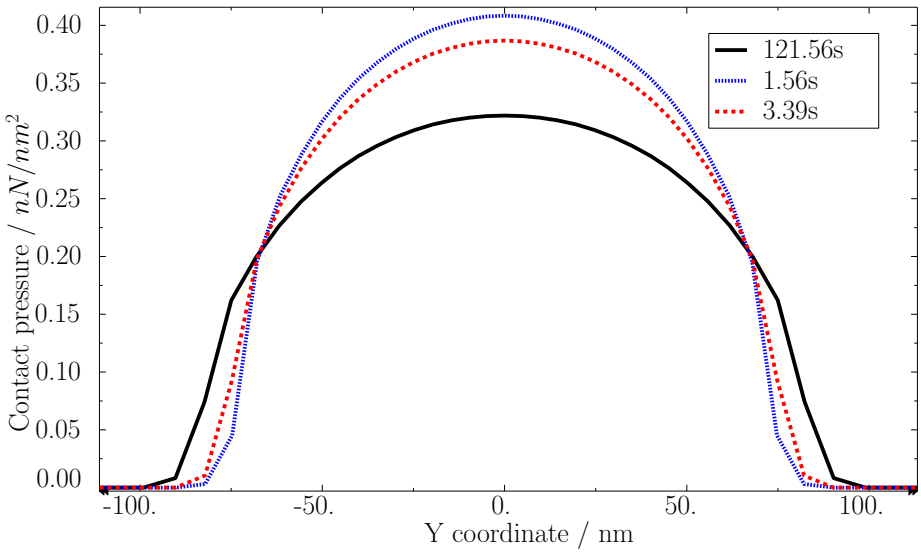

Figure 11.13.: Contact pressure distribution along y-axis

11.5. Conclusion

It was found that little differences of the maximum indentation depth influences the result of the shear moduli significantly. This applies also on the contact geometry or in other words the indenter and the contact hole.

The indentation experiments were performed on a PMMA sample. For the PMMA sample it is known from a tensile test that the elastic modulus is about $2.8\,\mathrm{GPa}$. To compare this with the incompressible material the modulus has to be divided by three to get the shear modulus $\mu = 0.93\,\mathrm{GPa}$ and again by two to obtain the parameter μ_{10}=$0.47\,\mathrm{GPa}$. While comparing this with the results of the simulation a moderate conformity is found. This difference either originates from the uncertainties in either the contact geometry or in the experimental measurements. Furthermore, it is also possible that the assumption of an incompressible material in these small scales is not valid for PMMA. Last but not least it is also possible that the material properties on the surface measured with the indentation experiment are not identical with the inner material properties which would make a comparison to a macro scale tensile test impossible.

The difference of the shear modulus compared to the Hertz theory is not immense but the difference can be explained due to the consideration of large deformations which will increase the contact area and therefore the material must not be as stiff as in the Hertz theory. As the contact radius a is close to the indenter radius it is moreover questionable if the assumptions of the Hertz theory are still valid.

12. Summary and Outlook

The assignment of tasks in this thesis was to implement a suitable material model for pulp fibres in an object oriented finite element code in Matlab and in Abaqus and then use this implementations to calibrate the material model parameters by simulating nano indentation experiments on pulp fibres. For this calibration an inverse problem has to be solved.

For the description of the pulp fibre, a very versatile material model was used with anisotropic and viscoelastic properties. The model is based on the theory of finite deformation and on hyperelastic potentials. For the elastic part the strain energy function proposed by Yeoh [33] was used. Viscoelasticity was implemented after the formulation of Simo [30] and Holzapfel [15]. For the formulation of the anisotropy the elastic potentials proposed by Schroeder and Neff [29] were taken into account. Even though, the material model is capable of anisotropic behaviour, but the available experimental data on PMMA gave no knowledge about any anisotropic parameters, it was decided to only estimate the isotropic parameters and disable the anisotropic contribution.

For a better understanding of the indentation experiments an analytical Hertz model was extended with viscoelasticity. With this model the main influences of viscous effects on the indentation experiment were analysed and a curve fitting strategy has been developed. This fitting strategy was necessary, since during the solution of the inverse problem a poor performance of a full parameter optimisation was observed. In this strategy the fitting process is divided into sub processes and only one parameter is fitted in one process. With that approach on one hand the fit could be controlled better and on the other hand computational time was reduced.

In a test phase of the material model it was investigated if the material model is suitable to reproduce a similar response as in the experiments. This test was performed with a finite element code SOOFEA in Matlab on a simple brick element geometry.

At last the indentation experiments where simulated in Abaqus and the inverse problem iteratively solved. An outcome of this simulation was that due to large deformations different results than the Hertz theory were investigated. Moreover, it was possible to get a good curve fit with two Maxwell elements. This was also an indication that the experiment can only cover a certain frequency band of the dissipation energy distribution.

An outlook of this investigation is that the estimated viscoelastic parameters should be compared to viscoelastic parameters that are evaluated based on dynamic tests to ensure that these results are accurate. A next step will be the analysis of real indentation data of pulp fibres. Since it was found that the contact geometry has a big influence on the analysis, it will be in future analysis beneficial to know the geometry more precisely.
Another investigation will be to adapt the current elastic potentials to get a minimum amount of parameters while the material model behaviour is similar or even better.

Bibliography

[1] ABAQUS. *ABAQUS: Theory Guide*. Dassault Systemes, 2016 (cit. on pp. 16, 47, 92, 93).

[2] Inc. ANSYS. "A large deformation Neo-Hookean user material in ANSYS". In: *ANSYS, Inc 275 Technologoy Drive, Canonsburg, PA 15317* (2008) (cit. on p. 93).

[3] K.J. Bathe and P. Zimmermann. *Finite-Elemente-Methoden*. Springer, 2002. ISBN: 9783540668060. URL: https://books.google.at/books?id=Lypjx7CEIt8C (cit. on p. 14).

[4] Chiara Bellini and Salvatore Federico. "Green-Naghdi rate of the Kirchhoff stress and deformation rate: the elasticity tensor". In: *Zeitschrift fuer angewandte Mathematik und Physik* 66.3 (June 2015), pp. 1143–1163. ISSN: 1420-9039. DOI: 10.1007/s00033-014-0421-x. URL: https://doi.org/10.1007/s00033-014-0421-x (cit. on p. 93).

[5] J. Bonet and R.D. Wood. *Nonlinear Continuum Mechanics for Finite Element Analysis*. Cambridge University Press, 2008. ISBN: 9781139467544. URL: https://books.google.at/books?id=V5Zf1rVeeEsC (cit. on pp. 16, 18).

[6] Ganser C. and Czibula C. "Combining adhesive contact mechanics with a viscoelastic material model to probe local material properties by AFM, submitted to Soft matter". In: - (2017) (cit. on pp. 64, 74).

[7] Zienkiewicz O. C. and Taylor R. L. *Finite Element Method: Volume 2*. 5th edition. McGraw-HILL Book Company (UK) Limited, 2000 (cit. on p. 15).

[8] P.D. Cha, J.J. Rosenberg, and C.L. Dym. *Fundamentals of Modeling and Analyzing Engineering Systems*. Cambridge University Press, 2000. ISBN: 9780521594639. URL: https://books.google.at/books?id=iv92vctq3j4C (cit. on p. 59).

[9] (DaimlerChrysler AG) D. Liefeith S. Kolling. *An Anisotropic Material Model for Finite Rubber Viscoelasticity*. LS-DYNA Anwenderforum, Frankenthal, 2007 (cit. on pp. 2, 17).

[10] Thomas Ebner, Ulrich Hirn, Wolfgang Fischer, Franz Schmied, Robert Schennach, and Manfred Ulz. "A proposed failure mechanism for pulp fiber-fiber joints". In: *Bioresources* 11.4 (Sept. 2016), pp. 9596–9610 (cit. on p. 45).

[11] D. Gruyter. *Paper Products Physics and Technology*. Ek, Monica; Gellerstedt, Göran; Henriksson, Gunnar: Pulp and Paper Chemistry and Technology. De Gruyter, 2009. ISBN: 9783110213461. URL: https://books.google.at/books?id=oDde90yqkFkC (cit. on p. 1).

[12] Michael Hammer. *SOOFEAM software*. http://www.soofea.org/ (cit. on p. 70).

[13] Greg Haugstad. *Atomic Force Microscopy: Understanding Basic Modes and Advanced Applications*. John Wiley & Sons, Inc., 2012. ISBN: 9781118360668. URL: http://dx.doi.org/10.1002/9781118360668.fmatter (cit. on p. 57).

[14] Anton Hofer. *Regelungstechnik I*. Ed. by -. TU Graz, Institut fuer Regelungstechnik und Automatisierungstechnik, 2014 (cit. on p. 61).

[15] G.A. Holzapfel. *Nonlinear Solid Mechanics*. John Wiley & Sons Inc., 2006 (cit. on pp. 7, 16, 31, 32, 35, 82).

[16] G.A. Holzapfel, T.C. Gasser, and M. Stadler. "A structural model for the viscoelastic behavior of arterial walls: Continuum formulation and finite element analysis". In: *European Journal of Mechanics - A/Solids* 21.3 (2002), pp. 441–463. ISSN: 0997-7538. DOI: http://dx.doi.org/10.1016/S0997-7538(01)01206-2. URL: http://www.sciencedirect.com/science/article/pii/S0997753801012062 (cit. on pp. 47, 60, 65).

[17] Gerhard A. Holzapfel, Thomas C. Gasser, and Ray W. Ogden. "A New Constitutive Framework for Arterial Wall Mechanics and a Comparative Study of Material Models". In: *Journal of elasticity and the physical science of solids* 61.1 (July 2000), pp. 1–48. ISSN: 1573-2681. DOI: 10.1023/A:1010835316564. URL: https://doi.org/10.1023/A:1010835316564 (cit. on p. 23).

[18] M. Horn and N. Dourdoumas. *Regelungstechnik: Rechnerunterstuetzter Entwurf zeitkontinuierlicher und zeitdiskreter Regelkreise*. Elektrotechnik : Regelungstechnik. Pearson Studium, 2004. ISBN: 9783827370594. URL: https://books.google.at/books?id=qvFSDQEACAAJ (cit. on p. 61).

[19] K. L. Johnson. *Contact Mechanics*. Cambridge University Press, 1985. DOI: 10.1017/CBO9781139171731 (cit. on pp. 58, 59, 64, 69).

[20] H. Kuhn, Dana Medlin, and ASM International. Handbook Committee. *Mechanical Testing and Evaluation*. ASM Handbook: Mechanical Testing and Evaluation. ASM International, 2000. ISBN: 9780871703897 (cit. on p. 53).

[21] Dirk Liefeith. "Material Model for Anisotropic Rubber Viscoelasticity at Finite Deformations". MA thesis. Universitaet Stuttgart, 2007 (cit. on pp. 2, 17, 41).

[22] K. Madsen, H. B. Nielsen, and O. Tingleff. *Methods for Non-Linear Least Squares Problems (2nd ed.)* Richard Petersens Plads, Building 321, DK-2800 Kgs. Lyngby: Informatics and Mathematical Modelling, Technical University of Denmark, DTU, 2004, p. 60 (cit. on pp. 53, 54).

[23] J.E. Marsden and T.J.R. Hughes. *Mathematical Foundations of Elasticity*. Dover Civil and Mechanical Engineering. Dover Publications, 2012. ISBN: 9780486142272. URL: https://books.google.at/books?id=-STEAgAAQBAJ (cit. on p. 3).

[24] David Mercier, czambaldi, RaulSanchezMartin, Claudio, and techfips. *stabix: STABiX v1.6.3*. Feb. 2015. DOI: 10.5281/zenodo.14854. URL: https://doi.org/10.5281/zenodo.14854 (cit. on p. 74).

[25] C. Miehe. *Aspects of the Formulation and Finite Element Implementation of Large Strain Isotropic Elasticity*. Vol. 37. 1981-2004. International Journal for Numerical Methods in Engineering, 1994 (cit. on p. 22).

[26] J. Nocedal and S. Wright. *Numerical Optimization*. Springer Series in Operations Research and Financial Engineering. Springer New York, 2006. ISBN: 9780387303031. URL: https://books.google.at/books?id=eNlPAAAAMAAJ (cit. on p. 53).

[27] Roger Rowell. *Handbook Of Wood Chemistry And Wood Composites*. Feb. 2005. ISBN: 9780849315886 (cit. on p. 1).

[28] Hartmann S. and Neff P. *Polyconvexity of generalized polynomial-type hyperelastic strain energy functions for near-incompressibility*. Vol. 40. 2767-2791. International Journal of Solids and Structures, 2003 (cit. on pp. 22, 26, 34).

[29] Neff P. Schroeder J. *Invariant formulation of Hyperelastic Transverse Isoropy Based on Polyconvex Free Energy Functions*. Vol. 40. 401-445. International Journal of Solids and Structures, 2002 (cit. on pp. 17, 26, 82).

[30] J. C. SIMO. *On a Fully Three-dimensional Finite-strain Viscoelastic Damage Model: Formulation and Computational Aspects*. Vol. 60. 153-173. Computer Methods in Applied Mechanics and Engineering, 1987 (cit. on pp. 17, 82).

[31] A. J. M. Spencer. *Theory of Invariants*. Vol. 1. Eringen: Academic Press, New York, 1971 (cit. on p. 20).

[32] L. R. G. Treloar. *Stress-Strain Data for Vulcanised Rubber Under Various Types of Deformation*. Vol. 40: 59-70. Transactions of the Faraday Society, 1944 (cit. on p. 25).

[33] O. H. Yeoh. *Characterization of Elastic Properties of Carbon-black-filled Rubber Vulcanizates*. Vol. 63. 792-805. Rubber Chemistry and Technology, 1990 (cit. on pp. 17, 25, 82).

Appendix

1. Tensor Derivations

A. Derivation of $\frac{\partial J}{\partial \boldsymbol{F}}$

$$J = det(F) = \lambda_1 \lambda_2 \lambda_3 \tag{A.1}$$

$$\boldsymbol{F} = \sum_{\alpha=1}^{3} \lambda_\alpha \, \boldsymbol{n}_\alpha \otimes \boldsymbol{N}_\alpha \tag{A.2}$$

$$\boldsymbol{F}^{-1} = \sum_{\alpha=1}^{3} \frac{1}{\lambda_\alpha} \, \boldsymbol{N}_\alpha \otimes \boldsymbol{n}_\alpha \tag{A.3}$$

$$\frac{\partial J}{\partial \boldsymbol{F}} = \frac{\partial \lambda_1 \lambda_2 \lambda_3}{\partial \sum\limits_{\alpha=1}^{3} \lambda_\alpha \, \boldsymbol{n}_\alpha \otimes \boldsymbol{N}_\alpha} = \sum_{\alpha=1}^{3} \frac{\partial \lambda_1 \lambda_2 \lambda_3}{\partial \lambda_\alpha} \boldsymbol{n}_\alpha \otimes \boldsymbol{N}_\alpha \tag{A.4}$$

$$= \lambda_2 \lambda_3 \, \boldsymbol{n}_1 \otimes \boldsymbol{N}_1 + \lambda_1 \lambda_3 \boldsymbol{n}_2 \otimes \boldsymbol{N}_2 + \lambda_1 \lambda_2 \boldsymbol{n}_3 \otimes \boldsymbol{N}_3 \tag{A.5}$$

$$= \frac{\lambda_1 \lambda_2 \lambda_3}{\lambda_1} \, \boldsymbol{n}_1 \otimes \boldsymbol{N}_1 + \frac{\lambda_1 \lambda_2 \lambda_3}{\lambda_2} \, \boldsymbol{n}_2 \otimes \boldsymbol{N}_2 + \frac{\lambda_1 \lambda_2 \lambda_3}{\lambda_3} \, \boldsymbol{n}_3 \otimes \boldsymbol{N}_3 \tag{A.6}$$

$$= J \boldsymbol{F}^{-T} \tag{A.7}$$

B. Derivation of $\frac{\partial J}{\partial \boldsymbol{C}}$

Note: $J^2 = III_{\boldsymbol{C}}$

$$\boldsymbol{C} = \sum_{\alpha=1}^{3} \lambda_\alpha^2 \, \boldsymbol{N}_\alpha \otimes \boldsymbol{N}_\alpha \tag{A.8}$$

$$\frac{\partial J}{\partial \boldsymbol{C}} = \frac{\partial \lambda_1 \lambda_2 \lambda_3}{\partial \sum\limits_{\alpha=1}^{3} \lambda_\alpha^2 \, \boldsymbol{N}_\alpha \otimes \boldsymbol{N}_\alpha} = \sum_{\alpha=1}^{3} \frac{\partial \lambda_1 \lambda_2 \lambda_3}{\partial \lambda_\alpha^2} \, \boldsymbol{N}_\alpha \otimes \boldsymbol{N}_\alpha \tag{A.9}$$

$$\lambda_\alpha^2 = \bar{\lambda}_\alpha \tag{A.10}$$

$$\frac{\partial J}{\partial \boldsymbol{C}} = \sum_{\alpha=1}^{3} \frac{\partial (\bar{\lambda}_1^{\frac{1}{2}} \bar{\lambda}_2^{\frac{1}{2}} \bar{\lambda}_3^{\frac{1}{2}})}{\partial \lambda_\alpha^2} \, \boldsymbol{N}_\alpha \otimes \boldsymbol{N}_\alpha \tag{A.11}$$

$$= \frac{1}{2} \left[\frac{\bar{\lambda}_1 \bar{\lambda}_2 \bar{\lambda}_3}{\bar{\lambda}_1} \right]^{\frac{1}{2}} \boldsymbol{N}_1 \otimes \boldsymbol{N}_1 + \frac{1}{2} \left[\frac{\bar{\lambda}_1 \bar{\lambda}_2 \bar{\lambda}_3}{\bar{\lambda}_2} \right]^{\frac{1}{2}} \boldsymbol{N}_2 \otimes \boldsymbol{N}_2 + \frac{1}{2} \left[\frac{\bar{\lambda}_1 \bar{\lambda}_2 \bar{\lambda}_3}{\bar{\lambda}_3} \right]^{\frac{1}{2}} \boldsymbol{N}_3 \otimes \boldsymbol{N}_3 \tag{A.12}$$

$$= \frac{1}{2} \left[\frac{\lambda_1 \lambda_2 \lambda_3}{\lambda_1} \right] \boldsymbol{N}_1 \otimes \boldsymbol{N}_1 + \frac{1}{2} \left[\frac{\lambda_1 \lambda_2 \lambda_3}{\lambda_2} \right] \boldsymbol{N}_2 \otimes \boldsymbol{N}_2 + \frac{1}{2} \left[\frac{\lambda_1 \lambda_2 \lambda_3}{\lambda_3} \right] \boldsymbol{N}_3 \otimes \boldsymbol{N}_3 \tag{A.13}$$

$$= \frac{1}{2} \left[J \boldsymbol{C}^{-1} \right] \tag{A.14}$$

C. Derivation of $\frac{\partial III_{\boldsymbol{C}}}{\partial \boldsymbol{C}}$

$$\frac{\partial III_{\boldsymbol{C}}}{\partial \boldsymbol{C}} = \frac{\partial J^2}{\partial \boldsymbol{C}} \tag{A.15}$$

$$\text{with eq. A.14} \tag{A.16}$$

$$= 2J\frac{\partial J}{\partial \boldsymbol{C}} = J^2\boldsymbol{C}^{-1} \tag{A.17}$$

D. Derivation of $\frac{\partial I_{\boldsymbol{C}}}{\partial \boldsymbol{C}}$

$$\frac{\partial I_{\boldsymbol{C}}}{\partial \boldsymbol{C}} = \frac{\partial \boldsymbol{C} : \mathbf{1}}{\partial \boldsymbol{C}} \tag{A.18}$$

$$= \underbrace{\frac{\partial \boldsymbol{C}}{\partial \boldsymbol{C}}}_{=\mathbb{I}_{\boldsymbol{C}}} : \mathbf{1} + \boldsymbol{C} : \underbrace{\frac{\partial \mathbf{1}}{\partial \boldsymbol{C}}}_{=0} \tag{A.19}$$

$$= \mathbf{1} \tag{A.20}$$

E. Derivation of $\frac{\partial II_{\boldsymbol{C}}}{\partial \boldsymbol{C}}$

Note: $II := tr(\boldsymbol{C}\boldsymbol{C})$

$$\frac{\partial II_{\boldsymbol{C}}}{\partial \boldsymbol{C}} = \frac{\partial tr(\boldsymbol{C}\boldsymbol{C})}{\partial \boldsymbol{C}} = \frac{\partial \boldsymbol{C} : \boldsymbol{C}}{\partial \boldsymbol{C}} = \frac{\partial C_{MN}C_{MN}}{\partial C_{IJ}} \tag{A.21}$$

$$= \frac{\partial C_{MN}}{\partial C_{IJ}}C_{MN} + C_{NM}\frac{\partial C_{NM}}{\partial C_{IJ}} \tag{A.22}$$

$$\text{with eq. A.36} \tag{A.23}$$

$$= \delta_{MI}\delta_{NJ}C_{MN} + \delta_{NI}\delta_{MJ}C_{NM} \tag{A.24}$$

$$= 2C_{IJ} = 2\boldsymbol{C} \tag{A.25}$$

F. Derivation of $\frac{\partial \boldsymbol{C}^{-1}}{\partial \boldsymbol{C}}$

$$\frac{\partial \boldsymbol{I}}{\partial \boldsymbol{C}} = \boldsymbol{0} \tag{A.26}$$

$$\frac{\partial \boldsymbol{C}^{-1}\boldsymbol{C}}{\partial \boldsymbol{C}} = \boldsymbol{0} \tag{A.27}$$

$$\frac{\partial \left[(C^{-1})_{IM}(C^{-1})_{MJ}\right]}{\partial C_{KL}} = \underbrace{\frac{\partial (C^{-1})_{IM}}{\partial C_{KL}}}_{wanted} C_{MJ} + (C^{-1})_{IM}\frac{\partial C_{MJ}}{\partial C_{KL}} = \boldsymbol{0} \tag{A.28}$$

$$\frac{\partial C_{MJ}}{\partial C_{KL}} = \frac{1}{2}\left(\delta_{MK}\delta_{JL} + \delta_{JK}\delta_{ML}\right) \tag{A.29}$$

$$\frac{\partial (C^{-1})_{IM}}{\partial C_{KL}} C_{MJ} = -(C^{-1})_{IM}\frac{\partial C_{MJ}}{\partial C_{KL}} \quad \Big| \cdot (C^{-1})_{JN} \tag{A.30}$$

$$\frac{\partial (C^{-1})_{IM}}{\partial C_{KL}} \delta_{MN} = -\frac{1}{2}\left((C^{-1})_{IK}(C^{-1})_{NL} + (C^{-1})_{IL}(C^{-1})_{NK}\right) \tag{A.31}$$

$$\frac{\partial (C^{-1})_{IN}}{\partial C_{KL}} = -\frac{1}{2}\left((C^{-1})_{IK}(C^{-1})_{NL} + (C^{-1})_{IL}(C^{-1})_{NK}\right) \tag{A.32}$$

$$\text{substitute N} \rightarrow \text{J} \tag{A.33}$$

$$\frac{\partial (C^{-1})_{IJ}}{\partial C_{KL}} = -\frac{1}{2}\left((C^{-1})_{IK}(C^{-1})_{JL} + (C^{-1})_{IL}(C^{-1})_{JK}\right) = -\boldsymbol{C}^{-1} \odot \boldsymbol{C}^{-1} = \mathbb{I}_{\boldsymbol{C}^{-1}} \tag{A.34}$$

Note: $(C^{-1})_{JL}(C^{-1})_{IK} = (C^{-1})_{IK}(C^{-1})_{JL}$

G. Derivation of $\frac{\partial \boldsymbol{C}}{\partial \boldsymbol{C}}$

$$\frac{\partial \boldsymbol{C}}{\partial \boldsymbol{C}} = \frac{\partial \frac{1}{2}\left[C_{KL} + C_{LK}\right]}{\partial C_{IJ}} \tag{A.35}$$

$$= \frac{1}{2}\left[\delta_{IK}\delta_{JL} + \delta_{IL}\delta_{JK}\right] = \mathbb{I}_{IJKL} = \mathbb{I} \tag{A.36}$$

$$\tag{A.37}$$

H. Derivation of $\frac{\partial II_{\boldsymbol{C}}}{\partial \boldsymbol{C}}$

Note: $II_{\boldsymbol{C}} := \frac{1}{2}\left(tr[\boldsymbol{C}]^2 - tr[\boldsymbol{C}^2]\right)$

$$\frac{\partial II_{\boldsymbol{C}}}{\partial \boldsymbol{C}} = \frac{\partial \frac{1}{2}\left(tr[\boldsymbol{C}]^2 - tr[\boldsymbol{C}^2]\right)}{\partial \boldsymbol{C}} \tag{A.38}$$

$$= tr[\boldsymbol{C}]\frac{\partial tr[\boldsymbol{C}]}{\partial \boldsymbol{C}} - \frac{1}{2}\frac{\partial tr[\boldsymbol{C}^2]}{\partial \boldsymbol{C}} \tag{A.39}$$

$$\text{with eq. A.20 and eq. A.25} \tag{A.40}$$

$$= tr[\boldsymbol{C}]\boldsymbol{I} - \boldsymbol{C} = I_{\boldsymbol{C}}\boldsymbol{I} - \boldsymbol{C} \tag{A.41}$$

I. Derivation of $\frac{\partial \bar{\boldsymbol{C}}}{\partial \boldsymbol{C}}$

$$\frac{\partial \bar{\boldsymbol{C}}}{\partial \boldsymbol{C}} = \frac{\partial J^{-2/3}\boldsymbol{C}}{\partial \boldsymbol{C}} = J^{-2/3}\frac{\partial \boldsymbol{C}}{\partial \boldsymbol{C}} + \boldsymbol{C} \otimes \frac{\partial J^{-2/3}}{\partial \boldsymbol{C}} \tag{A.42}$$

$$= J^{-2/3}\frac{\partial \boldsymbol{C}}{\partial \boldsymbol{C}} + \frac{-2}{3}J^{-5/3}\boldsymbol{C} \otimes \frac{\partial J}{\partial \boldsymbol{C}} \tag{A.43}$$

$$\text{with eq. A.14 and A.36} \tag{A.44}$$

$$= J^{-2/3}\mathbb{I} - \frac{2}{3}J^{-5/3}\frac{1}{2}J\boldsymbol{C} \otimes \boldsymbol{C}^{-1} \tag{A.45}$$

$$= J^{-\frac{2}{3}}\left[\mathbb{I} - \frac{1}{3}\boldsymbol{C} \otimes \boldsymbol{C}^{-1}\right] = \mathbb{Q} \tag{A.46}$$

J. Derivation of $2\frac{\partial \bar{\boldsymbol{C}}}{\partial \boldsymbol{C}\partial \boldsymbol{C}}$

$$2\partial_{C_{ij}C_{kl}}\bar{C}_{mn} = 2\frac{\partial}{\partial C_{kl}}\left(J^{-\frac{2}{3}}\left[\mathbb{I}_{mnij} - \frac{1}{3}C_{mn}C^{-1}_{ij}\right]\right) \tag{A.47}$$

$$= 2\left\{-\frac{2}{3}J^{-\frac{2}{3}-1}\frac{\partial J}{\partial C_{kl}}\left[\mathbb{I}_{mnij} - \frac{1}{3}C_{mn}C^{-1}_{ij}\right] - \frac{J^{-\frac{2}{3}}}{3}\left[\frac{\partial C_{mn}}{\partial C_{kl}}C^{-1}_{ij} + C_{mn}\frac{\partial C^{-1}_{ij}}{\partial C_{kl}}\right]\right\} \tag{A.48}$$

$$= 2\left\{-\frac{2}{3}J^{-\frac{2}{3}-1}\frac{1}{2}JC^{-1}_{kl}\left[\mathbb{I}_{mnij} - \frac{1}{3}C_{mn}C^{-1}_{ij}\right] - \frac{J^{-\frac{2}{3}}}{3}\left[\mathbb{I}_{mnkl}C^{-1}_{ij} - C_{mn}\{\mathbb{I}_{\boldsymbol{C}^{-1}}\}_{ijkl}\right]\right\} \tag{A.49}$$

$$= \frac{2}{3}J^{-\frac{2}{3}}\left\{C^{-1}_{kl}\left(\frac{1}{3}C_{mn}C^{-1}_{ij} - \mathbb{I}_{mnij}\right) + \left(C_{mn}\{\mathbb{I}_{\boldsymbol{C}^{-1}}\}_{ijkl} - \mathbb{I}_{mnkl}C^{-1}_{ij}\right)\right\} = \mathbb{M} \tag{A.50}$$

K. Derivation of $\frac{\partial(\boldsymbol{C}:\boldsymbol{M})}{\partial \boldsymbol{C}}$

Note: Where $\boldsymbol{M}$ is a symmetric structural tensor and therefore independent of $\boldsymbol{C}$

$$\frac{\partial tr(\boldsymbol{C}\boldsymbol{M})}{\partial \boldsymbol{C}} = \frac{\partial(\boldsymbol{C}:\boldsymbol{M})}{\partial \boldsymbol{C}} \tag{A.51}$$

$$= \frac{\partial \boldsymbol{C}}{\partial \boldsymbol{C}} : \boldsymbol{M} \tag{A.52}$$

$$\text{with eq. A.36} \tag{A.53}$$

$$= \mathbb{I} : \boldsymbol{M} = \boldsymbol{M} \tag{A.54}$$

L. Derivation of $\frac{\partial(\boldsymbol{C}^2:\boldsymbol{M})}{\partial \boldsymbol{C}}$

Note: Where $\boldsymbol{M}$ is a symmetric structural tensor and therefore independent of $\boldsymbol{C}$

$$\frac{\partial tr(\boldsymbol{C}^2\boldsymbol{M})}{\partial \boldsymbol{C}} = \frac{\partial M_{ik}C_{kl}C_{lm}\delta_{im}}{\partial C_{rs}} \tag{A.55}$$

With eq. A.36 (A.56)

$$= \frac{1}{2}M_{ik}\left[\delta_{rk}\delta_{sl} + \delta_{rl}\delta_{sk}\right]C_{lm}\delta_{im} + \frac{1}{2}M_{ik}C_{kl}\left[\delta_{rl}\delta_{sm} + \delta_{rm}\delta_{sl}\right]\delta_{im} \tag{A.57}$$

$$= \frac{1}{2}\left[C_{sm}M_{mr} + C_{rm}M_{ms}\right] + \frac{1}{2}\left[M_{sk}C_{kr} + M_{rk}C_{ks}\right] \tag{A.58}$$

Using the symmetry to establish a closed form (A.59)

$$= C_{sm}M_{mr} + M_{sm}C_{mr} = \boldsymbol{C}\boldsymbol{M} + \boldsymbol{M}\boldsymbol{C} \tag{A.60}$$

M. Derivation of $\frac{\partial^2 I\!I_{\boldsymbol{C}}}{\partial \boldsymbol{C}\partial \boldsymbol{C}}$

Note: $I\!I_{\boldsymbol{C}} := \frac{1}{2}\left(tr[\boldsymbol{C}]^2 - tr[\boldsymbol{C}^2]\right)$
With given first derivation of the second invariant A.41:

$$\frac{\partial(I_{\boldsymbol{C}}\boldsymbol{1} - \boldsymbol{C})}{\partial \boldsymbol{C}} = \frac{\partial I_{\boldsymbol{C}}}{\partial \boldsymbol{C}} \otimes \boldsymbol{1} - \frac{\partial \boldsymbol{C}}{\partial \boldsymbol{C}} \tag{A.61}$$

With the eq. A.36 and A.20 at hand, it follows: (A.62)

$$= \boldsymbol{1} \otimes \boldsymbol{1} - \mathbb{I} \tag{A.63}$$

N. Derivation of $\frac{\partial^2 tr(\boldsymbol{C}^2\boldsymbol{M})}{\partial \boldsymbol{C}\partial \boldsymbol{C}}$

Note: Where $\boldsymbol{M}$ is a symmetric structural tensor and therefore independent of $\boldsymbol{C}$
Using the already known first derivation A.60:

$$\frac{\partial(M_{kn}C_{nl} + C_{kn}M_{nl})}{\partial C_{ij}} = M_{kn}\frac{\partial C_{nl}}{\partial C_{ij}} + \frac{\partial C_{kn}}{\partial C_{ij}}M_{nl} \tag{A.64}$$

With eq. A.36 (A.65)

$$M_{kn}\frac{1}{2}(\delta_{in}\delta_{jl} + \delta_{il}\delta_{jn}) + \frac{1}{2}(\delta_{ik}\delta_{jn} + \delta_{in}\delta_{jk})M_{nl} \tag{A.66}$$

$$\frac{1}{2}(M_{ki}\delta_{jl} + \delta_{il}M_{kj}) + \frac{1}{2}(\delta_{ik}M_{jl} + M_{il}\delta_{jk}) \tag{A.67}$$

$$\frac{1}{2}(M_{ik}\delta_{jl} + \delta_{jk}M_{il}) + \frac{1}{2}(\delta_{ik}M_{jl} + M_{jk}\delta_{il}) = \boldsymbol{M}\tilde{\otimes}\boldsymbol{1} + \boldsymbol{1}\tilde{\otimes}\boldsymbol{M} \tag{A.68}$$

$$(\boldsymbol{A}\tilde{\otimes}\boldsymbol{B})_{ijkl} = \frac{1}{2}(A_{ik}B_{jl} + B_{jk}A_{il}) \tag{A.69}$$

2. Implementation of Hybrid Formulation

With the keyword HYBRID FORMULATION it is possible to specify which multi-field variational principle is used in the UMAT in the ABAQUS environment. Out of the manual [1] it is recommended to use the HYBRID FORMULATION=TOTAL which is a version of a Hu-Washizu variational principle. For that it is necessary to calculate the extra derivatives of the volumetric strain energy potential.

$$\hat{p} = -\frac{\partial U(\hat{J})}{\partial J} \tag{A.70}$$

$$\hat{K} = J\frac{\partial^2 U(\hat{J})}{\hat{J}^2} \tag{A.71}$$

$$\frac{\partial^2 U(\hat{J})}{\partial \hat{J}^2} = J\frac{\partial^3 U(\hat{J})}{\partial \hat{J}^3} \tag{A.72}$$

To incorporate the hydrostatic pressure $\hat{p}$ the determinant J is replaced by $\hat{J}$ in the derivations of the elastic potentials ψ'_{vol} and ψ''_{vol}. The bulk modulus $\hat{K}$ and $\frac{\partial^2 U(\hat{J})}{\partial \hat{J}^2}$ are passed into the stress array by extending it by NTENS + 1 and NTENS + 2.

3. Corotated Frame

Due to the updated Lagrangian formulation and the usage of a corotated frame principle, Abaqus expects a Green-Nahgdi rate form of the tangent. The Green-Nahgdi rate $\boldsymbol{\sigma}^{\Delta}$ can be approximated with the Jaumann rate $\boldsymbol{\sigma}^{\nabla}$. For that reason the Euler tangent has to be modified to fulfil the requirement of UMAT output[1].

The variation in Abaqus is performed in terms of the Truesdell rate of the Kirchhoff stresses $\boldsymbol{\tau}^{\circ}$.

$$\boldsymbol{\tau}^{\circ} = J\boldsymbol{c} : \boldsymbol{d} \tag{A.73}$$

$$\pounds\boldsymbol{\tau} = \boldsymbol{\tau}^{\circ} = \dot{\boldsymbol{\tau}} - \boldsymbol{l}\boldsymbol{\tau} - \boldsymbol{\tau}\boldsymbol{l}^{T} \tag{A.74}$$

The Euler tangent $\boldsymbol{c}$ can be calculated by the push forward operation of the Lagrange tangent $\mathbb{C}$ in remark 10. With the split of the velocity gradient tensor $\boldsymbol{l} = \boldsymbol{d} + \boldsymbol{w}$ into its symmetric and antisymmetric part and the Cauchy stresses $\boldsymbol{\tau} = J\boldsymbol{\sigma}$ and $\dot{J} = J\,tr(\boldsymbol{d})$ equation A.74 can be rewritten.

$$\boldsymbol{\tau}^{\circ} = J\left[\dot{\boldsymbol{\sigma}} - (\boldsymbol{d}+\boldsymbol{w})\boldsymbol{\sigma} - \boldsymbol{\sigma}(\boldsymbol{d}+\boldsymbol{w})^{T} + tr(\boldsymbol{d})\boldsymbol{\sigma}\right] \tag{A.75}$$

By multiplying out and considering the identity of the antisymmetric spin tensor $\boldsymbol{w}^{T} = -\boldsymbol{w}$, the first three parts can be identified as the Jaumann rate.

$$\boldsymbol{\tau}^{\circ} = J\left[\underbrace{\dot{\boldsymbol{\sigma}} + \boldsymbol{\sigma}\boldsymbol{w} - \boldsymbol{w}\boldsymbol{\sigma}}_{\boldsymbol{\sigma}^{\nabla}} - \boldsymbol{d}\boldsymbol{\sigma} - \boldsymbol{\sigma}\boldsymbol{d} + (\boldsymbol{1} : \boldsymbol{d})\boldsymbol{\sigma}\right] \tag{A.76}$$

Introducing equation A.76 into equation A.73 and reordering gives:

$$\boldsymbol{\sigma}^{\nabla} = \boldsymbol{c} : \boldsymbol{d} + \boldsymbol{d}\boldsymbol{\sigma} + \boldsymbol{\sigma}\boldsymbol{d} - (\boldsymbol{1} : \boldsymbol{d})\boldsymbol{\sigma} \tag{A.77}$$

To get the Jaumann tangent $\boldsymbol{c}^{\nabla}$ as specified in equation A.78, the rate of deformation tensor $\boldsymbol{d}$ has to be appropriately rearranged in equation A.77.

$$\boldsymbol{\sigma}^{\nabla} = \boldsymbol{c}^{\nabla} : \boldsymbol{d} \tag{A.78}$$

This is in the following outlined in index notation. Where $\mathbb{I}_{ijkl}$ is the fourth order identity tensor.

$$\sigma_{ij}^{\nabla} = c_{ijkl}d_{kl} + d_{ik}\sigma_{kj} + \sigma_{ik}d_{kj} - \delta_{kl}d_{kl}\sigma_{ij} \tag{A.79}$$

$$= c_{ijkl}d_{kl} + \sigma_{kj}\mathbb{I}_{ikmn}d_{mn} + \sigma_{ik}\mathbb{I}_{kjmn}d_{mn} - \delta_{kl}\sigma_{ij}\mathbb{I}_{klmn}d_{mn} \tag{A.80}$$

$$= c_{ijkl}d_{kl} + \frac{1}{2}\left[\sigma_{kj}(\delta_{im}\delta_{kn} + \delta_{in}\delta_{km}) + \sigma_{ik}(\delta_{km}\delta_{jn} + \delta_{kn}\delta_{jm}) - \delta_{kl}(\delta_{km}\delta_{ln} + \delta_{kn}\delta_{lm})\sigma_{ij}\right]d_{mn} \tag{A.81}$$

$$= c_{ijkl}d_{kl} + \frac{1}{2}\left[\sigma_{nj}\delta_{im} + \sigma_{mj}\delta_{in} + \sigma_{im}\delta_{jn} + \sigma_{in}\delta_{jm} - \sigma_{ij}(\delta_{mn} + \delta_{mn})\right]d_{mn} \tag{A.82}$$

$$= c_{ijkl}d_{kl} + \frac{1}{2}\left[\sigma_{lj}\delta_{ik} + \sigma_{kj}\delta_{il} + \sigma_{ik}\delta_{jl} + \sigma_{il}\delta_{jk} - 2\sigma_{ij}\delta_{kl}\right]d_{kl} \tag{A.83}$$

$$= \underbrace{c_{ijkl}d_{kl} + \frac{1}{2}\left[\delta_{ik}\sigma_{jl} + \sigma_{ik}\delta_{jl} + \delta_{il}\sigma_{jk} + \sigma_{il}\delta_{jk} - 2\sigma_{ij}\delta_{kl}\right]d_{kl}}_{c_{ijkl}^{\nabla}} \tag{A.84}$$

So by adding these additional terms to the Euler tangent the Jaumann Euler tangent can be calculated.

[1] For futher information, see [1], [4], [2].

4. Mesh Dependence

The discontinuous peak in figure A.1 is representing the unaveraged values of four elements which are located in the middle. This peak is a result of an unwanted influence of the mesh discretisation on the contact algorithm. Yet, it has no influence on the indentation result. It was found out that the peak can be eliminated if the mesh parameter *c_divi* is chosen accordingly. Consequently, the peak was a result of big differences in element size of elements that are close to each other.

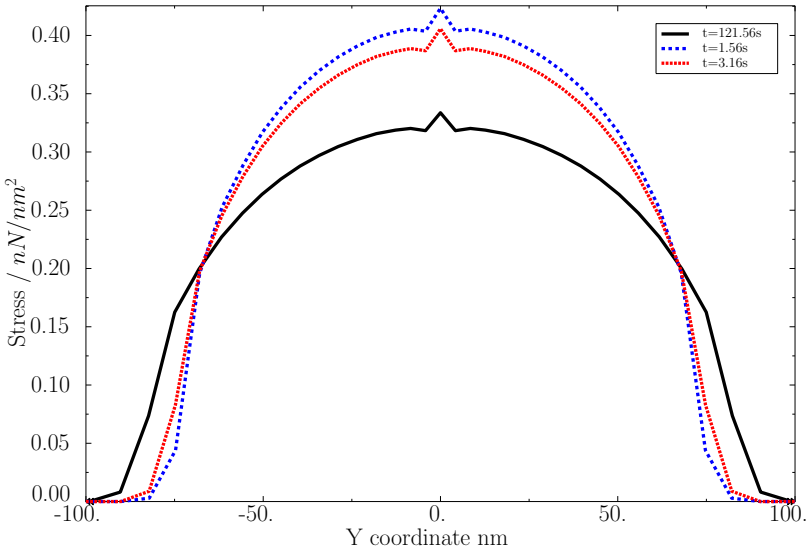

Figure A.1.: Contact pressure distribution along y-axis

5. Class Diagram of Soofeam Matlab Program